Monte Carlo Simulations of the High Energy X-ray Spectrometer (HEX) on Chandrayaan-I

by

Manju Sudhakar
ISRO Satellite Centre, Bangalore

A thesis submitted in partial fulfillment for the
degree of Doctor of Philosophy to the

Department of Physics
University of Calicut
Calicut, Kerala

March 2010

Certificate

This is to certify that the thesis titled "**Monte Carlo Simulations of the High Energy X-ray Spectrometer (HEX) on Chandrayaan-I**" is a bonafide record of the work done by Miss Manju Sudhakar under our joint supervision and that no part of it has been included any where previously for the award of any degree, either in this university or any other institution.

Dr. P. Sreekumar
Group Director, SAG
ISRO Satellite Centre
Bangalore

Dr. B.R.S Babu
Professor, Department of Physics
University of Calicut
Kerala

March 2010

Declaration of Authorship

I hereby declare that the thesis titled "**Monte Carlo Simulations of the High Energy X-ray Spectrometer (HEX) on Chandrayaan-I**" is an authentic record of the research work carried out by me under the supervision of Dr. P. Sreekumar, Group Director, Space Astronomy Group (SAG), ISRO Satellite Centre, Bangalore and Dr. B.R.S. Babu, Professor, Department of Physics, University of Calicut. No part of this work has formed the basis for award of any other degree or diploma in any university or institution.

Manju Sudhakar

March 2010

Your time is limited, so don't waste it living someone else's life. Don't be trapped by dogma - which is living with the results of other people's thinking. Don't let the noise of other people's opinion drown out your own inner voice. And most important, have the courage to follow your heart and intuition. They somehow already know what you truly want to become. Everything else is secondary.

Steve Jobs
American Entrepreneur, Apple Co-Founder

Abstract

HEX (High Energy X-ray Spectrometer) was one of the instruments on Chandrayaan-I, designed to detect and measure the intensity of high energy x-rays from 30 keV to 270 keV. The study of planetary radiation in this energy range is very challenging due to low signal strength and intense detector and planetary background emission. HEX consists of a CdZnTe compound semiconductor as the primary detector, and a CsI(Tl) scintillator as the secondary detector. The purpose of the secondary detector is to act as an anti-coincidence detector (ACD) to facilitate Compton suppression and background rejection in the primary detector. There were in total eleven experiments onboard the satellite, and the lifetime of the mission was planned to be two years; so there were constraints of size and weight of the various experimental payloads.

This thesis addresses design optimization of the ACD in terms of the number of detectors and shield thickness. It also includes estimation of the background that would be seen by the CdZnTe detector of HEX, and the Compton suppression and background rejection efficiency of the ACD. The predicted background includes contributions from high energy lunar albedo emission, and from the interaction of galactic cosmic rays with the payload and spacecraft. As a part of the ground work, the simulation codes and logic are validated against experimental and published results. The instrumental response of the CdZnTe and CsI(Tl) detectors are also simulated, using input from experimental data collected during calibration of the flight detectors. The Monte Carlo simulation toolkit, Geant4 is used extensively in this work. The methodology and results of the simulations, as well as experimental results and cross comparisons are presented in this work.

Contents

Abbreviations

HEX	**H**igh **E**nergy **X**-ray Spectrometer
ACD	**A**nti-**C**oincidence **D**etector
CZT	**C**admium-**Z**inc-**T**elluride
CsI	**C**esium **I**odide
GCR	**G**alactic **C**osmic **R**ay
SEP	**S**olar **E**nergetic **P**articles
LGRA	**L**unar **G**amma-**R**ay **A**lbedo
LNA	**L**unar **N**eutron **A**lbedo
SRF	**S**pectral **R**edistribution **F**unction
PMT	**P**hoto**M**ultiplier **T**ube
GSPM	**G**eneral **P**article **S**ource **M**odule
SNR	**S**ignal-to-**N**oise **R**atio
ESA	**E**uropean **S**pace **A**gency
CSPA	**C**harge **S**ensitive **P**re-**A**mplifier
SA	**S**haper-**A**mplifier
ADC	**A**nalog-to-**D**igitial **C**onverter
MCA	**M**ulti-**C**hannel **A**nalyzer
SC	**S**emi**c**onductor

List of Figures

List of Tables

To my Family . . .

Preface

Man cannot discover new oceans unless he has the courage to lose sight of the shore

Andre Gide

The ‘race to the Moon’ during the years 1959-1976 resulted in immense technological development, as well as getting to know our closest neighbor in space better. The 1990s saw a sudden spurt in missions to the Moon, started by the Japanese with Hiten in 1990 and then by the United States with Clementine (1994) and the Lunar Prospector (1998). Hiten was a flyby and orbiter, with experiments to test technology. Clementine had cameras with different filters to map the Moon in different wavelengths and a laser altimeter, which obtained the first global topographic map of the Moon. The Lunar Prospector (LP) was a 19 month, low polar orbit mission, with experiments to map the surface composition of the Moon, possible ice deposits, measurements of the magnetic fields, gravitational fields, and lunar out-gassing events.

Now, almost a decade later, ESA launched SMART-1 in 2003, while October 2007 saw the launch of the Japanese lunar mission Kaguya and the Chinese lunar spacecraft Chang’e. The Lunar Reconnaissance Orbiter (LRO) of the United States was launched in 2009. India has also entered the lunar exploration efforts with the launch of her first Moon mission, Chandrayaan-I (which means “journey to the Moon” in Sanskrit) on October 22, 2008.

The Chandrayaan-I mission

The aim of Chandrayaan-I [1] was to gain a better understanding of the origin and evolution of the Moon, through mineralogical and chemical mapping of the lunar surface, with high spatial and spectral resolution. Using instruments with spatial resolution of the order of 5 m in the visible and capabilities to measure altitudes on the lunar surface of the order of 10 m, Chandrayaan-I had the ability to generate a high resolution digital elevation map of the Moon. It also aimed to conduct a chemical and mineralogical study of the Moon's entire surface, with a 25 km (full width at half-maximum) spatial resolution on the surface for x-rays with energies less than 10 keV and 33 km for x-rays with energies less than 120 keV. The initial trajectory of the spacecraft around the Moon was a polar orbit (inclination of 90°), 100 km above the surface.

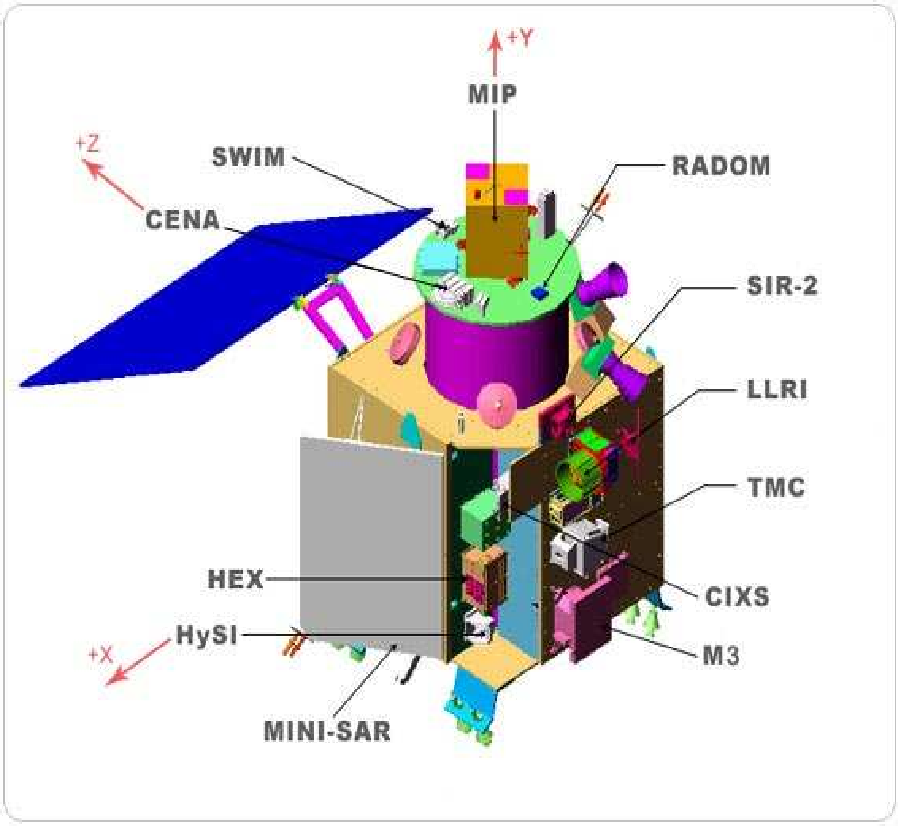

FIGURE 1: The Chandrayaan-I spacecraft

The Chandrayaan-I spacecraft was a cuboid of side 1.5 m, and weighed 1304 kg during launch. Once in orbit it weighed 590 kg. It carried eleven scientific experiments - five Indian, four International and two collaborative. A single solar panel was used for power generation. It was canted at 30° with respect to the pitch axis of the spacecraft to ensure adequate power generation for all possible spacecraft orientations with respect to the Sun during the full mission. When eclipsed by the Moon, the spacecraft was powered by a Li-ion battery. The fuel was a bi-propellant. There were three solid state recorders (SSRs) with total data storage capability of 40 GB. The Chandrayaan-I Ground Segment consists of three major elements - the Deep Space Network (DSN), Spacecraft Control Centre (SSC) and the Indian Space Science Data Centre (ISSDC). The Ground Segment is used to enable communication to and from the spacecraft, monitor spacecraft health data, carry out orbit and attitude maintenance, conduct payload operations, and makes available scientific data along with auxiliary data to the wider scientific community.

The range of experiments on Chandrayaan-I are briefly summarized below :

- **Terrain Mapping Camera** (TMC) - It aimed to map the topography in both the near and far side of Moon in the panchromatic spectral region of 0.5 to 0.85 μm with a spatial resolution of 5 m and a 20 km swath. It had three detectors for stereoscopic mapping, which used Active Pixel Sensor (APS) technology, and single refractive optics, which would cover the entire field-of-view of the three detectors.

- **Hyper Spectral Imager** (HySI) - It provided spectroscopic data for mineralogical mapping of the lunar surface to improve upon current information on mineral composition of the lunar surface. It had the capability to map the lunar surface in 64 bands in the Very Near Infra Red (VNIR) spectral range of 0.4-0.95 μm with a spectral resolution of better than 15 nm and spatial resolution of 80 m with swath coverage of 20 km. Refractive optics was used to focus on to an APS detector. Spectral separation was done using a wedge filter instead of prism or grating.

- **Lunar Laser Ranging Instrument** (LLRI) - It aimed to determine the global topographical field of the Moon in the vertical scale and to obtain an improved model for the lunar gravity field, supplementing the data from TMC and HySI payloads. Laser light at 1064 nm wavelength was transmitted to the lunar surface, where some fraction of it was scattered back in the direction of transmitter. Optical receivers collected it and focuses it onto a photo detector. The variation of the electrical signal could be translated into an altimetric map of the lunar surface.

- **High Energy X-ray Spectrometer** (HEX)[2] - It covered the hard X-ray region from 30 keV to 270 keV, with 33 km spatial resolution. The prime objective was to study excess ^{210}Pb in lunar poles and permanently shadowed craters. A measured excess would be a consequence of the transport of volatile ^{222}Rn to these cold traps and would provide support to the theory of transport of volatiles like water to the poles and permanently shadowed craters. It also aimed to identify regions of high U/Th concentrations via detection of emission of various decay products whose γ-rays lines fall within the HEX energy range.

- **Moon Impact Probe** (MIP) - It aimed to demonstrate technologies required for impacting a probe at a desired location on the Moon, and exploration of the Moon from close range. The impact probe was released at a predetermined time after the orbiter reached the final 100 km orbit to impact at a pre-selected location. The total flight time from release to impact on the Moon was close to twenty minutes. It consisted of a Video Imaging System for acquiring images of the surface of Moon from the descending probe and also a mass spectrometer to sample the tenuous lunar atmosphere during descent.

- **Chandrayaan 1 X-ray Spectrometer** (C1XS) - This experiment used x-ray fluorescence in the 1.0 keV to 10 keV energy region to measure elemental abundances of Mg, Al, Si, Ca, Fe, Ti distributed over the lunar surface. The x-ray sensor used was the Swept Charge Device (SCD). C1XS carried an X-ray Solar Monitor (XSM) to record the solar x-ray flux incident on the Moon. This was necessary to derive the absolute elemental abundances.

- **Near Infrared Spectrometer** (SIR-2) - This aimed to analyze the lunar surface in various geological/mineralogical and topographical units, to study the vertical distribution of crustal material, to study the formation process of lunar features, and to survey mineral lunar resources for future landing sites and exploration. Its optics collected reflected Moon light and fed it through an optical fiber to a grating. The dispersed light reached a row of photosensitive pixels. The wavelength range covered by the spectrometer was 0.93-2.4 μm with spectral resolution 6 nm.

- **Sub keV Atom Reflecting Analyzer** (SARA) - It aimed to image the lunar surface using low energy neutral atoms in the energy range 10 eV-2 keV, including permanently shadowed and volatile rich areas. SARA also aimed to image surface interaction of solar wind and lunar surface magnetic anomalies. SARA consisted of three parts - a neutral atom sensor, CENA (Chandrayaan-1 Energetic Neutrals Analyzer), a solar wind monitor, SWIM (Solar WInd Monitor), and a Digital Processing Unit, DPU.

- **Radiation Dose Monitor** (RADOM) - It qualitatively and quantitatively characterized the radiation environment in near Moon space. RADOM was a miniature spectrometer-dosimeter for measuring the spectrum of the deposited energy from primary and secondary particles in 256 channels.

- **Miniature Aperture Radar** (MiniSAR) - It aimed to detect water ice in the permanently shadowed regions on the lunar poles up to a depth of a few meters. The system would transmit Right Circular Polarization (RCP) and receive both Left Circular Polarization (LCP) and RCP. The radar system worked at a frequency 2.38 GHz with a resolution of 75m per pixel.

- **Moon Mineralogy Mapper** (M3) - It aimed to characterize and map the lunar surface mineralogy to help study more about lunar geological evolution. Lunar mineral resources would be mapped at high spatial resolution which would help facilitate planning target sites for future missions. The instrument was an imaging spectrometer operating in 0.7 to 3.0 μm range. It had a spatial resolution of 70 m per pixel and a 40 km field-of-view. It was recently credited with the discovery of water on the Moon.

The launch vehicle used for this mission was PSLV-C11 (Polar Satellite Launch Vehicle).

The work presented in this thesis discusses design optimization, test and characterization of the x-ray detectors on the High Energy X-ray Spectrometer (HEX) carried out by the author. The spectral parameters derived from the experimental data are used to model the response of the HEX detectors, which is then used to estimate the HEX detector background in lunar orbit.

Bibliography

[1] Goswami, J.L and Annadurai, M *Chandrayaan-1: India's first planetary science mission to the Moon*, Current Science, Volume 96, Number 4, pp 486-491, 2009

[2] Sreekumar, P et al., *High Energy X-ray Spectrometer on Chandrayaan-1*, Current Science, Volume 96, Number 4, pp 520-525, 2009

Chapter 1

Introduction

1.1 The High Energy X-ray Spectrometer (HEX) on Chandrayaan-I

1.1.1 Science Goals

There was a period in the early history of the solar system between 4 and 3.8 billion years ago when the planetoids in the inner solar system were intensively bombarded by comets and asteroids. Geologists and astronomers theorize that the Earth's water was probably delivered by these celestial objects through bombardment. The following question was asked then - since the Moon orbits the Earth at a distance of $\sim$400,000 km, why could not water be present on the moon due to deposition by similar asteroid and cometary bombardment.

The Apollo missions confirmed the fact that the dominant forces that were at work to shape the lunar surface were impact related. All these facts pointed out that water should be present on the Moon, but since the Moon's gravity is only 1/6 that of the Earth, most of the water would have sublimed and escaped from the Moon.

NASA's 1994 lunar mission Clementine, orbited the Moon from pole to pole and one of the experiments onboard beamed radio signals into shadowed craters near the Moon's south pole. The reflected signal was detected by Earth based telescopes and these signals indicated the presence of water ice. The data and its implications were not conclusive as the Arecibo telescope which was used for cross verification purposes, was not able to detect such signals from the same crater.

The Lunar Prospector (LP) launched by NASA in 1998, also studied the Moon from a polar orbit. One of the experiments onboard was the neutron spectrometer, which detected the flux of neutrons (thermal, epithermal and fast) from the Moon's surface. The presence of hydrogen compounds cause epithermal neutrons to lose energy via scattering and hence cause them to thermalize. When the flux of these neutrons decreases over a region, it could indicate the presence of hydrogen-based compounds there. Scans conducted by LP over lunar craters at the poles yielded depleted epithermal neutron flux, suggesting the presence the hydrogen, probably trapped in water ice. At the end of its mission, LP was made to crash near the south lunar pole, hoping to release some of the water for detection by Earth-based telescopes. However, there was no conclusive evidence.

The information that could be gathered from these experiments is that there **could be water trapped in permanently shadowed regions** on the Moon over billions of years. The Moon has no atmosphere and any volatile substance, like water, will rapidly sublime and escape into space. During one lunar day (equivalent to 29 Earth days), all regions of the Moon experiencing day time are exposed to sunlight with the temperature reaching $\sim$140°C. This is capable of subliming all exposed volatiles.

Water ice delivered to the Moon by bombardment would be scattered on the surface, most of which is quickly lost by sublimation. Since the moon is tilted by $\sim 1.5^\circ$ with respect to the ecliptic, there are some regions at both the polar regions which do not get sunlight. Craters present in these regions are therefore permanently shadowed. Some of the water ice could end up in these "cold traps" either by directly entering the crater or through random migration over the surface as molecules, subsequently becoming preserved there in frozen form, building up reservoirs over billions of years. Clementine data showed that 6000-15,000 km^2 of the lunar south pole is permanently shadowed.

Water ice is an extremely important lunar resource from the point of view of the following

- Future lunar colonies would be benefited if reservoirs of water ice are found on the Moon. Shipping water from the Earth to the Moon is extremely expensive, with estimates running into thousands of dollars per kilogram.
- Water ice could also be broken down into its constituents of Oxygen and Hydrogen; Oxygen to be used for life support systems and Hydrogen to be used for rocket fuel.
- Water ice would represent pristine material probably billions of years old and would help scientists to constrain possible lunar impact models, extraterrestrial origin of life, and the effects of photo-dissociation and solar wind sputtering.

In addition to water, there are other volatile substances like Hydrogen, Helium, Argon (decay product of radioactive Potassium and/or Krypton), Nitrogen, Neon, Radon (decay product of the U-Th series), Carbon monoxide, Carbon dioxide, Methane, and Oxygen. Some of these have been deposited in the lunar soil (regolith) over millions of years by the solar wind interactions, while others are products of natural radioactivity that occur deep within the lunar mantle or core, which seeps to the surface during low intensity tectonic or volcanic activity on the Moon. Radon (^{222}Rn) and Polonium (^{210}Po) are part of the U-Th decay chain, and they decay via the emission of alpha particles of specific energies. The alpha particle spectrometer aboard LP detected these alpha particles at the Aristarchus crater [1a], [2a], which is known to be an active out-gassing site. Once ^{222}Rn is released from vents and cracks in the surface it spreads out, the spatial distribution of which can be considered to follow a random walk process. The gas can spread up to 100 km before it decays to solid ^{210}Po in 3.8 days, emitting 5.5 MeV alpha particles. This radioactive product decays by emission of 5.3 MeV alpha particles in 138 days to produce ^{210}Pb. ^{210}Pb has a half life of 22 years, decaying to ^{210}Bi with the emission of the 46.5 keV γ-ray line. Mapping the intensity of this decay line over the lunar surface with hard x-ray/soft γ-ray detectors can help in tracing the location of ^{222}Rn out-gassing sites.

Just as it was speculated that water ice could end up in cold traps (permanently shadowed craters at the poles) over billions of years, it has been hypothesized that the above mentioned volatiles could also end up in these regions, accumulating and solidifying over time, preserved from sublimation and eventual loss from the lunar surface.

If a hard x-ray detector scans the lunar surface from a polar orbit, and if enhanced signals of the 46.5 keV line are detected in cold traps, the theory that volatile substances solidify and accumulate in these regions gains more confidence. **^{222}Rn decay to ^{210}Pb and its subsequent detection via the 46.5 keV line will act as a tracer to locate regions of possible volatile enrichment on the moon**. Future robotic landers and colonizers can mine these areas and treat the regolith so that the volatiles that have been implanted into the regolith can be extracted.

The High Energy X-ray Spectrometer on Chandrayaan-I was developed essentially to

- map the intensity of the 46.5 keV γ-ray line over the lunar surface which acts a tracer for volatile transport over the lunar surface.

HEX was designed to operate in the range **30 keV to 270 keV**. In addition to detection of the 46.5 keV line, HEX also aimed to detect

- radioactive decay lines from Uranium and Thorium that fall within this energy range (63.3 keV and 92.4 keV of ^{234}Th, 186.2 keV of ^{226}Ra, 185.7 keV of ^{235}U, 209.2 keV of ^{228}Ac, 238.6 keV of ^{212}Pb, and 241.9 keV of ^{214}Pb) and determine the abundances of these elements on the lunar surface.

1.1.2 Choice of Detectors for HEX

The γ-ray detectors used on Apollo 15-16 mission were scintillator detectors, NaI(Tl) with plastic anti-coincidence while on LP, the detector used was Bismuth-Germanate (BGO) with a plastic anti-coincidence detector. These detectors are sensitive to γ-rays, are rugged and have good energy resolution in the MeV region, but not in the tens to hundreds of keV energy region. For applications where spectral line studies are of interest, it is desirable to obtain energy resolutions of the order of 9% at 60 keV. Therefore, semiconductors are the preferred choice of detectors. Silicon (Si) detectors are sensitive only at low x-ray energies, while Germanium (Ge) is the best detector material for hard x-ray and γ-ray spectroscopy. But, it requires cryogenic cooling to reduce leakage currents and thermal noise.

For a planetary mission of limited lifetime like Chandrayaan-I, where propellant fuel is at a premium, payload weight has to be stringently controlled. Therefore, the compound semiconductor Cadmium-Zinc-Telluride (CZT, with $Cd_{1-x}Zn_xTe$, x=0.1 is the blending fraction of Zn) is the primary detector chosen for the HEX experiment. The table(1.1) compares some of the properties of Si, Ge and CZT detectors

Material	Band gap (eV) at 300K	Energy/e-h pair (eV)	Z	density g/cm^3
Si	1.11	3.61	14	2.33
Ge	0.67	2.96 (90K)	32	5.36
CZT	1.57	4.5	50	5.78

Table 1.1: This table compares the properties of some semiconductor materials, commonly used as radiation detectors. The various properties are the band gap energy in eV, the minimum energy required to create an electron-hole pair in eV, and atomic number (Z), and the density in g/cm^3

A detailed discussion on the properties of the CZT detector and its advantages over conventional semiconductor detector materials is given in chapter 4.

The anti-coincidence detector (ACD) of the HEX experiment is a Cesium iodide scintillator detector, doped with Thallium (CsI(Tl)). A scintillator is a material that has the property of emitting light when high energy radiation interacts with it. In the case of the HEX experiment, the light emitted by the detector is collected by a pair of side-mounted photomultiplier tubes (PMTs). The design parameters to be noted while choosing a scintillator for a space-based experiment are

- A scintillator crystal with high scintillator light output is required, in order to obtain good photoelectron statistics.
- The crystal should be non-hygroscopic so as to avoid sealing it in hermetic containers.
- The crystal should be rugged and should not crack or cleave under mechanical stress.

The commonly available scintillator that complied with the above criteria is CsI(Tl). Details of this detector are elaborated in chapter 3.

The main goal of the HEX ACD is **Compton suppression and background rejection of CZT events by anti-coincidence logic**. This will be discussed in detail in chapter 3. In addition to this, a coarse pulse height spectrum can be derived using a four channel counting system, covering energies from 30 keV to greater than 250 keV. This is realized using discriminator circuits.

HEX is a collaboration between the Physical Research Laboratory (PRL), Ahmedabad, and the Space Astronomy Group (SAG), ISRO Satellite Centre, Bangalore. The CZT detector and its associated electronics have been developed at PRL, while the ACD, its electronics and the processing electronics package for HEX have been developed at ISRO Satellite Centre.

The instrumentation employed for each of the detector systems discussed here will be elaborated in section 1.2. The next section deals with the principle of radiation detectors, the electronic systems used in the measurement and recording of signals generated by detectors and the physical processes of interaction of radiation with matter, which produce these signals.

1.1.3 Principles of Radiation Detection

Different types of detectors are used to detect radiation of various types and energies. Gas filled detectors are most often used as low energy photon detectors and they can be designed so as to have large collecting areas. Inorganic scintillation detectors also have large collecting areas and have good stopping power for high energy photons due to their high values of atomic number (Z) and density. Organic scintillation detectors are used to detect charged particles and neutrons. Semiconductors detectors are widely used in photon spectroscopy due to the excellent energy resolution they provide.

The interaction of radiation with a material causes it to lose energy in the material through various physical processes that depend on the interaction cross sections for one or more processes to take place. These cross-sections are functions of

- energy of the radiation
- properties of the material, like the density, atomic number, etc

The radiation emission process is statistical in nature and so is the process of energy loss of the incident radiation in the absorbing material. All radiation detection processes therefore deal with random events and the analysis and interpretation of the detector response to these events must take this stochastic nature into account.

A material is **sensitive** to a particular kind of radiation when it produces a detectable or measurable signal when that radiation interacts with it. Therefore, another important fact while considering the design of radiation detectors is to consider the unique interaction characteristics of different types of radiation of different energies with various materials, in order to increase the sensitivity of the measurement.

The interaction of a photon in a detector is characterized by the generation of an amount of charge - electron and ions/holes (ions for gases and holes for solids), called a **charge carrier pair**. An electric field applied across the detector causes the charges to drift towards their respective electrodes. Complete collection of charge forms the basic electric signal that is representative of the energy deposited by the incident radiation in the detector. The time for charge collection varies from detector to detector, and depends on the

- mobility of charge carriers within the detector
- distance that the charge carrier has to travel from the point of generation to the collecting electrode

When the charge carriers move under the influence of the applied electric field, a burst of current is produced and the time integral of this current is the total charge Q, proportional to the energy deposit in the detector. A voltage pulse is produced when this charge is integrated over the capacitance of the external circuitry. Its amplitude is proportional to the energy deposited by the photon in the medium.

Taking into account the statistical nature of the radiation emission and interaction processes, a photon of energy E interacting with the detector material produces a mean number of charge carriers N. Depending on the type of material used, a minimum amount of energy is required to produce a charge carrier pair by the detector. If this minimum amount of energy is denoted by w, then the mean number of charge carriers, N can be written as

$$N = \frac{E}{w}$$

Thus,

- for different types of detectors (varying w), radiation of the same type and energy, produce different N; smaller the value of w, larger the value of N
- for the same detector type (same w value), radiation of different types and energy produce different N; larger the incident energy, larger the value of N

The production of charge carriers in the detector is a Poissonian process, therefore every interaction produces a number of charge carriers that follows the distribution $N \pm \sqrt{N}$, where $\sqrt{N}$ defines the **statistical fluctuations** in the charge carrier production process. This translates into fluctuations in the amount of charge that is collected by the measurement system, and the subsequent voltage pulse height, at the end of each event. For a Poissonian process, the mean is equal to the variance, and so in the charge carrier production process, the variance is given by

$$\sigma_{stat}^2 = N = \frac{E}{w} \tag{1.1}$$

The distribution of the voltage pulse amplitudes is called the **differential pulse height spectrum**. The x-axis of the distribution is the amplitude of the pulse, and the y-axis is the number of pulses ΔN that are counted in one amplitude bin ΔV, divided by ΔV. Using the pulse height spectrum, the energy distribution of the incident radiation can be studied. The instrument has to be **calibrated** with respect to energy - one must study the pulse height spectrum recorded by a particular detector as a function of known energies. One must measure the peak pulse height corresponding to the incident energy, and then find the relation between the energy and the peak pulse height. Using this relation, the pulse height spectrum that is measured by the detector system can be converted from the voltage space to the energy space. The pulse height spectrum that is produced in the detector due to monoenergetic radiation is called the **spectral redistribution function** (SRF) of the detector for that energy.

The SRF of a particular detector to radiation will vary with

- type of incident radiation - photons, protons, electrons, or alpha particles, i.e, the radiative probabilities for various interaction processes

- energy of the radiation
- detector material
- geometry of the detector configuration

The **energy resolution** of a detector is defined as its ability to separate two closely spaced energies in a pulse height spectrum. As discussed earlier, the mean number of charges produced by a photon of energy E is N, which is distributed as N ± $\sqrt{N}$. This statistical fluctuation $\sqrt{N}$ results in a **minimum and non-reducible** amount of spread in the final charge collected and hence, in the measured energy. For typical photon energies, the photopeak response to monoenergetic radiation is well approximated by a Gaussian as shown in eqn(1.2)

$$P(E) = \frac{A}{\sigma\sqrt{2\pi}} \exp\left(-\frac{E - E_0}{2\sigma^2}\right) \tag{1.2}$$

Here, P(E) defines the photopeak response to incident photon energy E_0 and σ is the **standard deviation**. σ is the **spectral width parameter** and can be defined in terms of the **full-width-at-half-maximum (FWHM)**. It represents the **width of the distribution** or the amount of fluctuation. For a Gaussian,

$$\mathrm{FWHM} = 2.35\sigma \tag{1.3}$$

The resolution of a detector for a particular energy E is expressed as

$$\begin{aligned} R(E) &= \frac{\mathrm{FWHM(E)}}{E} \\ &= \frac{2.35\sigma(E)}{KN} \end{aligned}$$

where K is the proportionality constant between the measured energy and the number of generated charges. Using eqn(1.1), this can be written as

$$\begin{aligned} R(E) &\propto \frac{2.35\sqrt{N(E)}}{N(E)} \\ &\propto \frac{2.35}{\sqrt{N(E)}} \end{aligned} \tag{1.4}$$

From this it can be seen that the resolution improves with larger N. As discussed earlier, this can happen either for large energies or small values of w.

Experimentally measured values of σ^2 which arise from statistics of charge carrier generation (the “intrinsic detector noise”), are found to be smaller than the theoretically calculated values from eqn(1.1). This indicates that the processes that lead to the generation of the final charge are not completely independent of each other.

The deviation of this measured intrinsic variance, σ_{int}^2 from the Poissonian value σ_p^2 has been corrected for by the inclusion of the **Fano factor, F**, where

$$F = \frac{\sigma_{int}^2}{\sigma_p^2} \tag{1.5}$$

The value of F is less than unity for semiconductor and gas detectors, but is unity for scintillator detectors.

The total energy spread in a detector is the quadrature sum of the spread due to various sources. These sources are

- the intrinsic variance or "Fano noise", which can be written using eqn(1.1), as

$$\begin{aligned} \sigma_{Fano}^2 &= \sigma_{int}^2 = F\sigma_p^2 \\ &= F\frac{E}{w} \end{aligned} \tag{1.6}$$

- the noise due to the electronics system that processes the signals. This noise is expressed as **equivalent noise charge (ENC)**, Q_{enc}. This is defined as the amount of charge, if applied to the input terminals of the system, that produces an output voltage which corresponds to the noise only. The unit of Q_{enc} is "number of electrons".

$$\sigma_{ENC}^2 = \sigma_{ENC}^2 = Q_{enc}^2 \tag{1.7}$$

Therefore, the total spread, σ_{tot}^2 is

$$\begin{aligned} \sigma_{tot}^2 &= \sigma_{Fano}^2 + \sigma_{ENC}^2 \\ &= F\frac{E}{w} + Q_{enc}^2 \end{aligned} \tag{1.8}$$

From this one can write the energy spread in terms of FWHM

$$\begin{aligned} \text{FWHM(E)}_{tot} &= 2.35\sigma(E)_{tot} \\ &= 2.35\sqrt{\sigma(E)_{tot}^2} \\ &= 2.35\sqrt{F\frac{E}{w} + Q_{enc}^2} \end{aligned} \tag{1.9}$$

Therefore, the energy resolution can be written as

$$\begin{aligned} R(E) &= \frac{\mathrm{FWHM(E)}}{E} = \frac{\mathrm{FWHM(E)}_{tot}}{E}\,w \\ &= \frac{2.35\,w\sqrt{F\frac{E}{w}+Q_{enc}^2}}{E} \\ R(E) &= \frac{2.35}{E}\sqrt{FEw+w^2Q_{enc}^2} \qquad (1.10) \end{aligned}$$

Unless the **efficiency** of the detector is known, the number of pulses counted from the pulse height spectrum cannot be related to the actual number of photons entering the detector.

Quantum Efficiency is defined as the ratio of the number of pulses counted by the detector system to the number of photons incident on the detector. This efficiency depends on the detector properties and the energy of the incident radiation.

If all the pulses recorded in the pulse height spectrum are counted irrespective of their amplitude, the counting efficiency is called the **total efficiency**. If only those pulses that arise from full energy deposition events in the detector are counted, then the efficiency is called the **photopeak efficiency**. The incident intensity of radiation can thus be measured if the efficiency of the detector is known.

Another parameter of importance is the concept of **dead time**. The processing of each event takes a finite amount of time, of the order of tens of microseconds. This time 'τ' depends on the duration of the signal pulse and the electronics processing time. When a single event is detected by the detector and is being processed, the detector may or may not take into account a second event that occurs within τ.

A detector system that is sensitive to the second event during the processing of the first one is called a **paralyzable** system. In this case the second event adds its own dead time to that of the first event. For high event rates, the dead times of many consequent events can overlap, resulting in a sustained period during which signal processing becomes suspended. The system is then paralyzed. This results in signal distortion and information loss due to pile-up of successive events on the first one.

A detector system that is insensitive to the second event during τ is called a **non-paralyzable** system. In this case, the second event is not considered while the first is being processed. Once τ has passed, the system is ready to accept new events. The detectors of the HEX experiment are non-paralyzable systems.

For a non-paralyzable system, in order to obtain the true count rate from the measured count rate, one must always account for dead time corrections. If the true count rate is 'n' and the measured count rate is 'm' for a dead time of 't', one can determine the true count rate by the following equation (from [4a])

$$n = \frac{m}{1 - mt} \tag{1.11}$$

For space-based experiments, an important parameter is the limiting **sensitivity** of the instrument. Sensitivity is defined as the minimum detectable flux F_{min} of a detector at a chosen SNR above the background counts. This is significant especially in those cases when the signal flux is comparable with the fluctuations in background counts during a particular period of observation. Consider a source with flux given by F(E) photons $cm^{-2}s^{-1}keV^{-1}$ incident on a detector of area A cm^2 with efficiency ϵ(E). Let B(E) be the background counts in units of counts $cm^{-2}s^{-1}keV^{-1}$ such that the incident flux is comparable to ΔB, which is the variation of background counts in time period T seconds. Then, for an SNR three times above the background, the sensitivity can be expressed by

$$F_{min} = \frac{S}{\epsilon}\sqrt{\frac{\epsilon B(E)}{AT\Delta E}} \tag{1.12}$$

in units of photons $cm^{-2}s^{-1}keV^{-1}$, where ΔE is the energy range of interest.

1.1.4 Instrumentation for Radiation Detection and Measurement

The input to the electronics processing chain that forms an integral part of the instrumentation for radiation measurement is the charge output of radiation detectors. The various components of the instrumentation are briefly discussed below

- **The Charge Sensitive Pre-Amplifier (CSPA)** - The preamplifier circuit is the interface between the detector and the rest of the processing electronics. Its main role is to drive the weak signals through the cables connecting to the rest of the circuit, adding the least amount of noise. This is normally done by mounting the preamplifier as close to the detector as possible. There are three types of preamplifiers; current sensitive, voltage sensitive and charge sensitive. The current sensitive preamplifier is normally used with low impedance devices and so is not used with radiation detectors which are high impedance instruments.

  The output of a voltage sensitive amplifier depends on the capacitance of the detector and other stray capacitances at the input. These preamplifiers are not used with semiconductor detectors because the capacitance of these detectors can vary due to various factors.

  In a CSPA the detector capacitance does not contribute significantly to the output voltage pulse, and is therefore most widely used in spectroscopy. A simple circuit diagram of a CSPA and detector system is given in fig(1.1) The CSPA consists of

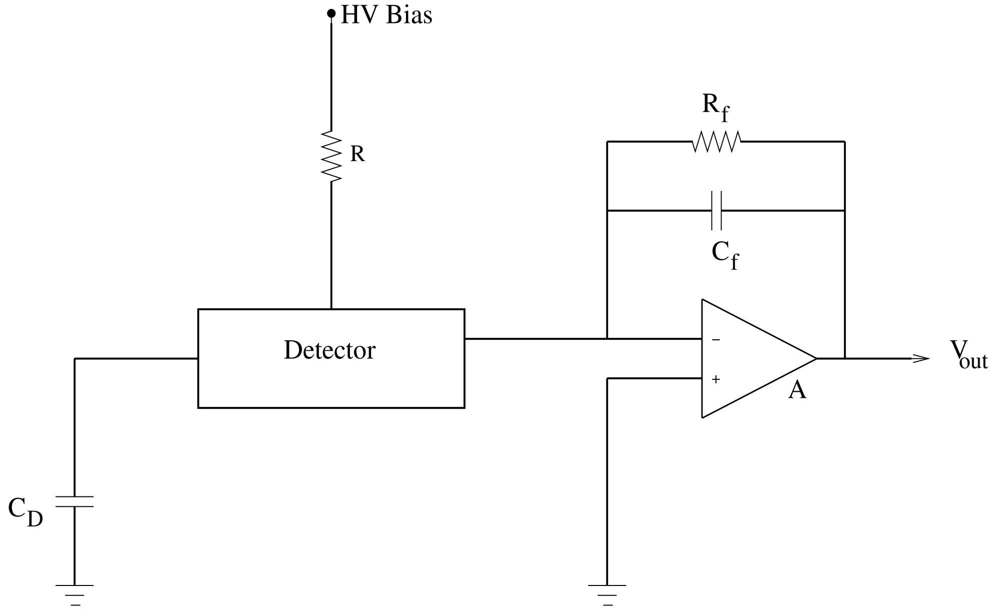

FIGURE 1.1: Circuit diagram of a detector and pre-amplifier system. In the figure, R is the load resistor, R_f and C_f are the feedback resistor and capacitor, respectively. 'A' is the open loop gain of the operational amplifier. C_D is the detector capacitance.

an inverting amplifying circuit. The feedback capacitance C_f is seen at the input as $(A+1)C_f$ and is in parallel with C_D which represents the detector capacitance and other stray capacitances. Therefore, the effective capacitance is given by $C_D + (A+1)C_f$.

Since this is an inverting amplifier circuit,

$$V_{out} = -AV_{in} \tag{1.13}$$

where V_{in} is the input voltage and A is the open loop gain of the op-amp. V_{in} can be written as

$$V_{in} = \frac{Q}{C_{eff}} \tag{1.14}$$

Here, Q is the charge output of the detector which is proportional to the energy deposited by the incident radiation, and C_{eff} is the effective capacitance as described earlier. Therefore eqn(1.13) can be written as

$$\begin{aligned} V_{out} &= -A\frac{Q}{C_{eff}} \\ &= -A\frac{Q}{C_D + (A+1)C_f} \end{aligned} \tag{1.15}$$

For large values of A, the denominator in eqn(1.15) can be approximated to C_f and therefore the output of the CSPA is given by

$$\begin{aligned} V_{out} &= -A\frac{Q}{AC_f} \\ &= -\frac{Q}{C_f} \end{aligned} \tag{1.16}$$

The output signal is a pulse with a very short rise time, of the order of nanoseconds and a long decay time, of the order of tens to hundreds of microseconds.

- **The Shaper-Amplifier (SA)** - The output voltage signal of a CSPA is a weak exponential pulse with a fast rise time and a slow decay time. These pulses are amplified and shaped by amplifiers into output pulses that are suitable for further processing. Proportionality has to be maintained between the input and output amplitudes. If the CSPA output pulse is amplified without shaping, the pulse shape is preserved, which poses certain problems for spectroscopy in the form of
  - low and high frequency noise components.
  - distortion of pulse shape and subsequent information loss; this happens when a second pulse arrives before the first pulse has decayed. This results in the second pulse riding on the long tail of the first pulse causing its amplitude to increase.

In pulse shaping, the total length of the CSPA output pulse is reduced, keeping its maximum amplitude intact. Pulse shapers consist of integrator (RC) and differentiator (CR) networks. The CR network is a low pass filter which decreases the duration of the pulse, reducing its decay time. This is followed by an RC network which is a high pass filter, and it increases the rise time of the pulse, allowing the amplitude information to be maintained for a longer time. Thus, CSPA output pulse is shaped improving the signal-to-noise ratio (SNR) characteristics considerably, as the pulse is now limited to only those frequencies that contain useful information.

Shaping circuits are characterized by the **time constant** which is the product of R and C (R in Ω and C in farads). The fig(1.2) is a schematic of the a simple CR-RC circuit. The shaped pulse is then amplified by a linear amplifier to an

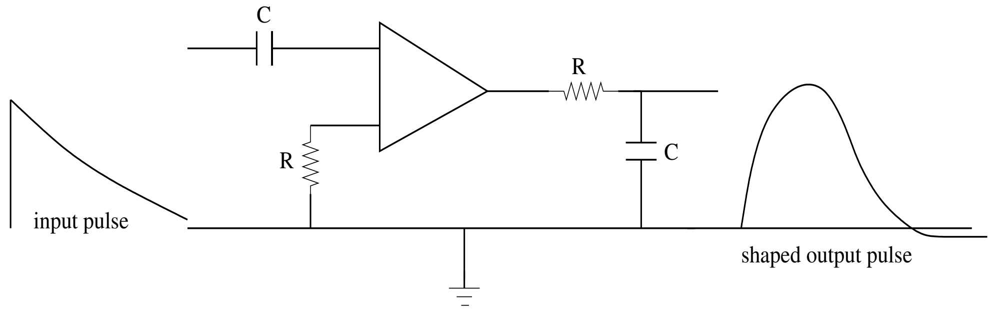

Figure 1.2: This is a schematic of the CR-RC shaper circuit. The input pulse is shown with fast rise time and slow decay. The first stage is the CR differentiator, followed by the op-amp and the RC integrator. The shaped output pulse is also shown.

output pulse within a specific amplitude range (usually between 0-10 V). If the product of the input amplitude and the gain of the amplifier exceeds 10 V, then the pulses begin to saturate. The system therefore exhibits linear behavior only for those pulses which have amplitudes below the saturation limit.

- **Analog-to-Digital Converter (ADC)** - The ADC performs a linear conversion of the input analog pulse amplitude, to a digital number called **channel**. An 8-bit ADC will generate 2^8 numbers over its input range, i.e. 256 bins, while a 10-bit ADC generates 2^{10} or 1024 bins. So, the greater the number of digital bins, smaller will be the number of input voltages each bin corresponds to. This defines **digital resolution**. The number of bits chosen for an ADC depends very strongly on the SNR of the input. Therefore, one can characterize the ADC performance based on

  - speed of conversion from analog voltage to digital number
  - linearity between analog voltage and number
  - digital resolution corresponding to the maximum range of input voltages available for conversion

  The ADC is one of the components of a multi-channel analyzer.

1.1.5 Interaction of Particles with Matter

Ionizing radiation can be divided into **charged** radiation, which interacts with matter via Coulomb forces, and **neutral** radiation, which produce secondary charged particles. The interaction processes of these particles in matter is briefly described below

1.1.5.1 Charged Radiation

- **Heavy Charged Particles**

These are particles whose rest masses are greater than that of the electron, like protons, alpha particles, fission fragments and mesons. The interaction is mainly through collisions with atomic electrons in the material medium via the Coulomb force. These collisions are inelastic; energy is transfered from the interacting particle to the electrons in the atom, either exciting them to higher energy levels or knocking the electron out of the atom, resulting in ionization. The kinetic energy loss of the interacting particle per unit distance traveled is called the **stopping power**, -dE/dx (the negative sign indicates energy loss) and is expressed by the Bethe-Bloch formula [4a],

$$-\frac{dE}{dx} = \frac{4\pi e^4 z^2}{m_0 v^2} NB \tag{1.17}$$

where

$$B = Z\left[\ln\frac{2m_0 v^2}{I} - \ln\left(1 - \frac{v^2}{c^2}\right) - \frac{v^2}{c^2}\right]$$

Here

v = velocity of the primary particle
e = electronic charge
N = number density
Z = atomic number of the absorber atoms
I = average excitation and ionization potential of the absorber
ze = charge of the primary particle
m_0 = electron rest mass

From this formula it can be seen that

1. -dE/dx varies inversely with the velocity, v of the particle
2. -dE/dx varies as z^2, where z is the charge of the interacting particle
3. -dE/dx varies with NZ, where N is the number density of atoms in the material, and Z is its atomic number

The **range** of a particle is the distance in the absorbing material, beyond which no particle will penetrate, i.e. the particle is fully stopped. The thickness of material which reduces incident particle flux to half its value is called the mean range. Every particle of a particular energy has a specific range for a material.

- **Electrons and Positrons**

  High energy electrons interact with atomic electrons in a medium via Coulomb forces, just like other charged particles, but there are differences in the rate of energy loss. This is due to the small mass of the electrons. In order to accommodate these differences the Bethe formula is modified as

$$
\begin{aligned}
-\left(\frac{dE}{dx}\right)_c =& \frac{2\pi e^4 NZ}{m_0 v^2}(\ln \frac{m_0 v^2 E}{2I^2(1-\beta^2)} \\
& - (\ln 2)(2\sqrt{1-\beta^2} - 1 + \beta^2) + (1-\beta^2) \\
& + \frac{1}{8}(1-\sqrt{1-\beta^2})^2)
\end{aligned}
\tag{1.18}
$$

  where β = v/c, with c representing the velocity of light.

  Beyond a critical energy E$_c$, the loss of electron energy due to emission of radiation or bremsstrahlung starts to dominate the energy loss of electrons, and is given by

$$E_c \simeq \frac{800}{Z+1.2}\text{MeV} \tag{1.19}$$

  Positrons have the same mass as electrons, except that they have the opposite sign. They also lose energy in a material by collisions via the Coulomb force, exciting and ionizing atoms in their path. Once they are slowed down to rest, they interact with an electron of the medium via annihilation, producing two photons each of energy 0.511 MeV, emitted in opposite directions.

1.1.5.2 Neutral Radiation

Photons and neutrons do not interact with matter via the Coulomb force. The end products of the interaction of neutral radiation with matter are charged particles, which interact with matter as discussed previously.

- **Photons**

  Interaction of a photon in matter either results in its complete disappearance or annihilation, or in it undergoing scattering and losing energy in the process. The processes that are important in removing photons from an incident beam are

  1. **Photoelectric effect-** This process dominates for low energy photons ($\leq$ 100 keV) and materials composed of high atomic number elements. The probability of photoelectric absorption per atom is given by

$$\sigma_{phot} \propto \frac{Z^n}{E^3} \tag{1.20}$$

where
E = energy of the incident photon
Z = atomic number of the medium
and n varies between 4 and 5.

In this process, an electron from the inner electronic shells is ejected, and this is the photoelectron. Its energy is given by

$$E_{e^-} = h\nu - BE \tag{1.21}$$

where $h\nu$ is the energy of the incident photon, and BE is the binding energy of the electronic shell, with which the interaction takes place. The atom relaxes to the ground state by the rearrangement of its electrons, emitting x-rays (fluorescence effect) or electrons (the competing Auger effect) in the process. The energy of the emitted radiation is characteristic of the element.

2. **Compton scattering** - Interactions by Compton scattering occur between the photon and a loosely bound electron. The one characteristic of the material that influences the probability of Compton scattering is the number of available electrons, i.e. the probability of Compton scattering per atom, σ_{Cs}, depends linearly on Z.

   Detailed discussion on this interaction process is given in section 3.4.

3. **Pair-production** - This interaction process is dominant for those photons with energy in excess of 1.022 MeV. The photon is subjected to the nuclear field of the atom in the material through which it is traveling, and is annihilated, resulting in an electron and a positron. The nucleus is not excited by the passage of the photon, but plays a passive role in which it helps in conserving the energy and momentum of the reaction. The state of the nucleus before and after the event is largely unchanged, except for a very small increase in the kinetic energy and momentum. The electron and positron are created from the energy of the incident photon, according to $E = mc^2$. Since the 1.022 MeV is rest mass of the electron and the positron (each having 0.511 MeV), the extra energy of the photon is imparted to the two particles as kinetic energy.

$$E_{e^-} = E_{e^+} = \frac{h\nu - 1.022}{2} \tag{1.22}$$

   where $h\nu$ is the energy of the incident photon. The probability of this interaction process, σ_{pp}, increases with increasing energy, and varies as the square of the atomic number, Z.

When one of the above interaction processes removes a photon from the incoming beam, the intensity is said to be attenuated. The attenuation is quantified by the rate of interactions in the material over unit distance, and is called the linear attenuation coefficient, μ in units of cm^{-1}. It defines the fraction of photons interacting in a unit length of material and is inversely related to the average distance the photons travel in the material before interacting. The total attenuation is a sum of the individual interaction probabilities

$$\mu = \sigma_{phot} + \sigma_{Cs} + \sigma_{pp} \tag{1.23}$$

If I_0 is the initial intensity of a beam of photons of energy E, passing through a material of thickness x, I_0 falls off exponentially through the absorbing material, as

$$I = I_0 \exp(-\mu x) \tag{1.24}$$

where I is the final intensity of the beam. The linear attenuation coefficient is most often expressed as a photon attenuation rate in terms of the amount of mass the radiation encounters, rather than the distance it travels. This is the mass attenuation coefficient, μ_m, related to μ by

$$\mu_m = \frac{\mu}{\rho} \tag{1.25}$$

where ρ is the density of the material (g cm^{-3}). The mass attenuation coefficient has the unit of cm^{2}g^{-1}.

Photons can also interact with matter via the Rayleigh effect, which is the elastic scattering of photons with matter, where photons do not lose energy, but undergo change in direction. This process is effective in reducing the intensity of narrowly collimated beams.

Another process by which photons interact with matter is by nuclear photodisintegration. High energy photons are annihilated when they are absorbed by a nucleus, causing it to enter an excited state. The nucleus de-excites immediately resulting in a daughter nucleus and the emission of subatomic particles, like protons, neutrons or α particles.

- **Neutrons**

  Neutrons interact with the nuclei of atoms of the material through which they pass. Since the short range nuclear force governs these interactions, they have to take place when the neutron is very close to the nucleus. This results in the interaction cross sections for neutrons to be very small, given the small size of the nucleus relative to the atom. Hence, neutrons travel a long way in matter before finally interacting. The physical processes of interaction depend on the energy of the incident neutron, which can range from a few eV to several MeV.

1. **Spallation** - This takes place at energies greater than 100 MeV, where the neutron strikes a nucleus, and produces a shower of secondary particles.
2. **Elastic Scattering** - Here, the neutron collides with the nucleus and bounces off, imparting some of its kinetic energy to it. With each collision, the energy lost by the neutron is gained by the nucleus. Elastic collision with a massive nucleus causes the incident neutron to lose very little energy, while collision with a light nucleus produces the opposite effect. This is why light materials are effective in slowing down neutrons (like Hydrogen).
3. **Inelastic Scattering** - In this case, collision with the nucleus results in the formation of a compound nucleus, which is unstable. It then decays with the emission of a neutron of lower energy, and a γ-ray, which takes up the remaining energy.
4. **Radiative Capture** - In this reaction, the neutron is captured by the nucleus, which de-excites with the emission of a γ-ray. This is one of the most common neutron reactions, and is most important for neutrons with very low energies, i.e. thermal neutrons.

The different types of radiation detectors used in experimental studies are discussed in the next section.

1.1.6 Types of Radiation Detectors

Radiation detectors can be based on gases, liquids and solids. Gas detectors can be ionization chambers, proportional counters or Geiger counters. Detectors based on liquids are mostly scintillators, while solid detectors are either scintillators or semiconductor detectors. The features of most commonly used detectors are summarized below

- Proportional counters
  In these detectors, the anode is surrounded by the cathode, either in a cylindrical geometry or in a multi-wire arrangement. The operating voltage is high enough to cause electron multiplication in the vicinity of the anode, with the multiplication factor as high as 10^6. The voltage pulse height that is measured is proportional to the energy of incident radiation. It is possible to distinguish between different incident particles using these detectors based on the pulse rise-time or pulse shape.

- Scintillators

  These are solids or liquids whose atoms are excited by incoming radiation. These atoms emit visible radiation when they de-excite to the ground state. If such a material is optically coupled to a photomultiplier tube or some device capable of detecting visible light, the optical photons emitted by the scintillator can be collected and converted to an electrical signal. The details of scintillators and their operation are elaborated in chapter 3.

- Semiconductor detectors

  These are essentially reverse biased p-n junctions. When ionizing radiation passes through the junction and interacts, electrons are excited into the conduction band and holes are created in the valence band. The applied electric field (with the internal junction potential) sweeps the electrons to the positive n-side and the holes to the negative p-side, resulting in the generation of a voltage pulse. The details of the operation of these detectors is discussed in chapter 4.

Thus far, the principles of radiation detectors and their associated electronics have been discussed. The different types of radiation and the ways in which they interact with matter have also been reviewed, along with a summary on the different types of radiation detectors. In the next section we discuss the HEX instrument on Chandrayaan-I.

1.2 The HEX Instrumentation

HEX payload consists of two parts

- The detector package, which has a stainless steel collimator, Cadmium-Zinc-Telluride (CZT) primary detector, a CsI(Tl) anti-coincidence detector (ACD) and associated analog electronics.
- The processing electronics package consisting of FPGA-based digital electronics, including interfaces with spacecraft telemetry and telecommand systems.

1.2.1 Mechanical Configuration of the detector package

Figure (1.3) shows the mechanical design of the HEX payload The contents are listed in table 1.2

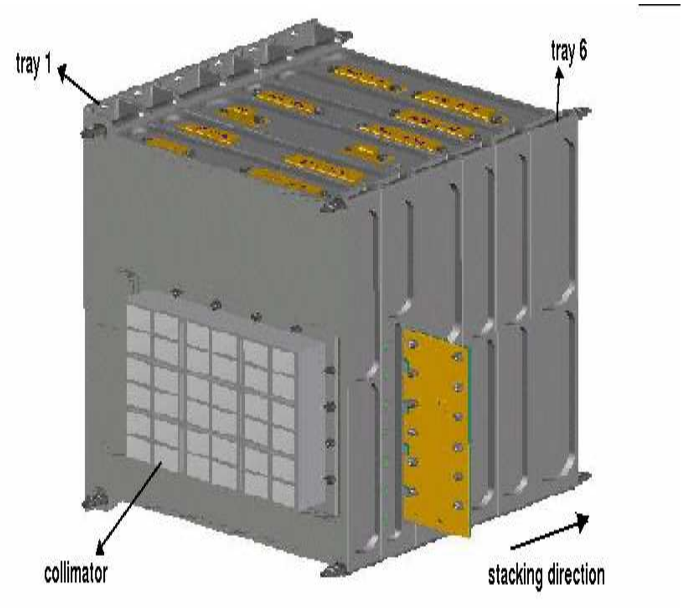

FIGURE 1.3: HEX payload; the collimator is indicated by the label, and the direction of tray stacking is also shown. The trays 1 and 6 have been marked in the figure. The collimator is made of stainless steel with the aim to restrict the field of view of the instrument.

Tray 1	power filter for the CZT ASIC bias + CSPA for ACD + Stainless steel collimator
Tray 2	CZT detector board
Tray 3	ACD + HV units for ACD, CZT
Tray 4	Front-end-electronics (FEE) for CZT signals
Tray 5	ACD electronics
Tray 6	All DC/DC converters (5)

TABLE 1.2: Break-up of the HEX instrument trays

1.2.2 The HEX Primary Detector

As discussed in section 1.1.2, the primary detector for the HEX experiment is the CZT compound semi-conductor detector, manufactured by Orbotech Medical Imaging (IMARAD), Israel. Each detector module has dimensions of 40 mm × 40 mm × 5 mm. For the HEX experiment, nine such detectors are mounted in a 3×3 matrix in tray 2 of the HEX package. Each module has a pixellated readout or anode, consisting of 256 pixels, arranged in a 16×16 array. Each anode has dimensions of 1.86 mm × 1.86 mm, with a pixel pitch of 2.46 mm. Each CZT module is mounted on a substrate, below which two ASICs (Application Specific Integrated Chips) are bonded. The ASICs are XAIM 3.3 from IDEAS, Norway. It is a low noise device, designed on a self-triggered and data driven concept. Each ASIC has 128 circuits, called "channels" which can process signals from 128 pixels. The detector pixels are bonded directly to the ASIC channels.

Two ASICs are bonded to one CZT detector module to handle signals from 256 pixels simultaneously.

Each ASIC has a CSPA, a SA, peak detector (PD) and level discriminator. The CSPA is the first stage of the ASIC channel and it converts the charge produced in the detector by incident radiation, into a voltage pulse. The output of the CSPA has a sharp rising edge (nanoseconds) and a very long tail. This “tail” pulse is next passed to the SA, where the pulse is shaped to a Gaussian in order to improve the energy resolution. The SA consists of a first order CR-RC filter which provides the shaping, and also a gain factor to increase the amplitude of the voltage pulse. The shaped pulse is then passed to the PD, to hold the amplitude information. This output is then passed to a comparator circuit to identify whether the signal is above the set threshold of detector. Once this happens, the comparator produces a trigger pulse, which in turn generates the pre-defined address of the channel.

Signals which cross the threshold are accepted and the output of the channel will be the energy and position information of the hit channel. The threshold is programmable. The trigger information is also available at the ASIC output, so that the user can identify the occurrence of the event.

1.2.3 The HEX Anti-Coincidence Detector (ACD)

As discussed in section 1.1.2, the HEX ACD is a CsI(Tl) scintillation detector. The CsI(Tl) crystal used has dimensions of 14 cm × 14 cm × 1 cm, procured from SCIONIX. It is placed directly below the CZT detector. The light emitted by the crystal is read out by two side mounted PMTs, powered by a single HV (high voltage) unit. The PMTs have a diameter of 1 inch, with bialkali photocathodes, and 10 dynodes. The PMTs are optically coupled to the CsI(Tl) crystal using light guides. The light guides are prisms, which are coupled to the crystal and the PMT using optical grease. The scintillation light reaches the PMT photocathode by total internal reflection in the prisms.

The HV unit supplies a bias of 690 V, which is distributed to all the dynodes through a voltage divider network. An DC/DC converter, which takes raw power from the spacecraft, provides regulated voltage to the HV circuit. The HV unit has a corona auto-shutoff feature - when the current drawn by the circuit becomes more than 1.5 times the nominal current, it is considered as a corona condition and the HV is shut off, thus providing safety to the spacecraft power bus. The output of the PMTs are summed and fed to the input of CSPA. The CSPA produces a voltage that is proportional to the charge output of the detector system, which in turn is proportional to the energy deposited in the detector.

The CSPA used in the system is Amptek's A203 chip. The CSPA output is unipolar and is further shaped and amplified using LM118 op-amp. The output of the shaper-amplifier circuit is fed to the window discriminator circuits. The ACD has four windows or channels. The comparator used for the discriminator is LM139. Each window is defined by a low level discriminator (LLD) and an upper-level discriminator (ULD). The voltage level at the LLD and the ULD corresponds to a specific energy in the energy range 30-250 keV. Once the input signal crosses the LLD, and its amplitude is less than the ULD, the ACD signal is generated as a digital pulse of amplitude +5V and duration 5.5 μs. When the input crosses ULD, the ACD output becomes 0. The output of the window discriminator is the output of the ACD. The output of the four windows are fed to the processing electronics.

As mentioned earlier, this thesis deals with optimization of detector design using the Geant4 simulation toolkit, the characterization of the HEX detectors, and the use of the detector spectral parameters to simulate the response of the detectors. The next section deals with simulation in general, and Monte Carlo simulation in particular.

1.3 Role of Monte Carlo Simulations

1.3.1 Why simulate ?

Simulation is used to predict the ways in which a system will evolve and respond to its surroundings. Simulation is a powerful and important tool because it provides a way in which alternative designs and plans can be evaluated without having to actually experiment on a real system, which may be extremely expensive, time consuming or even impractical to do. Simulation can be used to model systems in order to understand their functioning. Issues like performance optimization of technology can also be achieved through simulation, which feeds to subsequent alteration of design. Simulations also help in filling in the calibration phase space that may not be accessible through the existing laboratory set up.

The various steps involved in simulations are

1. Consolidate information about the physical entity to be simulated. These are the input parameters of the simulations, used to model the system.
2. Out of these input parameters, certain key elements are selected to study sensitivity effects. The behavior of the system can be studied through alterations of these select input parameters.

3. Simplifying approximations and assumptions are defined to limit the complexity or granularity of the simulation model. It saves time.

Simulations are used in engineering and technology for studying the performance of systems with many processes - in this case performance optimization is the main goal.

Models are mathematical, or logical representations of reality, and simulations are the specific applications of these models to derive realistic results. Models can also represent processes created from data, and equations that imitate or mimic the actions of systems or objects represented. Models can be simple, or complex, carrying all the information about the object that is to be simulated. Validation of the simulation results against the real-world system is essential for fine tuning the model, so that the simulated behavior matches the real-world behavior, within tolerance limits.

In the field of space science, simulation is extremely useful in design optimization, and one example is the optimization of shielding geometry. Shields are used to protect sensors and electronics systems from ambient space radiation. Conservative shielding geometries are used often and contribute significantly to the weight of the payload. Simulations help the designer to compute the shielding efficiency and determine the optimum shielding thickness that is essential, that keeps the weight of the system within tolerable limits. Another example of application in space science is simulation of sensor response over a range of energies or wavelengths. A few measurements taken in laboratory conditions are used in simulations to derive the system response. Once the laboratory system response is simulated and validated with measurements, it provides more confidence in predicting the system response in other conditions across all energies.

The next section discusses the role of Monte Carlo simulations in modeling the background of space-based γ-ray detectors.

1.3.2 Background modeling using Monte Carlo methods: a review

Low to medium γ-ray detectors operated from space-based platforms are immersed in extreme radiation environments. This radiation can interact with the detector and the spacecraft to produce line and continuum background in the detector. This instrumental background must be studied in detail as the instrument sensitivity and derived source intensity are very much dependent on it.

The Apollo 15 and 16 spacecrafts had NaI detectors onboard with the purpose of making accurate measurements of diffuse cosmic γ-rays above 1 MeV. They measured a higher count rate while inboard than when they were deployed outside the spacecraft [7a][8a].

These excess counts are the *locally produced* γ-rays which are due to interaction of cosmic rays with the spacecraft. The Apollo 16 detector showed 15% more counts than that of Apollo 15. The reason for this increase was investigated and it was found that at the time of the Apollo 16 mission there was an enhancement of the low-energy electron flux (3-12 MeV energy range) by a factor of ~ 2 compared with that during the Apollo 15 mission. This finding indicates that background measured in space-based detectors are dependent on the variation of space radiation sources.

The background observed in these detectors is substantial and emphasized the need to devote time and effort in modeling detailed instrument background. Continua would suppress weak lines of interest, while the lines produced as a consequence of induced radioactivity could interfere with spectroscopy of astrophysical and planetary γ-ray energies. Background can be estimated using semi-empirical functions but there are too many uncertainties involved due to the complicated physics involved. Monte Carlo simulations improved upon the accuracy and dependability of these calculations as they combine particle transport through geometries and all the relevant physics.

A comprehensive review is available in [9a] which discusses a general method of approach in the estimation of the total background of a low-energy γ-ray detector system in a particular radiation environment. This paper discusses the different sources of background in ambient space and their temporal and spectral variation. Dean et al [9a] also covered the topic of optimum shield design with respect to shield leakage, activation due to β-decay and elastic neutron scattering. Methods for estimating the background due to these different sources were expostulated upon and results of the calculations were compared with experimentally observed background. They computed the background for the γ-ray detectors of the SMM spacecraft, Apollo 15, SIGNE 2 and comparisons with observations were satisfactory. A few facts obtained from these exercises were that background is very much dependent on the mass in the line of sight of the detector. Dean et al also performed calculations for the background of the GRASP telescope for two types of orbits, HEO (High Earth Orbit, an elliptic orbit, characterized by a relatively low altitude perigee and a high altitude apogee which lies above 35,786 km) and LEO (Low Earth Orbit, orbits that have altitudes generally between 300 km and 1000 km) and studied the dependence of the energy deposited in detectors with inclination and altitude. It was found that in LEO the background was dominated by γ-rays generated in the Earth's atmosphere by cosmic ray interactions, while in HEO the spectrum was dominated by locally produced γ-rays due to cosmic rays. Also the contribution due to trapped protons in the Earth's magnetosphere was dominant for LEO, while it was relatively negligible for HEO. Dean et al briefly discussed different methods to suppress the background. At the end it was understood that background modeling is an extremely important part of payload design, in terms of performance and data analysis.

The advantage of Monte Carlo simulations is that all the complexities of the physics and geometries can be modeled in the detail which is difficult with analytical calculations.

Monte Carlo simulations have been used to simulate the effects of spacecraft shielding against geomagnetically trapped protons and cosmic ray protons in detector materials as discussed in [10a]. Truscott et al have used the Integrated Radiation Transportation Suite (IRTS) to study the production of secondary particles and induced radioactivity in detector materials. This paper discusses the physics required for simulation by comparing simulations with experimental data from shuttle flights and laboratory beam tests. Monte Carlo methods were also used to estimate the γ-ray background of the Burst and Transient Source Experiment (BATSE) [11a] using a mass model of the instrument and spacecraft. The energy dependent background flux in its nine year mission. The Monte Carlo simulation tools MGGPOD[13a] and EGS4 were used by Tajima et al [12a] for the design and performance optimization with respect to background in the 0.1-100 MeV energy range.

MGGPOD is a Monte Carlo software suite used for simulating the background measured by γ-ray detectors, including all the lines due to interaction of various sources of radiation with the spacecraft and detector materials. This can also be used to model instrument response. It was tested by comparing the simulated background of the Germanium detector of the Transient Gamma-ray Spectrometer (TGRS) onboard the Wind spacecraft [14a]. The simulated background consisted of the prompt and delayed background components due to radioactive decay in detector and spacecraft, and the background due to cosmic diffuse γ-rays. The instrumental response was included in the simulation. It was found that the simulation and measurements agree within 30%, with 87% of the lines due to induced radioactivity being reproduced. The background detected by the SPI instrument on INTEGRAL [15a] was also simulated using MGGPOD and it was found that though the overall spectrum was well reproduced, there were some discrepancies due to the handling of thermalization and capture of secondary neutrons in MGGPOD. The background of the RHESSI detectors [16a] was also simulated using MGGPOD and the overall spectrum was well reproduced. Certain additions and improvements have been implemented in the original version of MGGPOD and upgraded to version 1.1, as described in [17a].

Geant4 [18a][19a] is a multiparticle simulation toolkit that has the capability to model complex 3D geometries and transport particles through them, and it includes a wide variety of physics processes and models. Geant4 has been used to estimate the background of a number of space-based γ-ray experiments like XMM-Newton [20a], GLAST [21a], LISA [22a], Suzaku [23a], the Columbus module of the International Space Station [24a]. Geant4 has been used extensively in this thesis for simulation purposes since it has capabilities to model 3D geometries of spacecraft and payloads in great detail, and it has an extensive list of physics processes and models. This is useful from the point of view of studying the processes of background generation in a given detector for a specific radiation source. It is based on object oriented technology (section 1.3.4) which provides a modular framework for the code; this software design enables transparency in physics and allows the test and validation of physical parameters.

In the next section we discuss the logic behind a Monte Carlo algorithm and its application in particle transport codes.

1.3.3 Monte Carlo simulations and Particle Transport Codes

Monte Carlo simulations are used to solve problems that are statistical in nature. It is a numerical method of problem solving that uses random variables, called the method of 'statistical trials' [3a]. A trial is repeated N times, each being independent of the rest; the result of all the trials are then averaged. Error decreases with increasing number of trials. The Monte Carlo method enables the simulation of any problem governed by random processes with the construction of probability models. Figure(1.4) shows a flowchart which is an example of a Monte Carlo algorithm. For particle transport codes, the Monte Carlo method is applied usually to decide which physics process is to be applied to a particle. From the material information of the matter through which the particle has to interact, the number density of atoms is computed. Using this number density and the energy dependent particle interaction cross-sections, the mean free path for each physical process is computed. The step size of a particle in the medium is determined from the mean free path for the process and the number of mean free paths, 'm' for the particle. This number is a random variable, chosen from a pre-defined probability distribution or generated using a random number generation engine. For each physics process, a random number is generated, and using these, the step size for the process is calculated. The process with the shortest step is then selected.

There are many particle transport codes based on the Monte Carlo code available. However, only a few of them are multi-particle codes, i.e. they deal with the transport of all particles - neutrons, protons, ions, electrons, muons, and other subatomic particles, neutrinos, optical photons, x-rays and γ-rays. Of all the codes available, Geant4 which is discussed in chapter 2, is the only one that uses object oriented technology, which has many advantages. The concept of object oriented technology and its advantages are discussed briefly in the next section.

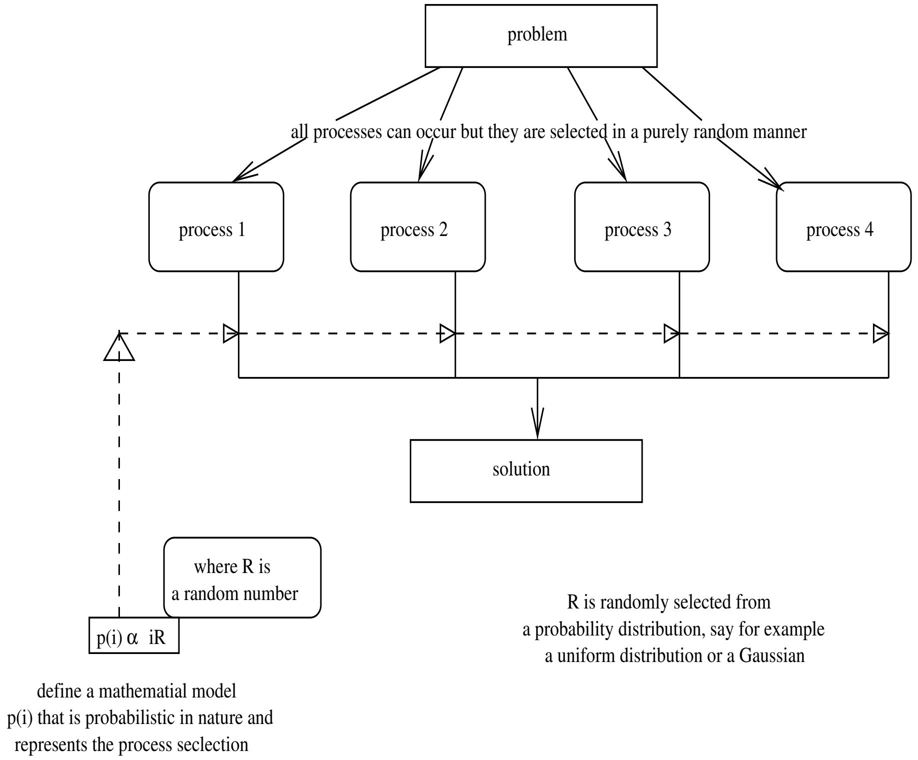

FIGURE 1.4: This flowchart is an example illustrating the basic principle behind a Monte Carlo algorithm.

1.3.4 Object Oriented Programming

Object oriented programming (OOP) uses **objects** which are comprised of code and data. Data is treated as a critical element and is not allowed to flow freely. It is bound closely to the functions that operate on it and is thus protected from accidental modifications. An object is defined by its **class** which is basically a collection of objects of similar types. Once a class is created, any number of objects that belong to it can be created.

The various advantages of OOP are as follows:

1. Modularity - Each object forms a separate entity whose internal workings are decoupled from other parts of the system. The object consists of code and data merged into a single entity and the information it holds is encapsulated or hidden from the rest of the system.
2. Modifiability - It is easy to make minor changes to the functions or procedures in OOP. Changes in a class do not affect any other part of a program, since the

only public interface that the external world has to a class is through the use of methods.

3. Extensibility - Adding new features or responding to changing operating environments can be solved by introducing a few objects and modifying some existing ones.
4. Maintainability - Objects can be maintained separately, making location and fixing of problems easier.
5. Re-usability - Objects can be reused in different programs.

1.4 Author's research areas associated with the HEX experiment

1. **Simulations for HEX design optimization**

   Geant4 simulation was used to optimize the design geometry of the HEX ACD system. The ideal design of an anti-coincidence shield requires the primary detector to be surrounded by a secondary detector, which serves to detect and reject those events which contribute to the background in the primary detector. In the case of the HEX experiment, stringent spacecraft weight constraints had to be taken into account during the design of the ACD, which is one of the heaviest subsystems of any γ-ray experiment. Simulations were used to determine the fraction of events that Compton scatter from the primary CZT detector into CsI detectors placed at different positions relative to it. A Geant4 application was developed and used to optimize the geometry of the ACD is elaborated in depth. The results and conclusions of this exercise are presented.

2. **Experimental Characterization of Detectors**

   This work also includes experimental characterization of three different detectors associated with HEX.

   An important aspect of this thesis was to model the veto efficiency of the CsI ACD and to predict the Compton suppression rate of the ACD in the lunar environment. Specific experimental set ups were used to measure the spectrum of Compton scattered photons from a CZT crystal using a commercial CdTe (Cadmium-Telluride) detector. A preliminary step to this measurement was the characterization of the CdTe detector.

   In order to model the response of the CsI ACD, it was necessary to characterize the detector as a function of energy, position, operating voltage and temperature.

The complex spectral characterization of the crystal was modeled taking into account the positional dependence of the spectral parameters. The final results of the experimental test and data analysis of the spectra were used to parameterize the spectral parameters as a function of position on the crystal surface.

The CZT detectors were characterized as a function of energy, position and temperature. Experiments were performed at different temperatures and operating voltages to measure the spectra of the detectors. Measurements at different voltages were necessary to extract the mobility-lifetime products (charge carrier properties) of the electrons and holes of the detector, in order to study the behavior of these parameters as a function of temperature.

3. **Analysis and Modeling of Data**

In this work, data generated from various simulation exercises were validated against experimental data. A comparison of the two data sets was done using goodness-of-fit techniques and hypothesis testing. Spectral quantities of the XR-100T-CdTe detector were used in a Geant4 application to model the response of the detector. The simulated response was then validated against the experimentally measured response, and was subsequently used to simulate the Compton scattered spectrum from a CZT crystal irradiated by ^{133}Ba. These are covered in chapter 2.

The analysis of spectra measured with the CsI ACD and the parameterization of the different spectral quantities as a function of energy and position on the crystal surface is discussed in chapter 3. In this chapter, the response of the ACD is modeled using Geant4 using the parameterized response of the detector and the simulated spectra are compared with the experimentally measured ones. Using this simulated detector response, it was possible to model the veto rate of the ACD, which compared well with the measured rate.

Chapter 4 focuses on the analysis of experimental data measured using one of the nine CZT detectors. Spectral quantities and the mobility-lifetime products of each of the 256 pixels of the crystal were extracted as functions of energy and operating temperature. The spectral quantities were parameterized and included in a Geant4 application designed to simulate the response of the CZT detector. The modeled spectra were then compared with experimental spectra.

The modeled responses of the CZT detector and the CsI ACD were used to simulate the background in the CZT in the lunar environment and the veto efficiency of the ACD in these conditions. This is discussed in chapter 5.

Bibliography

[1a] Lawrence, S.L et al., *Preliminary Results from the Lunar Prospector Alpha Particle Spectrometer*, Lunar and Planetary Science XXXII, 2001

[2a] Lawrence, S.L et al., *Recent outgassing from the lunar surface : The Lunar Prospector Alpha Particle Spectrometer*, Journal of Geophysical Research, Volume 110, Issue E09009, 2005

[3a] Sobol, Ilya, M *A Primer for the Monte Carlo Method*, CRC Press, 1994

[4a] Knoll, G. F *Radiation Detection and Measurement*, Edition 3, John Wiley and Sons, 2000

[5a] Leo, W. R *Techniques for Nuclear and Particle Physics Experiments*, Edition 2, Springer-Verlag New York, 1994

[6a] Tsoulfanidis, N *Measurement and Detection of Radiation*, Taylor and Francis, 1995

[7a] Trombka, J.I et al., *The Cosmic γ-ray Spectrum Between 0.3 and 27 MeV measured on Apollo 15*, Astrophysical Journal, Volume 181, pp 737-746, 1973

[8a] Trombka, J.I et al., *Reanalysis of the Apollo Cosmic Gamma-ray Spectrum in the 0.3 to 10 MeV Energy Region*, Astrophysical Journal, Volume 212, pp 925-935, 1977

[9a] Dean, A.J et al., *Background in Space-borne Low-energy γ-ray Telescopes*, Space Science Reviews, Volume 57, pp 109-186, 1991

[10a] Truscott, P.R et al., *Monte Carlo simulation of induced radioactive background in gamma-ray detector materials*, IEEE Transactions on Nuclear Science, Volume 45, Issue 3, pp 894-902, 1998

[11a] Shaw, S.E et al., *A mass model for estimating the gamma-ray background for the Burst and Transient Source Experiment*, Astronomy and Astrophysics, Volume 398, pp 391-402, 2003

[12a] Tajima, H et al., *Design and Performance of the Soft gamma-ray detector for the NEXT mission*, IEEE Transactions on Nuclear Science, Volume 52, Issue 6, pp 2749-2757, 2005

[13a] Weidenspointner, G et al., *MGGPOD: a Monte Carlo suite for modeling instrumental backgrounds in γ-ray astronomy and its application to Wind/TGRS and INTEGRAL/SPI*, New Astronomy Reviews, Volume 48, pp 227-230, 2004

[14a] Owens, A et al., *A High-Resolution GE Spectrometer for Gamma-Ray Burst Astronomy*, Space Science Reviews, Volume 71, pp 273-296, 1995

[15a] Vedrenne, G et al., *SPI: The spectrometer aboard INTEGRAL*, Astronomy and Astrophysics, Volume 411, pp L63-L70, 2003

[16a] Smith, D.M et al., *The RHESSI spectrometer*, Solar Physics, Volume 210, pp 33-60, 2002

[17a] Weidenspointner, G et al., *MGGPOD:a Monte Carlo Suite for Gamma ray astronomy - Version 1.1*, preprint, astro-ph/0702623v1, 2007

[18a] Agostinelli, S et al., *Geant4: a Simulation Toolkit* Nuclear Instruments and Methods A, Volume 506, pp 250-303, 2003

[19a] Allison, J et al., *Geant4 Developments and Applications* IEEE Transactions on Nuclear Science, Volume 53, Number 1, pp 270-278, 2006

[20a] Nartallo, R et al., *Low angle scattering of protons on the XMM-Newton optics and effects on the on-board CCD detectors*, IEEE Transactions on Nuclear Science, Volume 48, pp 1815-1821, 2001

[21a] Thompson, D.J et al., *Gamma-ray Large-Area Space Telescope (GLAST) balloon flight engineering model: overview*, IEEE Transactions on Nuclear Science, Volume 49, pp 1898-1903, 2002

[22a] Henrique, M et al., *Detailed Calculation of test-mass charging in the LISA mission*, Astroparticle Physics, Volume 22, pp 451-469, 2005

[23a] Ozaki, M et al. , *Framework for a Geant4-Based Simulator of the Radiation Background and Detector Responses of the Space X-ray Observatory Suzaku(Astro-E2)*, IEEE Transactions on Nuclear Science, Volume 53, pp 1310-1316, 2006

[24a] Ersmark, T et al., *Status of the DESIRE Project: Geant4 Physics validation Studies and First Results From Columbus/ISS Radiation Simulations*, IEEE Transactions on Nuclear Science, Volume 51, pp 1378-1384, 2004

Chapter 2

Geant4 and Experimental Validation of Simulation

This chapter briefly discusses the Geant4 simulation toolkit. Validation of simulation with experimentally measured and published results, with respect to the HEX experiment, forms the core of this chapter

2.1 Features of the Geant4 Simulation toolkit

Geant4 [18a],[19a] is a toolkit developed by a large team at CERN and other laboratories across the world. It permits the study of interaction of particles in a user-defined detector system. The user defines the types of interaction processes that will be simulated for a given trial. As the particle interacts at various subsections of the detector geometry, the user can extract numerous details. If a specific detector volume is defined as "sensitive" under Geant4, the track information (location, type of interaction, energy loss etc) can be derived at finer spatial samples. The particle is followed or "tracked" within the program until its energy drops becomes zero.

As mentioned in section 1.3.3, Geant4 follows an object oriented design and is hence composed of logical units called "class categories". A class category consists of classes that have a close relationship; there are eight such logical units in Geant4, which are discussed briefly below.

1. **The Geometry Class Category**
   This class category allows the definition of detector geometry. Detector properties are represented in a hierarchical "tree" structure. The shape and dimensions of the

detector are represented by the **solid volume** class. The **logical volume** class contains the object of the solid volume and additional attributes such as material information, sensitivity of the volume to particle interaction and visualization. Its object is contained by the **physical volume** class which includes information on the placement and orientation of the geometry in three dimensional space.

2. **The Material and Particle Class Category**
   Materials in Geant4 can be defined as isotopes, elements or materials (compounds or mixtures). Elements can be made up from isotopes and materials are made up from elements. The user must make sure to supply correct input parameters like density of the material and fraction of weight of its constituting elements.
   Geant4 is a multi-particle simulation toolkit, treating gluons/quarks, leptons, mesons, baryons, ions, optical photons and high energy photons. Particles are defined by three classes that define separately the

   - name, mass, spin, lifetime and decay modes of the particle.
   - dynamics of the particle necessary for its interaction with matter, like energy, momentum, polarization etc and includes the static information described previously.
   - position, time and step information of the particle.

3. **The Tracking Class Category**
   This category consists of three classes. The *G4Step* class represents a step through which a particle is propagated in the simulation. The object of this class stores transient information of the step and this information is updated each time a physics process is invoked. After the step is completed, information can be extracted from it. The *G4StepPoint* class represents the end-points of the step and contains information about the geometry, material, physics processes etc. The *G4Track* class contains information on the status of the particle after a step is completed. The *G4Step* class contains a pointer to the object of *G4Track*.

4. **The Hits and Digitization Class Category**
   A detector is said to be *sensitive* when information about the particle track can be extracted from it once the track crosses into the *sensitive* volume. There exists a sensitive detector base class, from which the user must create a concrete class. When the object of the logical volume of a detector is made to point to this user defined sensitive detector class, the detector in question is said to become *sensitive*. In the user defined concrete sensitive detector class, the object of the *G4Step* class can be used to retrieve information about the particle track, which can be the energy deposited in the step, the physics process that resulted in the

energy deposition, the name or other identifying parameter of the volume that the track is in, etc. This information is used to create *hits*. A hit represents particle interaction in a detector. A *digit* is used to represent the detector physics output.

5. **The Physics Class Category**

   The implementation of physics in Geant4 is transparent and consists of processes and models. A process is defined as a class which describes how and when a specific kind of physical interaction takes place. A given particle has several processes assigned to it. A model is a class which has methods or procedures to implement the details of a physical interaction. One or more models can be assigned to a process. Models can be selected based on the energy range, material etc.

   The user has to define all the required physics processes in a class called *G4UserPhysicsList*, which is derived from a physics list base class. In the concrete class, the user has to construct particles, processes and set "cuts" for the production of secondary particles. Cuts are defined as the lowest energy threshold below which no secondary particles are created. The physics processes available in Geant4 are Electromagnetic, Hadronic, Decay, Optical photons, and Transportation.

6. **The Run and Event Class Category**

   The "run" is the largest unit of the simulation and consists of the number of events to be simulated. It is represented by the *G4Run* class and is controlled by the *G4RunManager* class. Classes for detector construction, physics and primary particle generation must be registered to the *G4RunManager* class.

   An object of the *G4Event* class is an "event" and is the primary unit of the simulation. The input of an event is the source particle and its positional information. After an event is completed, it contains information about hits and trajectories, which can be extracted by the user for later processing.

7. **The Visualization Class Category**

   This class category manages the visualization of solids, trajectories and hits.

8. **The Interface Category**

   This class category handles interaction of the simulation application with external software for the production of graphical user interfaces (GUIs).

Further details on the Geant4 toolkit and class structure can be obtained from [18a], [19a], [1b], [2b].

2.1.1 The General Source Particle Module

Geant4 was initially developed for ground-based high energy physics; the sources described were usually unidirectional and mono-energetic. Users working in other fields, such as space science needed to hard code source geometries that they needed for a particular application; such as spatially extended sources (sometimes enclosing detectors), random positions and ejection angles of the primary particles and generation of energy spectra. The General Source Particle Module (GSPM) was developed for space science applications, intended for use with Geant4. Once linked and compiled it can be used to generate source particles without the need for C++ coding. The GSPM software enables users to specify energy spectra, positional and angular distribution of the source particles, via command line or macro batch files.

All particles can be specified by GSPM, including nuclei to simulate radioactive decay. Cartesian co-ordinates can be specified to indicate the (x,y,z) position from which the source particles are emitted. The positional distribution of sources can be point, surface or volume, with a variety of shapes to choose from. The angular distribution of the particles can be either isotropic or have a cosine distribution, and the user can define their own distribution by specifying θ and ϕ. In the case of cosine distribution, the opening angle of the source can also be specified. The energy of the incident particle can be either mono-energetic or distributed in a spectrum. In the case of a spectrum, the user has a number of pre-defined functions to choose from : linear, logarithmic, exponential, power law, bremsstrahlung, black body or even user-defined functions. This is done by entering the differential distribution as a histogram or as a list of spectral points. There are a variety of interpolation schemes available as well - linear, logarithmic, exponential, etc.

GSPM is a part of the Geant4 toolkit, and its classes are installed along with the rest of the Geant4 kernel. This has been extensively used in the work contained in this thesis. More information on GSPM can be found in [3b]

2.2 Why is simulation validation important?

Simulations are carried out to predict the outcome of an experiment or in regions of the parameter space which are hard to cover experimentally. In addition, realistic simulations build confidence in a design before initiating hardware fabrication. The usefulness of a simulation exercise depends on the confidence in the input parameters and procedures. Reproduction of experimental results through simulation might require several iterations with different input parameters. A good match with experimental results would imply that the input parameters chosen for the simulation are close to the real world values. Any discrepancies that occur in the course of the simulation can be attributed to improper definitions of input parameters (geometry modeling, source definition, physics implementation etc) or in the procedure or even in not having complete understanding of the system response. These discrepancies can then be systematically eliminated as much as possible by fine tuning input parameters, so that the experimental results can be modeled to a high degree of accuracy.

In this present study, Geant4 has been used to optimize the design of the CsI ACD and to model the spectral redistribution functions of the CZT and CsI detectors of the HEX experiment. The optimized design of the ACD was incorporated into the hardware design of the experiment. The spectral responses are used to simulate the background in the CZT detector and the veto count rate of the ACD in lunar environment. As a preliminary step however, it is necessary to perform a series of exercises wherein certain aspects of the simulation are validated against laboratory or published data.

The design optimization of the CsI ACD depends upon accurate simulation of Compton scattered photons from the CZT detector, since its main purpose is Compton suppression of the CZT spectrum. Before this optimization is performed, it is essential to validate the simulated Compton scattered spectrum from CZT against the experimentally measured spectrum. A laboratory experiment was designed especially for this purpose.

In order to model the spectral redistribution function of the two detectors it is required to use input parameters extracted from characterization of the detectors in the laboratory. This characterization is usually conducted using a limited number of x/γ-rays available for measurement purposes. However, in order to correctly predict the response of the detectors to other photon energies in the energy range of interest, one must validate these modeled responses against available experimental data.

Modeling the CZT detector background in the lunar environment requires validation of the particle source simulation and the physics of interaction of heavy charged particles and neutrons in matter. Geant4 exercises were preformed to simulate output spectra that were validated against published observed data and theoretical formulas.

Sections 2.4 through 2.7 will demonstrate validation of the preliminary steps required for the main Geant4 simulation.

The next section discusses a few features of quantitative statistical analysis and its application in the validation exercises.

2.3 Statistical Analysis

According to [5b], "*Statistics is concerned with the scientific method for collecting, organizing, summarizing, presenting and analyzing data, as well as drawing valid conclusions and making reasonable decisions on the basis of such analysis.*"

Statistics is the study of deriving meaningful information from data. Inferential statistics is a subdivision of statistics, which uses quantitative techniques to make approximate generalizations from limited observations. These methods are used to test the significance of various assumptions and to develop models that best define data.

2.3.1 Hypothesis testing

A hypothesis is defined as a statement that needs to be verified. A **null hypothesis**, represented by H_0, is a statement that is assumed to be true, which needs to be verified. To illustrate, in this chapter the simulated data is to be validated against experimental data. This is the problem that needs to be solved. The null hypothesis then states that the simulated and experimentally measured data are the same. If the null hypothesis turns out to be wrong, it is rejected in favor of the **alternative hypothesis**, H_a, which simply states that the null hypothesis is false.

During hypothesis testing, there is a chance of rejecting the null hypothesis, when it is actually true. The risk of committing this error is called the level of significance of the test, or α. Conventionally, a risk of 5% is chosen as the significance level. This means that the null hypothesis can be accepted with 95% confidence. The smaller the significance level, the higher the confidence in the truth of the null hypothesis.

Once the hypothesis has been defined, next one must choose a statistical technique as a goodness-of-fit test criterion, which was the χ^2 test for the work presented in this chapter. The χ^2 goodness-of-fit test is discussed in the next section.

For the validation exercises discussed in this chapter, the hypothesis test is outlined in table 2.1.

H_0	the simulated data and experimentally measured/observed data are similar
H_a	the simulated data and experimentally measured/observed data are not the same
statistical test	χ^2 test
α	5%

TABLE 2.1: Definition of the hypothesis test

2.3.2 Goodness-of-Fit Tests and Residuals

Simulation of the quantities discussed in section 2.2 involves modeling observable physical quantities. The goodness-of-fit describes how well a model fits an observed data set. Quantitatively, it defines the discrepancy between the observed and expected values. The test statistic used to quantify this discrepancy depends on the problem being considered. With regard to the work presented in this thesis, the reduced χ^2 goodness-of-fit test was used.

The χ^2 value is defined as the sum of the squares of the differences between the observed and expected values squared, weighted by the errors on the measurement. In the case of observed and expected distributions f(x) and g(x)

$$\chi^2 = \sum_{i=1}^{n} \left(\frac{(f(x_i) - g(x_i))^2}{\sigma(f(x_i))^2} \right) \tag{2.1}$$

where ‘n’ is the number of bins, f(x_i) and g(x_i) are the values of the observed and expected distributions for the i^{th} bin respectively, and $\sigma(f(x_i))$ is the error on f(x_i).

In the case when errors are available for both the distributions,

$$\chi^2 = \sum_{i=1}^{n} \left(\frac{(f(x_i) - g(x_i))^2}{\sigma(f(x_i))^2 + \sigma(g(x_i))^2} \right) \tag{2.2}$$

where $\sigma(g(x_i))$ is the error on g(x_i). In the case of counting experiments,

$$\begin{aligned} \sigma(f(x_i)) &= \sqrt{f(x_i)} \\ \sigma(g(x_i)) &= \sqrt{g(x_i)} \end{aligned}$$

Therefore substituting in eqn(2.2),

$$\chi^2 = \sum_{i=1}^{n} \left(\frac{(f(x_i) - g(x_i))^2}{f(x_i) + g(x_i)} \right) \tag{2.3}$$

The reduced χ^2, χ^2_ν is computed by dividing the χ^2 by the number of degrees of freedom, ν.

Table C.4 from [7b] gives tabulated values of χ^2_ν corresponding to a particular value of of the significance level, α for different values of ν. The tabled values of χ^2_ν correspond to an upper one sided test; this means that if the computed value of the χ^2_ν for a particular value of α and ν is greater than or equal to the corresponding tabled value, the null hypothesis is rejected. If the computed χ^2_ν is less than the tabled value, then it means that there is not enough evidence to reject the null hypothesis.

Residuals are defined as the difference between a model and the observed values. They give a qualitative description of any discrepancy between the two.

The next sections deal with validation of different aspects of simulations using Geant4 against experimental data either measured in the laboratory by the author or from published results. The statistical method described above has been used for hypothesis testing of simulated data and experimental data.

2.4 Validation of Compton Scattering from CZT crystal

The main function of the HEX ACD is to detect Compton scattered photons from the CZT crystal. The validation exercise discussed in this section aims to test the reproducibility of experimentally measured Compton scattered spectrum from CZT; i.e. to answer the question: when simulating the ACD and CZT in Compton suppression mode, is the ACD really detecting Compton scattered photons from the CZT crystal.

In the laboratory, a commercial CdTe detector was used to measure the Compton scattered spectrum from the CZT crystal. This detector was used because of its ease of operation and low noise characteristics. Since the Compton scattered photons from the CZT crystal were detected using the CdTe detector, one must first model its response before one can accurately simulate the measured spectrum. In other words, before one can attempt to simulate the spectrum of Compton scattered photons as detected by the CdTe detector, one should incorporate its spectral redistribution function into the simulation model.

In the following sections the experimental characterization of the commercial CdTe detector from AMPTEK, modeling its response with Geant4, and validation of this response against experimental measurements are discussed.

2.4.1 About the CdTe detector

XR-100T-CdTe is an x-ray/γ-ray detector with a preamplifier and a thermoelectric cooler (TEC), manufactured by AMPTEK. The detector is a CdTe (Cadmium Telluride) diode (3 mm × 3 mm × 1 mm) mounted on the TEC. The input FET stage and the feedback components of the A205 preamplifier are also mounted on the cooler. The internal temperature is maintained at -30°C. An operating potential of 500 V is required for complete electron/hole collection, and cooling the detector results in reduction of leakage current and electronics noise. The experimental setup is depicted by the block diagram in fig(2.1). The detector is mounted 0.3 cm behind a 250 μ thick

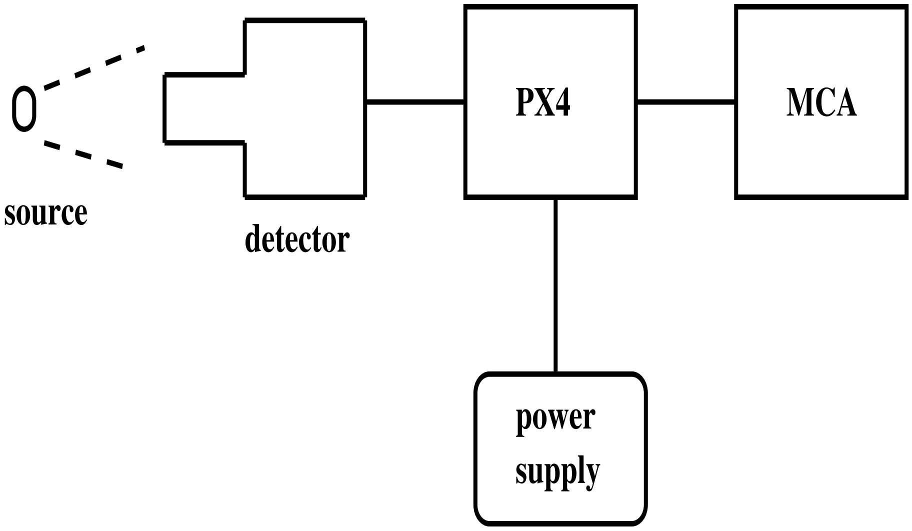

FIGURE 2.1: Experimental set-up to measure the XR-100T-CdTe detector response.

Beryllium window. The system also includes the complete signal processing chain data acquisition and analysis software. The XR-100T-CdTe preamplifier output is the input to the SA system, indicated in the block diagram as PX4, to which the power supply is also connected. It also consists of a MCA which bins the counts into a spectrum.

2.4.2 Characterization of the XR-100T-CdTe

Spectra from ^{133}Ba and ^{241}Am were measured using the XR-100T-CdTe, with amplifier gain and peaking time of the pulse shaper set to optimum values. These values were optimized with respect to the maximum energy range that can be measured with the system and the lowest electronic noise (hence, best energy resolution). These optimized values are listed in the table 2.2. The characterization of XR-100T-CdTe is summarized in the plots shown in fig(2.2). The energy-channel conversion equation was obtained by

Parameter	Optimized value
Amplifier gain	4.13
Peaking time	11.2 μsecs
Highest MCA channel	2047
Highest energy	285 keV
Energy resolution	1% at 59.5 keV

TABLE 2.2: Optimized instrumental parameters of the XR-100T-CdTe detector

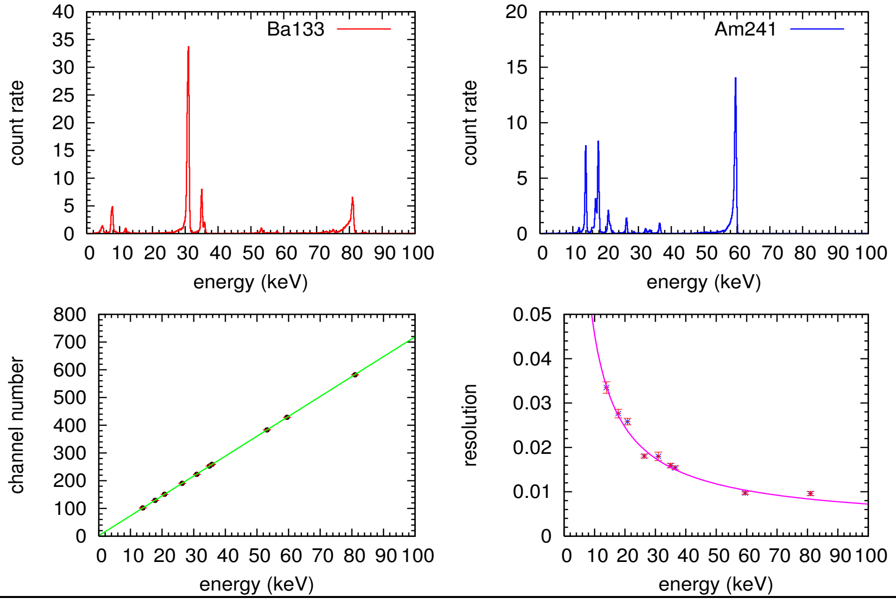

FIGURE 2.2: Summary of XR-100T-CdTe characterization : **Top left** - ^{133}Ba spectrum in energy space; **Top right** - ^{241}Am spectrum in energy space; **Bottom left** - Energy-channel conversion; **Bottom right** - Resolution versus energy relation

fitting channel versus energy data with a straight line as shown in the bottom left plot of fig(2.2).

$$\mathrm{Ch} = \mathrm{offset} + \mathrm{gain}E \tag{2.4}$$

where Ch is the channel number, offset is 1.77 channels, gain is 7.17 channels/keV and E is the incident energy. Using this equation, the peaks in the spectra were fit to obtain values of the spectral width parameter, σ, for each peak in energy units. The resolution was then calculated and plotted versus energy and fit with equation

$$R = \frac{2.35}{E}\sqrt{FEw + w^2N^2} \tag{2.5}$$

where R is the resolution, E is the incident energy, w is the amount of energy needed to produce one electron-hole pair (0.00443 keV), F is the Fano Factor and N is the equivalent noise charge (ENC) in units of number of electrons; F and N are the free parameters in this relation. The fit gives values of 0.143 and 40 electrons for F and N. This is shown in the bottom right plot of fig(2.2).

The only experimental parameters that could not be extracted (due to technical constraints) from the characterization of this detector were the charge transport properties of electrons and holes for the CdTe material. These parameters, the **mobility-lifetime**

products of electrons and holes, $(\mu\tau)_{e,h}$ were therefore based on the general values reported for CdTe detectors (AMPTEK data sheet) which were $(\mu\tau)_e \sim 3.8\times10^{-3}$ cm^{2}V^{-1} and $(\mu\tau)_h \sim 2\times10^{-4}$cm^{2}V^{-1}. The transport properties of the electron defines the location of the photopeak, and the hole transport properties determine the fraction of events that make up the photopeak. The importance of these parameters and the method of extracting them is elaborated in detail in chapter 4.

2.4.3 Geant4 Application Design and Results

Using the spectral parameters derived from the XR-100T-CdTe characterization, the spectral response of the detector was simulated using Geant4. The fig(2.1) shows the schematic of the experimental set up, which was modeled as described below.

The XR-100T-CdTe detector was modeled as 1 mm thick, with an area of 9 mm^2, with a 0.1 mm thick Beryllium window placed at a distance of 2.5 mm in front of it. The window and detector are housed in an annular stainless steel cylinder 3 mm high, with outer and inner diameters of 15 mm and 8 mm respectively. The detector was made *sensitive* by setting the pointer of its sensitive detector class to its logical volume. The energy deposited in the detector is obtained by extracting the *hits* information in the *UserEventAction* class using the object of the *G4HCofThisEvent* class. The input parameters used in the *UserEventAction* class to model the detector response were relations between channel and energy, resolution and energy, and the $(\mu\tau)_{e,h}$ products.

The source was modeled using GSPM, as a plane circle of diameter 7 mm placed in a plastic disc of thickness 3 mm and diameter 25 mm. The simulation was run for 10^6 events with photons of energy 122.1 keV which was used in the experiment.

The physics processes included in the Geant4 simulation are listed in the table 2.3.

Physics process	Geant4 class
Low energy photoelectric effect	G4LowEnergyPhotoElectric
Low energy Compton scattering	G4LowEnergyCompton
Low energy pair-production	G4LowEnergyGammaConversion
Low energy Rayleigh scattering	G4LowEnergyRayleigh
Low energy ionization	G4LowEnergyIonisation
Low energy bremsstrahlung	G4LowEnergyBremsstrahlung
Positron annihilation	G4eplusAnnihilation
Radioactivity	G4RadioactiveDecay
Multiple scattering	G4MultipleScattering
Transportation	G4Transportation

Table 2.3: List of physics processes used.

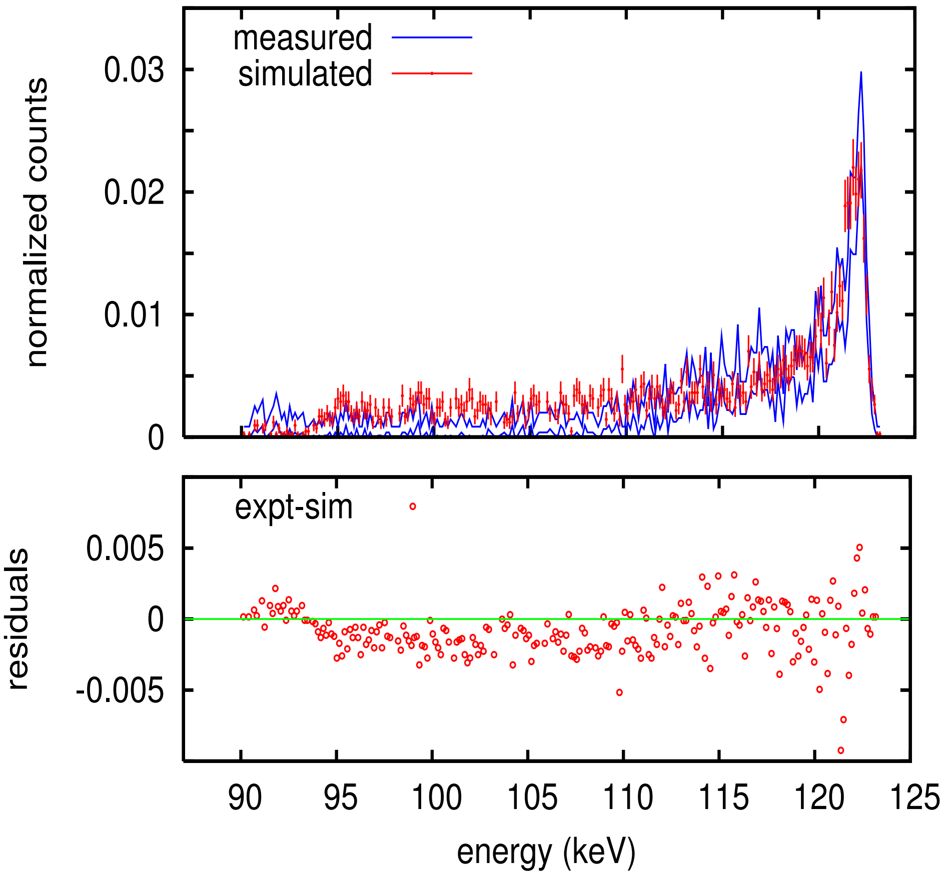

FIGURE 2.3: **Top Panel**: Comparison between the simulated XR-100T-CdTe detector response with measurement. The experimental data are represented in this plot by the $\pm 1\sigma$ error band, shown by the blue lines. The closed circles are the simulated data with 1σ errors shown by the vertical red bars; **Bottom Panel**: Residual plot. The open circles represent the difference between the experimental and simulated data and the solid line at y=0 is for reference.

The plot in the top panel of fig(2.3) shows the comparison between the simulated and measured XR-100T-CdTe detector response, plotted as normalized counts (counts in each bin divided by total counts under the spectrum) versus energy, from 90 keV to 125 keV. The blue lines are the $\pm 1\sigma$ error bands of the experimental data and closed circles are the simulated data, with the 1σ errors shown as bars for each data point. The experimental data are not shown to avoid crowding of the plot. The plot in the bottom panel of the figure is the residual plot, where the open circles represent the difference between the measured and simulated data. The solid line at y=0 in the residual plot is a reference mark. As can be seen from the figure, all the simulated data points are contained within the error bands of the experimental data, except in the region between 95 keV and 110 keV.

In the region from 95 keV to 110 keV, it is clear that the simulated spectrum overestimates the continuum with respect to the measured data. This is shown in the residual plot in the fig(2.3) by the negative region.

This overestimation in the continuum is reciprocated by a drop in the peak amplitude, as can be seen in both plots of fig(2.3) at 122.1 keV. This could be due to an underestimation of the mobility-lifetime product for the holes. The smaller the value of the hole mobility-lifetime value, the more probable it is for these charge carriers to be trapped in crystal defects. This hole trapping leads to incomplete contribution of the hole mobility to the total charge collected at the electrodes, and hence an increase in the phenomenon of"hole tailing". Details of this phenomenon and the effects of the charge carrier mobility-lifetime products on spectral shape are discussed in chapter 4.

The fact that the simulation reproduces the experimental response over the remaining energy range helps in concluding that this response can now be employed in the next step of the exercise, which is to simulate the Compton scattered spectrum from the CZT crystal, as measured by the CdTe detector.

In order to reproduce the Compton scattered photons from the CZT crystal, an experiment was performed in the laboratory.

The experimental set up consisted of a ^{133}Ba radioactive source in its plastic disc holder, pasted onto a bare CZT crystal (40mm×40mm×5mm), without its associated ASIC and PCB, and the source-crystal arrangement was placed at a distance of 7 mm from the Beryllium window of the XR-100T-CdTe detector system. The experimental set-up as modeled by Geant4 is illustrated in the fig(2.4).

The Compton scattered spectrum of the ^{133}Ba photons up to 285 keV, were measured by the XR-100T-CdTe detector, and recorded. The integration time that was needed to record a spectrum not dominated by counting statistics was nine hours. The solid line in fig(2.5) is the measured Compton continuum of of ^{133}Ba, normalized with respect to the total counts under the spectrum.

What is of interest to this experiment is the Compton scattered continuum. This continuum is due to the Compton scattering of certain γ-ray lines of the ^{133}Ba radioactive source in the CZT. The most important lines are provided in the table 2.4 in order of decreasing relative intensity. Since the maximum energy range of the CdTe detector is 285 keV, the lines with energy greater than 285 keV are not seen. The nine hours of integration time needed to achieve meaningful counting statistics were still not sufficient enough to detect the 160.6 keV and 223 keV lines, as they are too weak.

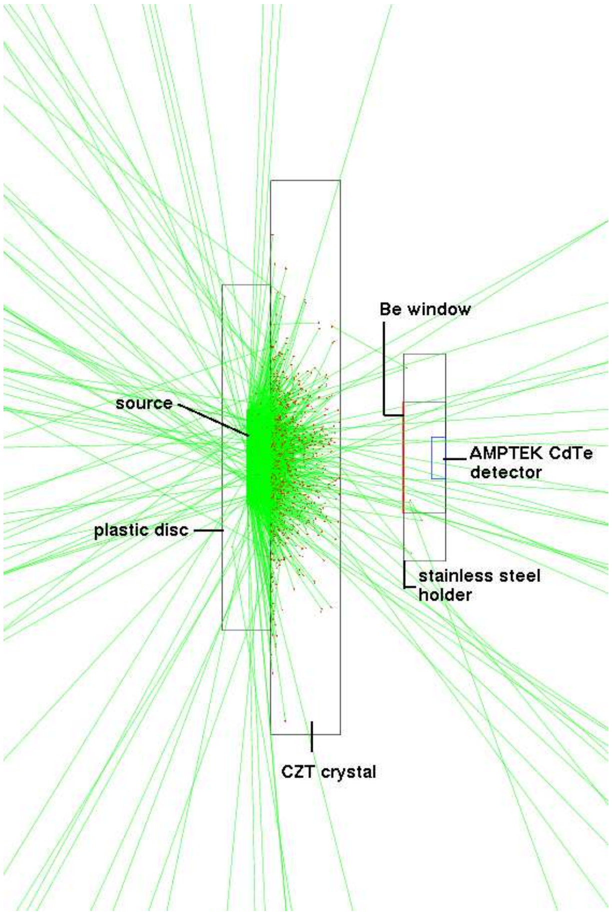

FIGURE 2.4: Experimental set up of the Compton scattering experiment as modeled with Geant4

γ-ray energy (keV)	Relative intensity
356	1
303	0.32
383	0.14
276	0.13
160.6	0.013
223	0.011

TABLE 2.4: List of ^{133}Ba γ-ray lines

The physics processes included in the simulation is listed in the table 2.3. The low energy peaks like 30.97 keV and 81 keV were not included in the simulation exercise. The top panel of fig(2.5) shows the simulated spectrum represented by closed circles compared with the measured spectrum. The simulated spectrum was derived as the sum of the series of the γ-ray lines listed in table 2.4 which make up the high energy part of the ^{133}Ba spectrum. The plot in bottom panel of fig(2.5) is the residual plot, where the circles represent the difference between the experimental and simulated data. The errors on the data of the two distributions are not shown in the plot to avoid crowding. As can be seen, the residuals are randomly distributed about the reference line at y=0 (represented by the green solid line the residual plot) throughout the energy range, except in the vicinity of the 276 keV line. The residuals indicate an excess of counts in the low energy tail of the simulated spectral line, which is probably due to underestimation of $(\mu\tau)_h$ as discussed in earlier.

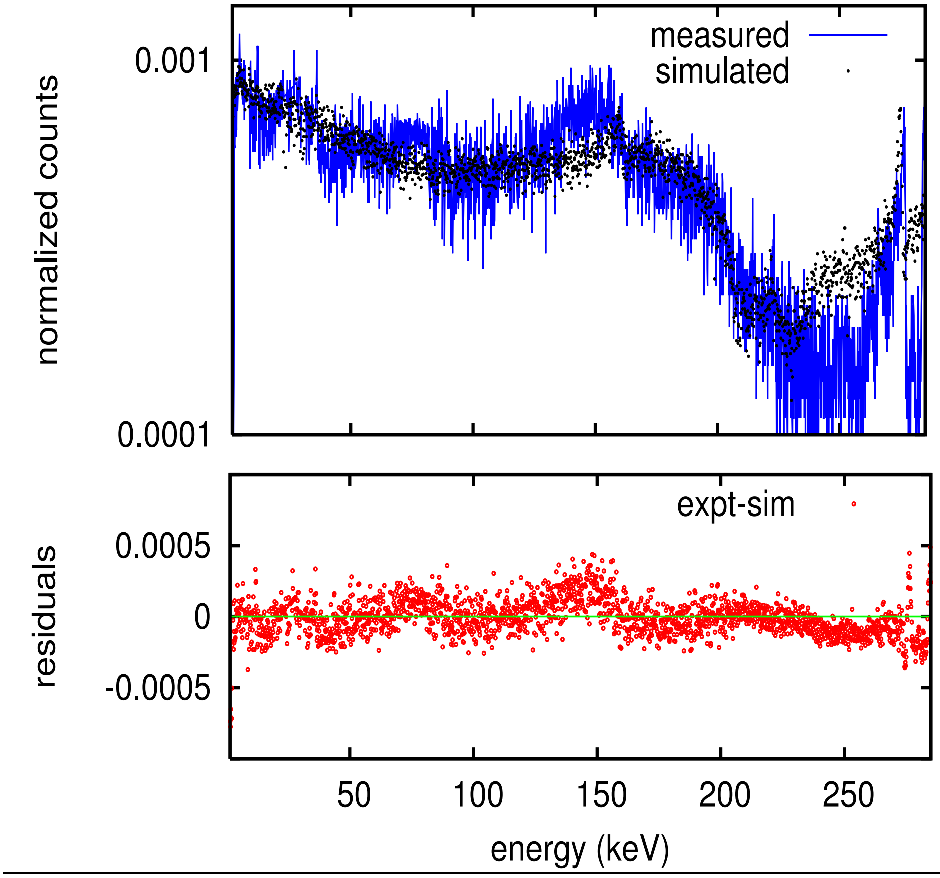

FIGURE 2.5: **Top Panel**: Comparison between the simulated and measured Compton scattered spectrum, represented by closed circles and solid blue lines, respectively; **Bottom Panel**: Residuals of the above plot; the closed circles represent the difference between measured and simulated data, while the green solid line at y=0 is for reference.

This validation gives confidence in the simulation methodology with respect to reproducing an experimental set up as well as in the spectrum of Compton scattered photons from the CZT material.

2.5 Validation of source generated by GSPM

All the sources as described in this thesis are generated using GSPM. As a routine check of the whole simulation exercise, it is important to determine whether GSPM actually generates assumed input spectrum.

In GSPM, it is possible to express the input spectra in terms of pre-defined distributions, like a simple power law or a user-defined spectrum represented by a histogram with the values of energy and flux. If a detector is illuminated by source particles defined by a particular source geometry, it should be possible to reproduce the incident spectrum, after normalization.

Consider an isotropic source with flux F(E) particles cm^{-2} s^{-1} keV^{-1} sr^{-1} incident on a detector of area A cm^2 placed at a distance R from the source. The exposure time of the detector to the source is T seconds. In the simulation environment, the known parameters that can be controlled by the user are :

- the spectral shape and the number of incident particles, N_0.
- the spatial extent of the source, and its position with respect to the detector.
- the angular distribution of the source, i.e. whether the particles are isotropic with respect to the detector or have a cosine distribution.
- the area A of the detector in cm^2.

The exposure time T can be computed by counting the number of particles detected by the detector. If N denotes the number of particles counted by a detector of area A placed at a distance R, then

$$\begin{aligned} N &= A\,T \int_{E_1}^{E_2} \int_{4\pi} \frac{F(E)}{cm^2\ s\ sr\ dE}\, dE\, d\Omega \\ &= A\,T \int_{4\pi} \frac{I(E)}{cm^2\ s\ sr}\, d\Omega \\ &= A\,T \frac{I'(E)}{cm^2\ s} \end{aligned} \tag{2.6}$$

where $I(E)$ is the integral flux, $I'(E)$ is the integral flux averaged over the entire solid angle. From eqn(2.6),

$$T = \frac{N}{A\,I'(E)} \tag{2.7}$$

The simplest way to validate the source generated by GSPM is to place a vacuum filled particle counter at the centre of a sphere, the inner surface of which acts as an isotropic particle generator. For example, consider the Cosmic Diffuse X-ray Background (CDXB) [9a] which forms a background against which x-ray measurements have to be made; it is expressed by eqn(2.8). It is a simple power law, valid between 20 keV and 1 MeV, and can be expressed in GSPM by giving the type of its energy spectrum , minimum and maximum energies, and power law index.

$$dN(E) = 87.4E^{-2.3}dE \quad \text{photons cm}^{-2}\text{s}^{-1}\text{keV}^{-1}\text{sr}^{-1} \tag{2.8}$$

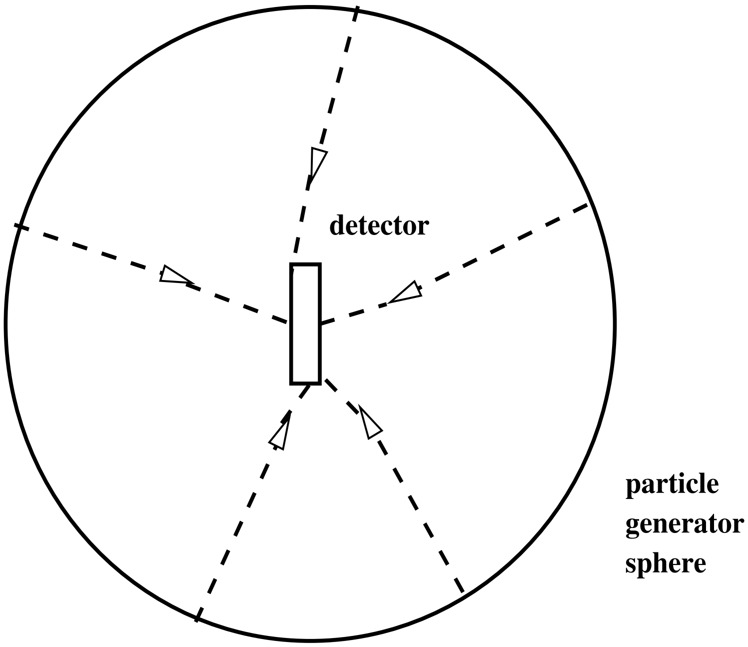

Figure 2.6: Test geometry for the validation of spectra generated by GSPM. The particles are generated isotropically from the inner surface of the sphere. The detector is placed at the centre of the sphere. The dashed lines represent the particles generated from the sphere with the arrows indicating direction of incidence of the particles.

2.5.1 Geant4 Application Design

The detector is modeled as a simple counter of 144 cm^2, arbitrarily chosen to be similar to the geometrical area of the HEX CZT detector. It is filled with vacuum to eliminate the need to convolve the response of the detector material to extract the source photons. The source is defined by a sphere with particles generated isotropically from its surface with the detector placed at its centre. The radius of the sphere determines the distance of the source from the detector. The test geometry is illustrated by the schematic diagram in fig(2.6).

The spectral shape is defined as a power law, and the minimum and maximum energies are given as 20 keV and 1000 keV and the power law index is entered as -2.3, consistent with eqn(2.8). The integral flux $I(E)$ for the CDXB spectrum between 20 keV and 1 MeV has been calculated as 1.36 photons $\text{cm}^{-2}\text{s}^{-1}\text{sr}^{-1}$. In order to average over all solid angles, this is multiplied by 4π to get $I'(E)$ as 17.09 photons $\text{cm}^{-2}\text{s}^{-1}$. The number of incident photons for the simulation is 10^8. The aim of this exercise is to prove that irrespective of the radius of the generator sphere or the area of the detector, the particle spectrum generated by GSPM matches the input spectrum.

At the start of the exercise, it had been assumed that the simulated spectrum has no dependence on R or A. The simulation was therefore been performed for three cases

1. Case 1 : A = 144 cm^2, R = 1500 mm
2. Case 2 : A = 144 cm^2, R = 2500 mm
3. Case 3 : A = 288 cm^2, R = 1500 mm

In each case the number of photons counted by the detector was noted. In order to compare the simulated spectrum with the input spectrum, the number of photons counted in each case should be normalized or standardized to units of photons $\text{cm}^{-2}\text{s}^{-1}\text{keV}^{-1}\text{sr}^{-1}$. Therefore, the exposure time T for each case was calculated by substituting I'(E), R and A in eqn(2.7) and listed as:

- Case 1 : T = 64.73 seconds
- Case 2 : T = 8.76 seconds
- Case 3 : T = 35.62 seconds

2.5.2 Results

The normalized simulated spectra for each of case are represented by closed circles in fig(2.7) and are compared with the theoretical spectrum as calculated from eqn(2.8), which is represented by solid lines. Errors on the simulated values are computed taking into account counting statistics; the counts in each energy bin follows Poisson counting statistics and therefore, the error on the count is the square root of the count. The errors are not shown in the figures to avoid crowding. As can be seen from the plots, the CDXB input spectra matches perfectly with the simulated spectra.

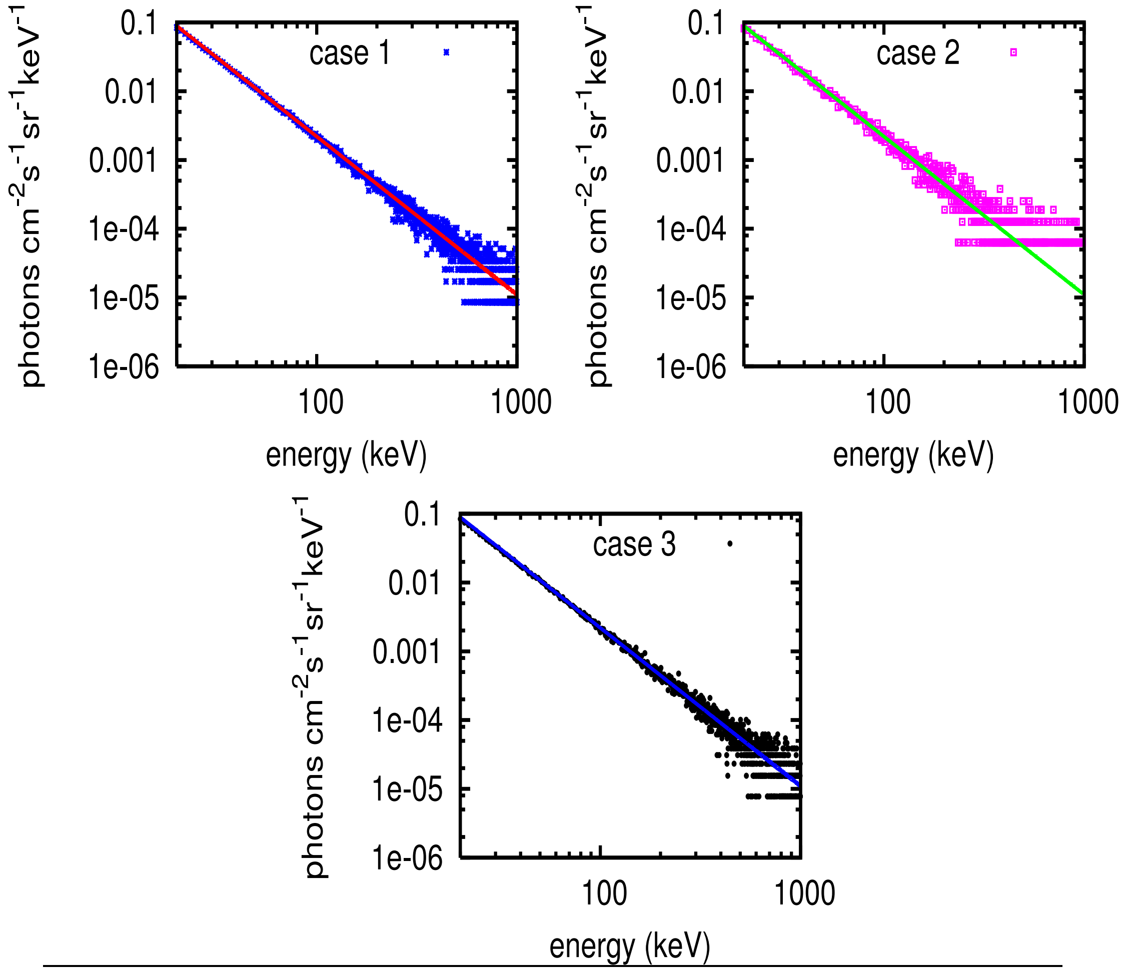

FIGURE 2.7: Results from the simulation of the CDXB ; **Top Left** Case 1; **Top Right** Case 2; **Bottom Centre** Case 3. The input spectrum according to eqn(2.8) is shown in each plot by the solid lines, and the simulated data are represented by points.

To quantitatively indicate the correctness of the simulated spectra, the simulated spectra in each case have been fit with the input spectrum and the goodness-of-the fit determined by the χ^2_ν test according to eqn(2.1). For each case, ν waa 50. The values of χ^2_ν are tabulated in table(2.5). From table C.4 of [7b], the tabulated value of χ^2_ν for α equal to 0.05 or 5% and ν corresponding to 50 is 1.350. For each case, the computed χ^2_ν is less than 1.350, which means that there is not enough evidence to reject the null hypothesis, which states that the model and the simulated data are similar. Therefore, the difference between the input spectrum given by eqn(2.8) and the simulated data in each case is not significant at the 5% level and one can say that the two data sets are similar at the 5% level.

Case	χ^2_ν
Case 1	0.629
Case 2	0.367
Case 3	0.956

TABLE 2.5: χ^2_ν values of the χ^2 goodness-of-fit test for validation of simulated CDXB spectrum against the input CDXB spectrum

The physical significance of these results may therefore be stated as follows:

1. The spherical source geometry is not biased towards any arbitrary θ and ϕ.
2. The procedure adopted for deriving the exposure time, given the number of incident particles and the source-detector geometry is capable of producing results that show a good match with quoted values, both qualitatively as well as quantitatively.

2.6 Validation of Hadronic physics

One of the sources of the background in the HEX CZT detector in orbit is due to the interaction of Galactic Cosmic Rays (GCR) and solar energetic particles with the detector and its immediate surroundings. The interaction of high energy particles with all this material generates a shower of secondary particles - photons, mesons, neutrons - which decay/interact subsequently to generate a flux of additional photons and electrons. Using the extensive hadronic physics list of Geant4, one can simulate these showers and estimate the background seen by the detector when it is housed in its actual spacecraft environment.

The HEX CZT detector is a hard x-ray/soft γ-ray detector and hence it is essential to validate the γ-ray spectrum that the hadron specific physics can produce for a particular source and detector geometry configuration; this will help one to understand the various physical processes that take place to generate secondary γ-rays from cosmic ray particles.The source geometry for space based applications has already been validated in section 2.5.

The hadronic processes which will also be used for the HEX CZT background simulation are listed below

Elastic scattering for all particles - p, $\overline{p}$, n, $\overline{n}$, π^+, π^-, neutral and charged kaons, deuteron, triton, α, and all strange particles
Low Energy Parameterized Models from 1 to 25 GeV for inelastic scattering for all particles
High Energy Parameterized Models from 25 GeV to 10 TeV for inelastic scattering for all particles
Processes for absorption of π^-, K^-, $\overline{p}$, and $\overline{n}$ at rest
Models to simulate break-up of nuclei, like evaporation, pre-compound model, Fermi break-up etc, and CHIPS based models
Models to simulate intra-nuclear cascades
Photonuclear and Electronuclear processes

Table 2.6: List of hadronic physics processes.

In addition to the hadronic physics, electromagnetic interactions as listed in table 2.3 were also included.

2.6.1 Geant4 Application Design

Figure(2.8) shows the spectra of GCR protons for minimum, average and maximum solar activity, calculated using the eqn(2.9) from [8b]

$$J(E,M) = 1.244 \times 10^6 \frac{E(E+1876)(E+M+X)^{-2.65}}{(E+M)(E+1876+M)} \tag{2.9}$$

where,

J(E,M) is the proton flux in units of protons cm^{-2}s^{-1}MeV^{-1} as a function of E and M; E is the kinetic energy of the proton; X = $780e^{-2.5\times10^{-4}E}$; M is the **solar modulation parameter** in units of MeV, and is the parameter that defines the solar influence on the cosmic ray flux.

Hadronic physics validation was performed using observational results of locally produced γ-ray background detected by the Apollo 15 NaI(Tl) scintillation detector. The spectrum was measured during the Trans-Earth Coast of April 1971 [7a] while the detector was inside the spacecraft and not deployed. During this time the solar activity was between solar minimum and maximum. The simulation application was designed as follows

- Information for approximating the spacecraft and detector geometry was obtained from [9a]. For the Apollo 15 experiment, the spacecraft was irradiated isotropically

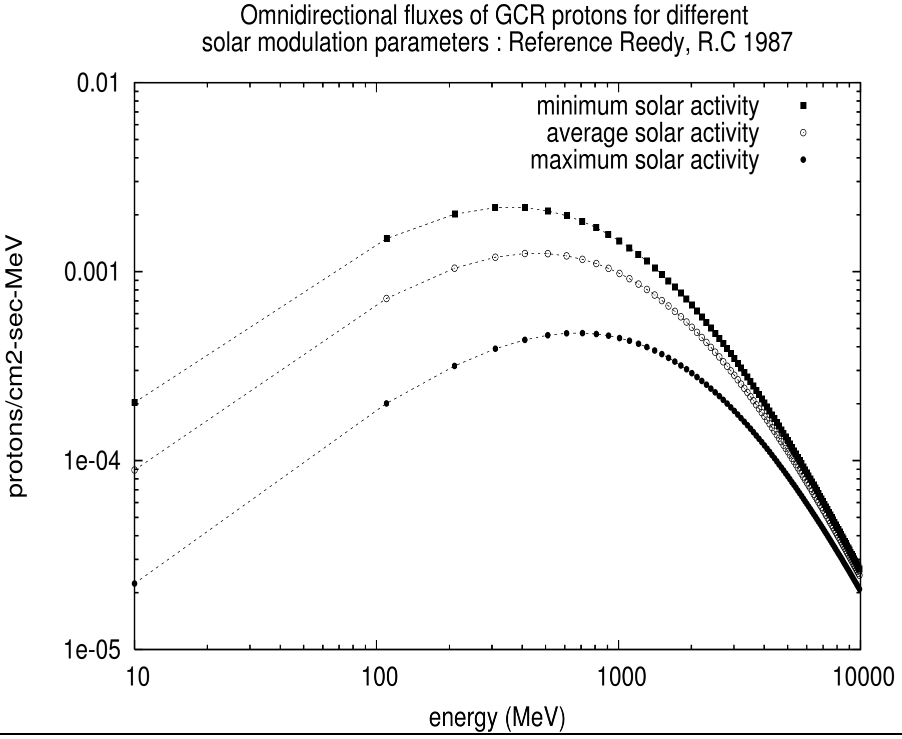

Figure 2.8: Galactic Cosmic Ray proton spectra calculated for different solar modulation parameters. The closed circles, open circles, and closed squares represent the spectra at maximum solar activity, average solar activity and minimum solar activity, respectively. The dashed lines are included in the figure to join the points and do not represent any fit to the values.

by GCR protons and the local production of γ-rays was said to have taken place in material that was on an average 50 g cm^{-2} thick.

The spacecraft and detector were thus modeled as *simple cylinders*, with the detector dimensions and material according to the experiment. The spacecraft material and detector housing were assumed to be Aluminum, and the dimensions of the cylinder making up the spacecraft and detector housing were then computed according to 50 g cm^{-2}.

The detector-spacecraft geometry is shown in fig(2.9), and is referred to as a **mass model**.

- The source spectrum was generated using GSPM; the spacecraft and detector models were placed at the centre of primary particle generator sphere, such that the protons are generated from its surface isotropic in position and launch angle. The GCR proton spectrum for the simulation was calculated from eqn(2.9) for average solar activity.

- The locally produced γ-ray spectrum was detected by the NaI(Tl) detector, and the information was extracted in the *UserEventAction* class for further processing.

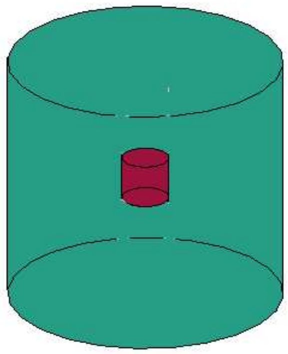

Figure 2.9: Apollo 15 detector-spacecraft mass model; **Green** : spacecraft; **Red** : NaI(Tl) detector

2.6.2 Results

Figure(2.10) shows the comparison between the simulated NaI(Tl) spectrum, locally produced through interaction of GCR protons with the spacecraft mass model and the actual observed spectrum. The small deviations observed could arise from certain approximations and assumptions made. The spacecraft-detector geometry was made as simple as possible, the actual spectral response of the NaI(Tl) detector and a ^{203}Hg source (0.28 MeV) that was used as an onboard calibration source for NaI(Tl) detector were not included in the simulation.

Despite of these simplifications and assumptions, it can be seen from the figure that the simulated spectrum agrees very well with the measured one. The most significant result of the simulation is the excellent match of the strength of the 0.511 MeV electron-positron annihilation line with the experimentally observed line strength. This line is an important feature that is part of the chain of events that occur when very high energy protons interact with matter, leading to the production of electromagnetic showers.

A χ^2_ν goodness-of-fit test was done to measure the compatibility of the simulated spectrum with observed results, with the null hypothesis that the two data sets are equal. Using eqn(2.3), the counting errors due to both distributions were taken into account and the value of χ^2_ν was **1** for ν of 32. From table C.4 of [7b], the tabled value of χ^2_ν for ν 32 and α 0.05 or 5% is 1.444. The computed χ^2_ν is less than the tabled value which means that there is not enough evidence to reject the null hypothesis. Therefore, one can say that the difference between the two data sets is not significant at the 5% level and one can say that the two are equal at the 5% level.

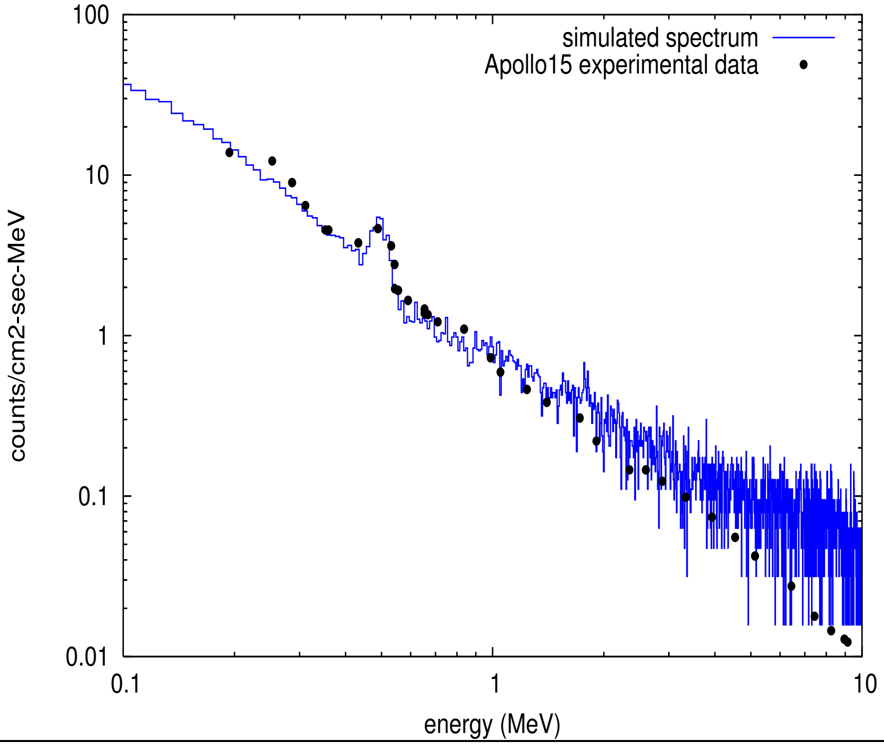

Figure 2.10: Plot comparing the measured and simulated energy spectrum of the NaI(Tl) detector onboard the Apollo 15 spacecraft, due to locally produced γ-rays.

This exercise demonstrates that all the necessary hadronic physical processes that contribute to the generation of photon-electron cascades has been included in the application.

2.7 Simulation of Detector Response

This section briefly discusses the approach to modeling detector response of the CsI and CZT detectors.

The implementation of the detector response in the *UserEventAction* class, using information from the *hits* generated in the *sensitive* detectors is highlighted here. Data obtained from laboratory measurements were used to extract important spectral information such as channel-energy conversion, variation of the spectral width σ with energy, position dependence of the parameters, if any, etc. These simulations help in validating

- detector construction within Geant4
- implementation of the detector response into the *UserEventAction* class.

2.7.1 Simulation of CsI spectral response

Fig(2.11) compares the simulated and measured CsI ACD spectra using the ^{57}Co source (122.1 keV, 136.5 keV). The details of the experimental set up and simulation application design are given in chapter 3.

The x-axis is in channels (1024 channels) and the y-axis is normalized counts, which is defined as the counts per bin divided by the total counts in the spectrum. The photopeak that is seen in the spectra at channel 260 is that of 122.1 keV. The feature at channel 650 in the experimentally measured spectrum is an artificial peak due to saturated background events detected by the crystal arising from events that deposit energy exceeding the upper limit of the electronics design. This effect was not simulated. The asymmetry in the left side of the measured photopeak which causes a visible "hump-backed" structure is due to an artifact of the source-detector geometry that was not modeled, and hence is not present in the simulated spectrum. The 136.5 keV γ-rays are not resolved in the spectra due to the poor resolution of the CsI detector. It can be seen from the figure that the two data sets show an appreciable level of compatibility.

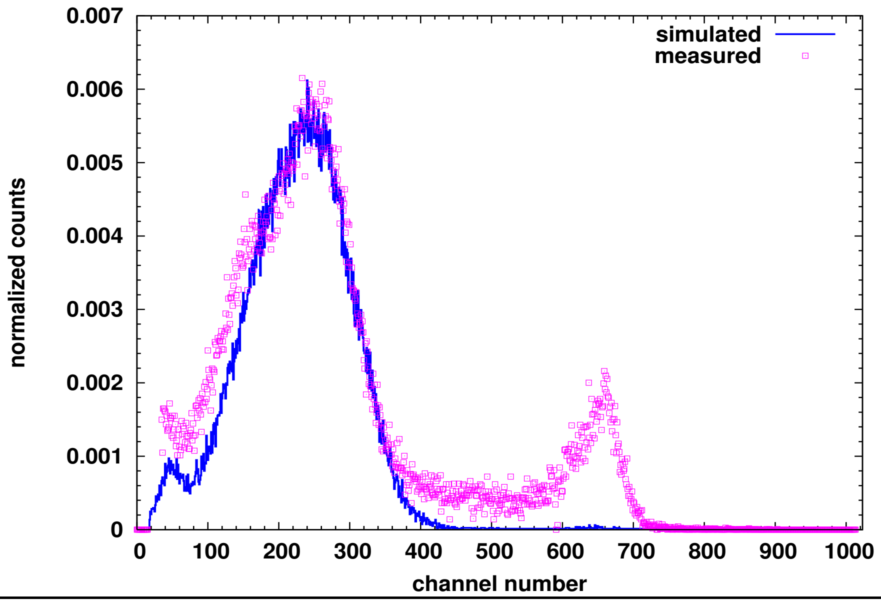

FIGURE 2.11: Comparison between experimentally measured and simulated ^{57}Co - validation of simulation HEX CsI ACD response. The measured and simulated spectra are represented by open squares and solid lines, respectively

2.7.2 Simulation of the CZT detector response

Figure(2.12) is the experimentally measured CZT spectrum of ^{57}Co compared with the simulated spectrum, for one pixel (2.4 mm × 2.4 mm × 5 mm) at a temperature of

5°C. The data was measured in the laboratory using the flight detector module for different temperatures, using an electronics box that was supplied by the vendor of the CZT detector. The details of the data analysis, and extraction of $(\mu\tau)_{e,h}$ products, spectral parameters and the application development will be give in chapter 4. These detector and spectral parameters were incorporated into the *UserEventAction* class of the application.

The x-axis represents channel number (4096 channels) and the y-axis represents normalized counts. Since the resolution of CZT detectors are much better than that of the CsI detector, the 136.5 keV peak is resolved from the 122.1 keV peak. Evidence of hole tailing (discussed in chapter 4) is seen in the low energy region of the 122.1 keV peak. The results show that the spectral response of the CZT detector has been modeled quite satisfactorily using $(\mu\tau)_{e,h}$ products extracted experimentally.

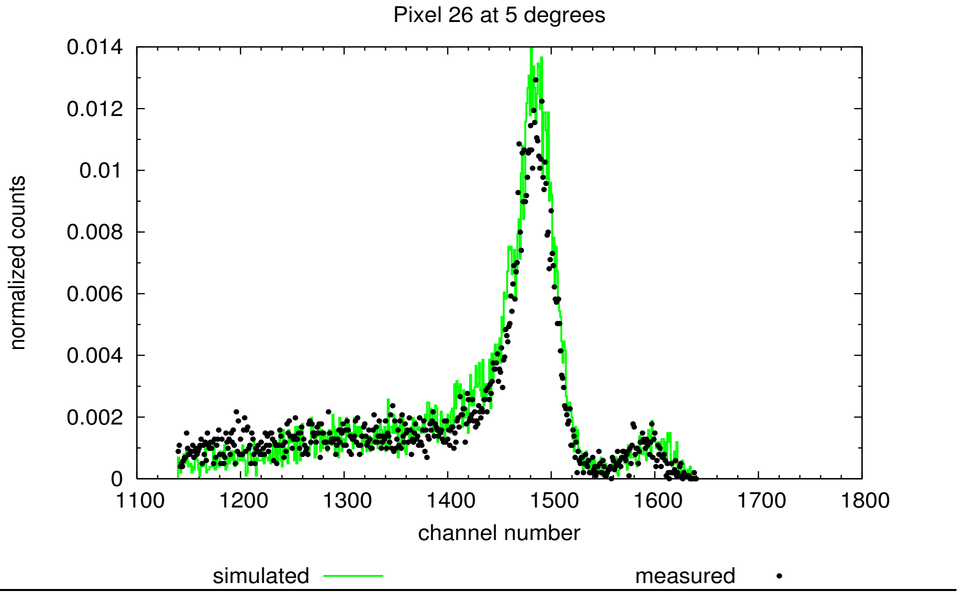

FIGURE 2.12: Comparison between experimentally measured and simulated ^{57}Co at 5°C - validation of simulation of HEX CZT detector response

2.8 Summary and Conclusions

1. The important features of the Geant4 simulation toolkit were listed so as to provide a comprehensive view of its capabilities, stressing on the modularity of the code, and the transparency of the physics to the users. The merits of using the GSPM over the standard Geant4 source-particle implementation was discussed, stressing the fact that GSPM is a tool for use in space applications, instrumentation and nuclear medicine.

2. Simulation of physics experiments is important in every step of the experimental process; from the design of the experimental set up, setting up of the physics relevant to the experiment, defining the output of the experiment, extraction and analysis of the results, and assessing the performance.

3. Validation of the various simulation "stages" is an essential part of the experimental design (outlined above); validation helps build confidence in current results and in predictions of system behavior in varied experimental conditions. It also helps in understanding system limitations.

4. Experimental validation of various aspects of simulation by the author have been presented, with examination of the results with statistical analysis techniques.

5. From this chapter it can be concluded that accurate simulation requires good knowledge about the system that is to be simulated in terms of inclusion of all relevant physics processes, detailed source geometry modeling, good knowledge of the source spectrum, construction of accurate detector geometries, and characterization of detectors in conditions that can be easily simulated.

Bibliography

[1b] http://geant4.web.cern.ch/geant4/UserDocumentation/UsersGuides/ForApplicationDeveloper

[2b] http://geant4.web.cern.ch/geant4/UserDocumentation/UsersGuides/ForToolkitDeveloper

[3b] http://www.space.qinetiq.com/geant4/gspm.html

[4b] http://geant4.web.cern.ch/geant4/UserDocumentation/UserGuides/PhysicsReferenceManual

[5b] Beri, G.C *Business Statistics* Second Edition, Tata McGraw-Hill, New Delhi, 2007

[6b] Downing, D and Clark, J *E-Z Statistics* Barron's Educational Series, New York, 2009

[7b] Bevington, P.R and Robinson, D.K *Data Reduction and Error Analysis for the Physical Sciences*, Third Edition, McGraw Hill, 2003

[8b] Reedy, R.C *Nuclide Production by Primary Cosmic-Ray Protons*, Proceedings XVII Lunar and Planetary Science Conference, Part 2, Journal of Geophysical Research, Volume 92, Number B4, pp E697-E702, 1987

[9b] http://www.physics.csbsju.edu/stats

Chapter 3

The HEX Anti-Coincidence Detector

This chapter discusses the optimization of the the HEX CsI(Tl) anti-coincidence detector geometry using Geant4 and the results from the detector characterization for flight. Various experimental parameters extracted from the data analysis are used to model the response of this detector using Geant4. This response modeling is used to simulate veto logic, and is used in chapter 5 to estimate the veto efficiency for various space radiations.

The main role of the HEX anti-coincidence detector (ACD) is the suppression of Compton continuum in the CZT detector spectrum. It is also used for the rejection of background events due to space radiation environment. Anti-coincidence is an active means to reduce background in a detector, as opposed to the passive method. In the passive method, dense materials with large thicknesses are placed around the detector with the aim of reducing or attenuating penetrating background radiation before it enters the detector.

In a typical active anti-coincidence system, the primary detector is surrounded by secondary detectors, and a pulse produced by the primary detector is accepted only when the secondary detectors *do not* produce a pulse within a time period τ.

A CsI(Tl) (Cesium iodide doped with Thallium) scintillator crystal coupled with two side-mounted PMTs is used as the HEX ACD.

3.1 Pulse Formation in Scintillators

PMTs are devices that are used with scintillator detectors to convert their light output to electrical signals. A PMT consists of

- a **photocathode**, which emits electrons via the photoelectric effect when scintillation photons interact with it
- a series of **dynodes**, which form the electron multiplication section
- the **anode** which collects the total charge generated

These components are housed in an evacuated glass envelope.

When a scintillation light photon is incident on the photosensitive material of the photocathode, an electron is emitted by the photoelectric effect, with kinetic energy equal to the difference between the energy of the incident photon and the binding energy of the electron in the atom of the photocathode material. The photoelectron loses energy in the material due to collisions with other electrons. If it has to escape from the material, the energy that it is left with after the collisions should be greater than the work function or potential barrier of the material. These photoelectrons are called primary electrons. One can define the quantum efficiency (QE) of the photocathode, as the ratio of the number of photoelectrons emitted by the photocathode to the number of scintillation photons incident on it. It is a function of wavelength of the scintillation light. Typical values of QE for bialkali photocathodes is 30-40%.

The electron multiplication section, represented by a series of dynodes, amplifies the number of primary electrons by a factor of about 10^6. The first dynode has a positive potential with respect to the photocathode, and the others have progressively higher voltage values. The primary electrons are accelerated to the first dynode by the potential difference, and strike it with a kinetic energy that is dependent on this potential difference. These energetic primary electrons now knockout electrons from this dynode. These are the secondary electrons and they escape to vacuum after overcoming the work function of the dynode material. The number of secondaries emitted depends on the kinetic energy of the primaries. The secondaries emitted by the first dynode are accelerated towards the second dynode, which has a relatively higher potential, and so strike it with a higher kinetic energy. More electrons are emitted from the second dynode. This process is repeated with more and more secondaries being emitted as the potential difference between the dynodes increases.

In this way, an amplification of the number of primaries takes place and a burst of 10^6-10^7 electrons reach the anode.

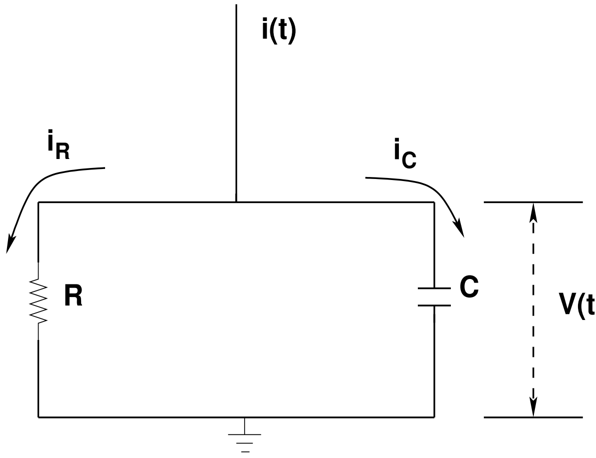

FIGURE 3.1: Schematic of PMT anode circuit (adopted from [4a]); i(t) is the total current flowing into the parallel RC circuit in time 't', $\mathrm{i_R}$ is the current through the resistor R, and $\mathrm{i_C}$ is the current through the capacitor, C; V(t) represents the voltage at the anode.

The anode can be represented by an equivalent R-C circuit, as shown in fig(3.1). C is the combined capacitance of the anode, the connecting cable, and that of the circuitry, while R represents the input impedance of the anode circuit. The current of electrons that reach the anode is due to a single scintillation emission. The emission has a decay constant λ. According to [4a]

$$i(t) \quad = \quad \lambda Q e^{-\lambda t} \tag{3.1}$$

where Q is the total charge collected over the pulse. The current flow is assumed to start at time t = 0.

From the fig(3.1) it can be seen that the total current flowing into the parallel RC circuit is the sum of the current through the capacitor, i$_C$ and the current through the resistor, i$_R$. What needs to be determined from this current is the time profile of the total expected voltage, V(t) at the anode.

$$\begin{aligned} i(t) &= i_C + i_R \\ &= \frac{dQ}{dt} + \frac{V(t)}{R} \\ &= C\frac{dV(t)}{dt} + \frac{V(t)}{R} \end{aligned} \tag{3.2}$$

From this we get the equation

$$\frac{dV(t)}{dt} + \frac{1}{RC}V(t) = \frac{\lambda Q}{C}e^{-\lambda t} \tag{3.3}$$

The solution of the this equation is

$$V(t) = \frac{1}{\lambda - \theta}\frac{\lambda Q}{C}(e^{-\theta t} - e^{-\lambda t}) \tag{3.4}$$

where $\theta = \frac{1}{RC}$, the reciprocal of the time constant of the parallel circuit.

In cases where the amplitude of the pulse, Q/C is to be preserved, the anode time constant RC must be large compared to the scintillation decay constant or $\theta << \lambda$. Then eqn(3.4) is reduced to

$$V(t) = \frac{Q}{C}(e^{-\theta t} - e^{-\lambda t}) \tag{3.5}$$

Now, the time profile of the voltage pulse can be divided into two parts

- t $<< \frac{1}{\theta}$
  The first exponential becomes unity and eqn(3.5) becomes

  $$V(t) = \frac{Q}{C}(1 - e^{-\lambda t}) \tag{3.6}$$

  This is the behavior of the leading edge of the pulse, as illustrated in fig(3.2), where the rise time is determined by the scintillator decay constant, λ.

- t $>> \frac{1}{\lambda}$
  The second exponential becomes zero and eqn(3.5) become

  $$V(t) = \frac{Q}{C}e^{-\theta t} \tag{3.7}$$

  This is the behavior of the tail of the puls,e as illustrated in fig(3.2), and is purely determined by the anode time constant.

The amplitude of the pulse in this case reaches the maximum Q/C only if the anode time constant is much larger than the scintillator decay time. Fig(3.2) shows the time profile of the anode voltage pulse. The detection system is operated in this mode when the application requires pulse height spectroscopy.

The measurement of the arrival time of a pulse is called **timing**, and can be determined by studying the time profile or time development of a voltage pulse. The time at which the leading edge of a pulse crosses a certain set voltage threshold is *time of arrival* of the pulse. The study of time profiles can be used in many applications like measuring the rate of coincidence between two events. When time of arrival of two pulses is used to accept one of the pulses, it is called **coincidence** and when it is used to discard one of the pulses it is called **anti-coincidence**.

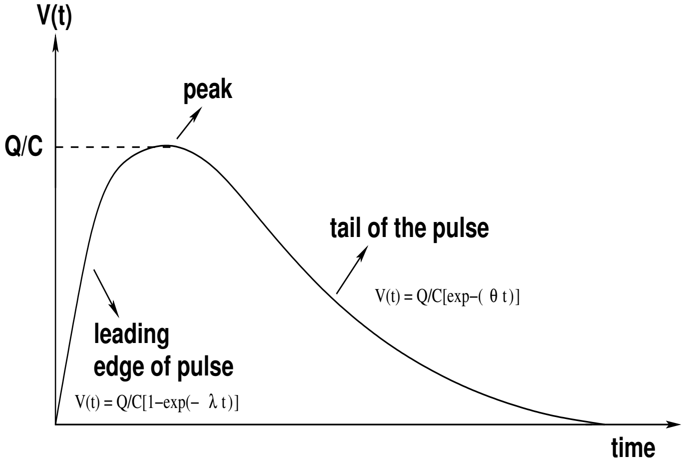

FIGURE 3.2: Time profile of the anode voltage pulse for the case when the anode time constant is very large compared to the scintillation decay constant.

Since the HEX ACD operates on the principle of anti-coincidence, this technique will be briefly discussed in the next section.

3.2 The Principle of Anti-Coincidence

When two pulses from two independent detectors arrive at the same time it is called **true coincidence**, but this hardly occurs in nature. Therefore, a *coincidence window* τ is defined, such that they are said to be coincident if they occur within τ. The width of the coincidence window depends of the type of detector being used and ranges from nanoseconds (1-10 ns) for "fast" detectors to microseconds (1-5 μs) for "slow" detectors.

When event pulses generated by two appropriately placed detectors arrive within τ, the pulses are rejected; they are accepted only if they **do not arrive within** τ. Such a system is said to operate in the anti-coincidence mode. The pulse rejection or "veto" action is irrespective of the time of arrival of the events within the window, so long as both are detected within τ. This principle is illustrated in the fig(3.3).

As discussed in chapter 1, CsI(Tl) is used as the anti-coincidence detector (ACD) of the HEX experiment and it is used to reject events that are Compton scattered from the primary CZT detector. This is called **Compton suppression** and represents events that scatter from *in-to-out*, i.e. scatter from the CZT to the ACD. Also, since the anti-coincidence logic does not depend on which signal is detected first within τ, the ACD is also useful in rejecting background in the CZT that are due to events that are generated first in the ACD and then scatter into the CZT, i.e. *out-to-in* events.

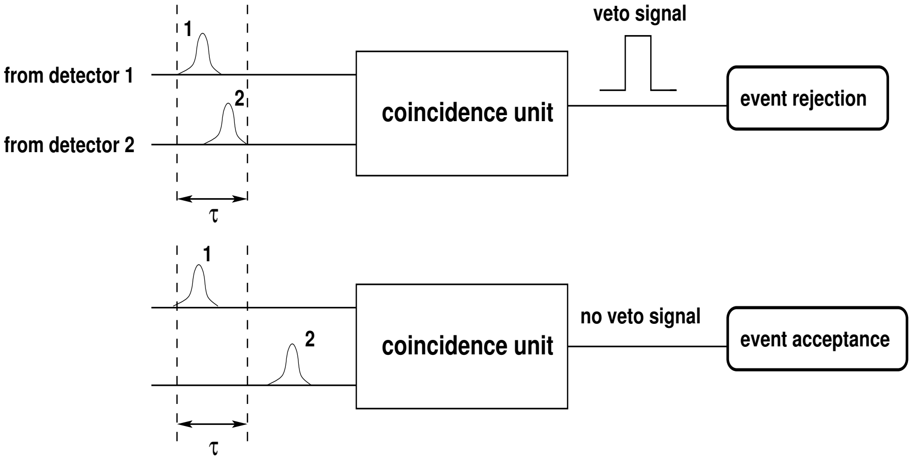

FIGURE 3.3: Simplified schematic of anti-coincidence logic. Two events 1 and 2 generated by detectors 1 and 2 respectively, are fed into a coincidence unit. **Top:** The two events arrive within the time interval τ, hence a veto signal is generated and event 2 is rejected; **Bottom:** The two events do not arrive within τ, hence event 2 is accepted.

For the HEX experiment, if signals are generated by the CZT and ACD within $\tau = 3.5$ μs, the corresponding CZT event is "tagged" and stored for rejection at a later stage. Thus, CZT spectra can be constructed including the tagged events, as well as after removal of tagged events. This is very useful if a comparative study of the two spectra needs to be done. The CZT spectra measured onboard Chandrayaan-I which includes the tagged events, is scientifically important as it gives an idea of the background seen by the detector in lunar orbit.

The next section discusses the properties of Cesium iodide scintillators.

3.3 The Cesium Iodide Scintillator

Cesium Iodide (CsI) is an attractive material for use as a radiation detector for space-based applications. This is due to its

- high density ($\rho = 4.51$ gcm^{-3}) and effective atomic number ($Z_{eff} = 52$)
- robust; can withstand mechanical and thermal shock and vibration
- not hygroscopic; need not be housed in hermetically sealed containers

CsI by itself can be used as a scintillator material and it emits scintillation photons with a maximum wavelength of 315 nm. The scintillation decay time is ~20 ns. It yields 2×10^3 light photons per MeV of deposited energy.

To enhance the probability of emission of scintillation photons, the crystal is **doped** with small amounts of **activators**, like Thallium or Sodium, resulting in CsI(Tl) and CsI(Na) having very different scintillator properties.

CsI(Na) is hygroscopic and must be hermetically sealed. Its maximum wavelength of emission is at 420 nm. Its scintillation light yield is 3.9×10^4 light photons per MeV, which is of the same order as that for NaI(Tl).

CsI(Tl) is the inorganic scintillator with the highest absolute scintillation yield of 6.5×10^4 photons per MeV of deposited energy. The emission spectrum of CsI(Tl) peaks at 540 nm. The CsI(Tl) scintillation emission shows two components; a fast component that occurs 64% of the time, with a scintillation decay time of 0.64μs, and a slow component with a decay time of 3.34 μs, occurring 36% of the time.

The scintillation light output of CsI(Tl) depends on temperature. According to [5a], and references therein, the scintillation light output increases steeply from -70°C to peak at 50°C, after which it begins to decrease slowly with increasing temperature.

The most common manifestation of radiation damage in scintillation crystals is the formation of *radiation induced* absorption bands for the scintillation photons, called **color centres**. These centres reduce the scintillation output of the crystal, which can be determined by measuring the transmission of the crystal. Crystals damaged by radiation can be recovered by **room temperature annealing**, and the speed of recovery depends on the depth of formation of these photon traps. Radiation damage can interfere with the scintillation emission process as well, and can also cause phosphorescence or afterglow, which manifests itself as an increase in readout noise.

This chapter focuses on the simulation of HEX CsI(Tl) detector response and discusses the

- experimental characterization of the detector in terms of light collection over the detector surface
- extraction of position-dependent spectral parameters

The parameterization of these experimental results is an essential part in modeling the CsI(Tl) response.

However, an important part of this chapter is the optimization of the CsI(Tl) ACD geometry for the HEX experiment using Monte Carlo simulations, thus helping to bring the weight of the instrument within the limits specified by spacecraft constraints. These results also helped in finalizing the ACD geometry in the final instrument.

3.4 Design Optimization of ACD using Geant4

Compton scattering results in partial energy deposition in the detector material, and is the most probable photon interaction process in the energy range 100 keV $\lesssim$ E $\lesssim$ 0.5 MeV. The dynamics of Compton scattering are illustrated in the fig(3.4), where $h\nu$ is the energy of the photon i.e. incident on an electron of the medium, and $h\nu'$ is the energy of the scattered photon. Compton interaction results in photon scattering accompanied by electron recoil. Part of the incident photon energy is transfered to the electron and this fraction depends on the angle of scattering, θ. The energy of the scattered photon, $h\nu'$ is given in terms of θ by

$$h\nu' = \frac{h\nu}{1 + (h\nu/m_0c^2)(1 - \cos\theta)} \tag{3.8}$$

where m_0c^2 is the rest mass energy of the electron.

The kinetic energy of the recoil electron is given by

$$\begin{aligned} E_{e^-} &= h\nu - h\nu' \\ &= h\nu \left(\frac{(h\nu/m_0c^2)(1 - \cos\theta)}{1 + (h\nu/m_0c^2)(1 - \cos\theta)} \right) \end{aligned} \tag{3.9}$$

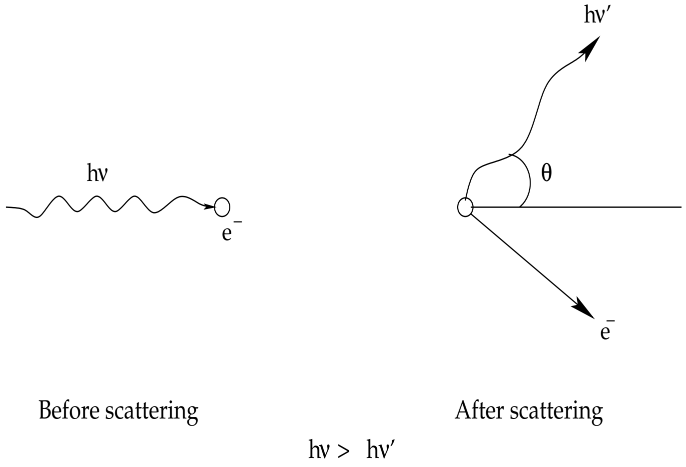

FIGURE 3.4: Dynamics of Compton Scattering

Consider a detector, with photons of energy $h\nu$ incident on it. When θ is close to 0, which is called "grazing angle scattering", it can be seen from eqn(3.9) that $h\nu \approx$ hν', and $E_{e^-} \sim 0$. This means that the energy deposited in the detector material (i.e. energy of the recoil electron) ~ 0, and the photon hardly loses energy. When θ is 180°, "backscattering" occurs, and the energy of the scattered photon and recoil electron are given by

$$h\nu'|_{\theta=180^\circ} = \frac{h\nu}{1+(2h\nu/m_0c^2)} \tag{3.10}$$

$$E_{e^-}|_{\theta=180^\circ} = h\nu\left(\frac{2h\nu/m_0c^2}{1+(2h\nu/m_0c^2)}\right) \tag{3.11}$$

The *Klein-Nishina* formula in eqn(3.12) gives the angular dependence of the Compton scattered photons, i.e. the number of photons scattered into unit solid angle at a scattering angle θ, and this can be written as

$$\begin{aligned}\frac{d\sigma}{d\Omega} = Zr_0^2 &\left(\frac{1}{1+\alpha(1-\cos\theta)}\right)^2 \\ &\left(\frac{1+\cos^2\theta}{2}\right)\left(1+\frac{\alpha^2(1-\cos\theta)^2}{(1+\cos^2\theta)[1+\alpha(1-\cos\theta)]}\right)\end{aligned} \tag{3.12}$$

where dσ/dΩ is defined as the differential scattering cross-section, $\alpha = h\nu/m_0c^2$, and r_0 is the classical electron radius. The differential scattering cross-section has been calculated using above equation for energies from 1 keV - 2 MeV, for angles from 0° to 180°, and is plotted in fig(3.5).

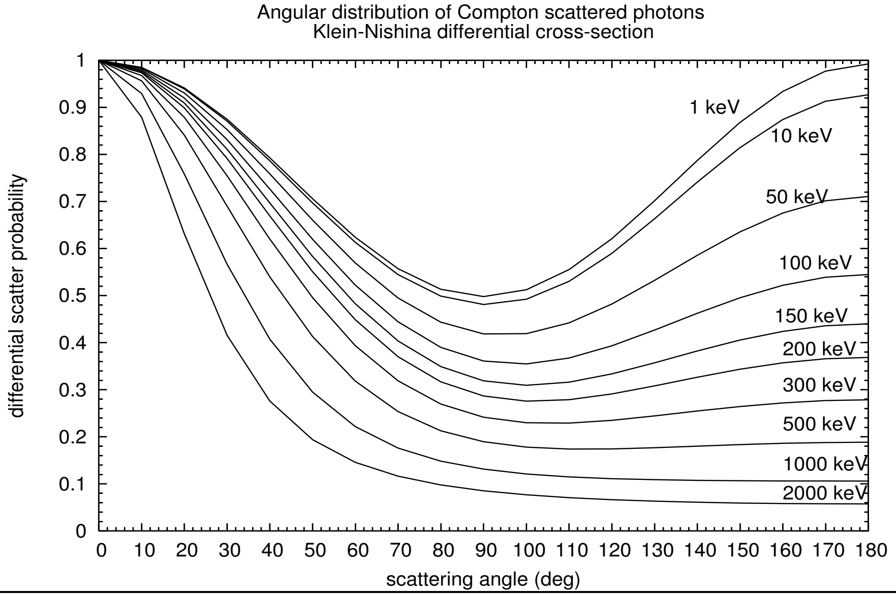

FIGURE 3.5: The differential Compton scatter probability in units of cm^2 per unit solid angle for photons of different energies, as a function of scattering angle, θ. As can be seen from this plot, the scatter probability tends to the forward direction ($\theta < 90^\circ$) as the photon energy increases.

In this plot, backscattering refers to all those angles greater than 90° and forward-scattering to all those angles less than 90°. As can be seen, the probability for forward scattering increases with photon energy. Since all scattering angles can occur it can be seen from fig(3.6) that a continuum of energy deposits results in the detector, from 0 to $E_{e^-}|_{\theta=180^\circ}$.

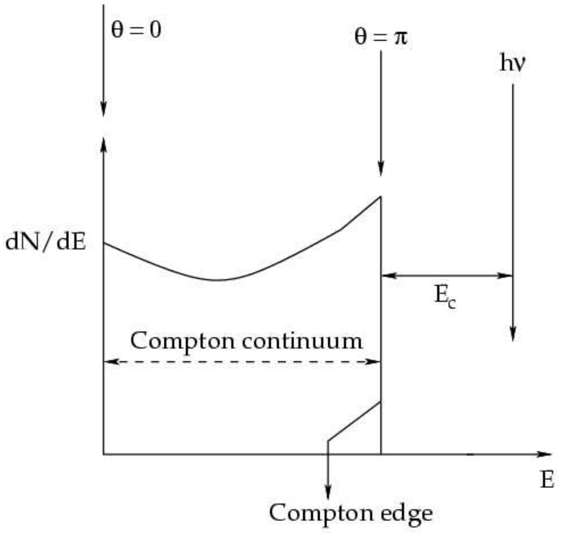

FIGURE 3.6: Schematic of Compton continuum. Here, E_c = hν - E_{e^-}, where E_{e^-} is the energy of the recoil electron

This continuum becomes a background against which spectroscopic measurements have to be made. If the spectral lines important to the experiment are weak and lie in the low energy part of the continuum, they get submerged in this background. The continuum can be suppressed by suitably placing secondary detectors around the primary detector and applying anti-coincidence techniques. Compton scattered photons that escape from the main detector produce signals in the secondary detectors. According to the principle of anti-coincidence discussed in section 3.2, when the secondary and main detectors produce signals within the coincidence window τ, the corresponding main detector event is rejected. In this way, deposition of energy due to Compton recoil electrons is suppressed and the Compton continuum background is reduced.

An ideal ACD is one which surrounds the primary detector on all sides, except that side through which the radiation must enter. *Due to the weight constraints imposed on the HEX experiment by the spacecraft, it was very important to optimize the design of the ACD geometry with respect to saving weight.* Geant4 has been used to optimize the design of the ACD geometry with regard to

- Shielding geometry - choosing between the best among
    - Ideal shielding geometry

  - Shielding only four sides of the primary detector
  - Shielding only the bottom of the primary detector
- Thickness of the ACD - can the ACD thickness be reduced without loosing considerable veto efficiency.

The veto efficiency or the fraction of events that are rejected by the ACD, is expressed in terms of the **Compton Suppression Efficiency (CSE)**. This is defined as the ratio between the coincident counts in the CZT and ACD (i.e. the difference between counts in CZT without ACD and counts in CZT with ACD) to the counts detected in the CZT detector without ACD logic, expressed as a percentage.

Mathematically, this definition can be written as

$$\mathrm{CSE\%} = \frac{C_{\mathrm{noACD}_{\Delta E}} - C_{\mathrm{ACD}_{\Delta E}}}{C_{\mathrm{noACD}_{\Delta E}}} \times 100 \tag{3.13}$$

where
$\mathrm{C}_{\mathrm{noACD}_{\Delta E}}$ are the counts in CZT energy spectrum without ACD logic active
$\mathrm{C}_{\mathrm{ACD}_{\Delta E}}$ are the counts in CZT energy spectrum with ACD logic active
ΔE is energy range of interest.

3.4.1 Geant4 Application Design

Geant4 geometry construction was used to model the CZT detector and ACD geometry. The modeled CZT detector geometry consisted of nine CZT modules arranged in a 3×3 matrix, with the specified dimensions and materials. Various ACD geometries were studied in order to arrive at an optimized design. Appropriate materials were used to model the ACD. The source geometry was simulated using GSPM as a plane square, with cosine angular distribution. The generated photons were isotropic in terms of position on the generator plane and launch direction. The source used for the simulation was the lunar gamma-ray albedo (LGRA) spectrum from [1e] as illustrated in fig(5.2). The energies of these photons range from 1 keV to 10 MeV The source-detector geometry is shown in fig(3.7). The physics processes included in the Geant4 simulation are listed in the table 2.3.

The CZT detector array and the CsI ACD were made *sensitive*. This means that certain functionalities were included to facilitate the extraction and storage of information concerning the energy deposition by the incident particle. The energy deposited in the CZT detector is obtained by extracting the *hits* information in the *UserEventAction* class using the object of the *G4HCofThisEvent* class. In the *UserEventAction* class, the

ACD logic is applied through the following condition: **during an event, if there are hits registered by both the CZT and ACD, the CZT energy deposit is not saved; else the CZT energy deposit for that event is saved**. Those events that make up the latter, constitute the *Compton suppressed CZT energy deposit spectrum.* In addition, this application also produces the CZT energy deposit spectrum which includes CZT Compton scattered events and this constitutes the *Full CZT energy deposit spectrum.* In both cases only those events which deposit energy in the CZT within the 30-270 keV range were stored.

Four experimental setups were simulated for ACD geometry optimization:

1. CZT detector array surrounded on four sides and bottom by the ACD. This is the **five component configuration**. The dimensions of a side ACD is 14 cm × 2.5 cm × 2.5 cm, while that of the bottom ACD is 14 cm × 14 cm × 2.5 cm. The thickness of 2.5 cm or 1 inch is a conservative choice for the shielding material. The Geant4 application is executed for two cases :

    - ACD logic inactive
    - ACD logic active

    The counts under the spectra in both cases are used to compute the CSE for this experiment.

2. CZT detector array surrounded on four sides by ACDs with dimensions as specified above. This is the **four component configuration**. The Geant4 application is executed for the cases listed above, and the corresponding CSE computed.

3. CZT detector array having one ACD placed below it with dimensions as specified above. This is the **single component configuration**. The Geant4 application is executed for the cases listed above, and the corresponding CSE computed.

4. Depending on the result of the above experiments, the appropriate ACD geometry is selected. The CSE is then computed for different thicknesses of ACD, ranging from the conservative 2.5 cm to 1 cm, in steps of 0.5 cm.

3.4.2 Simulation results

Figures (3.8) and (3.9) show two plots -

- the *Full energy* deposit spectrum and the *Compton suppressed* energy spectrum for the four component configuration

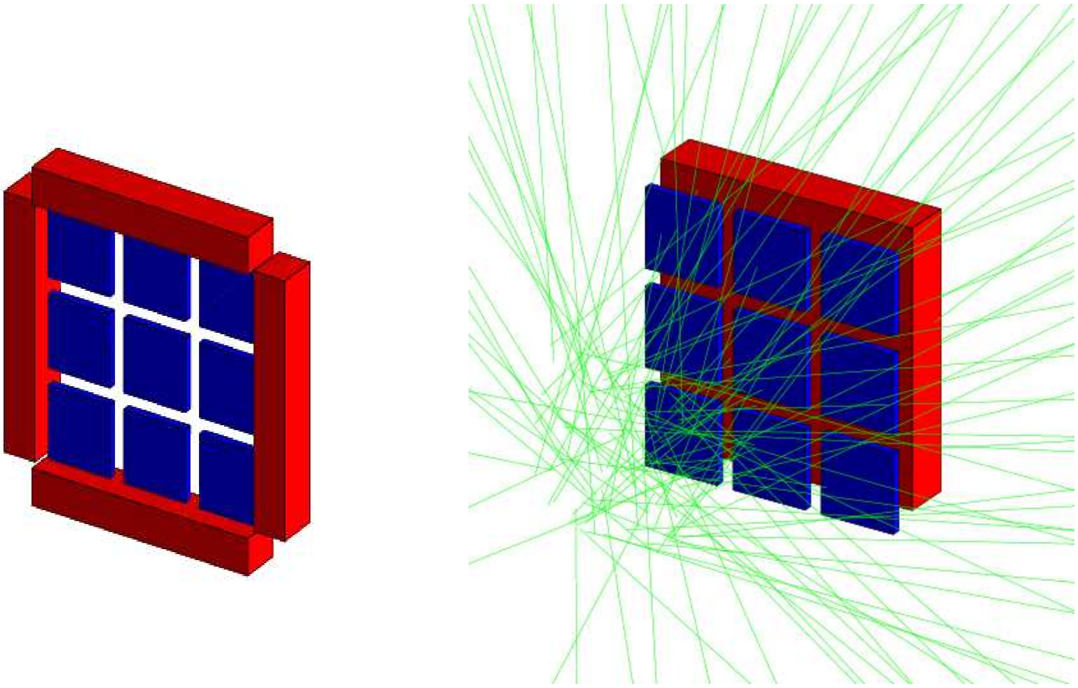

FIGURE 3.7: The Geant4 CZT-ACD model, with the nine CZT modules in blue and the CsI ACD in red; **left** : detector geometry for the four component configuration; **right** : detector geometry for single component configuration, the source geometry is also shown here

- the *Full energy* deposit spectrum and the *Compton suppressed* energy spectrum for the single component configuration

The y-axis units are normalized counts per incident photon. As can be seen from both sets of plots, the Compton suppressed energy spectrum due to the single component configuration shows a visible rejection of Compton scattered events over the entire energy range of 30-270 keV, with almost a factor of 2 background rejection in the 30-60 keV region where the 46.5 keV line is located, thus increasing its sensitivity. Compared to this, the background rejection due to the four component configuration is insignificant over the full energy range.

Putting these observations into a quantitative perspective, the CSE due to the

- five component configuration is 21%
- four component configuration is 5%
- single component configuration is 16%

At this stage we define a minimum criteria of 10% for CSE in order to determine the cut off veto efficiency of a particular ACD geometry. From this we can see that the CSE of the four component configuration is significantly lower than the minimum CSE cut off, and thus need not be considered as a meaningful configuration.

According to the Klein-Nishina formula, higher energy photons have a greater forward-scatter probability, and from Compton dynamics, photons that scatter in the forward direction, i.e. at small angles with respect to the detector axis, scatter with most of the energy of the incident photon. This results in low energy recoil electrons which deposit energy in the low energy region of the spectrum. Thus, the single component configuration takes care of the forward scattered events and suppresses low energy CZT events, when compared with the four component configuration.

The computed CSEs also indicate that with respect to the ideal ACD geometry, the bulk of rejection occurs due to the single ACD placed at the bottom of the CZT.

One can express the CSE in units of CSE per unit mass, which is a general unit for representing the veto efficiency corresponding to the total ACD mass. Taking this into account, it can be seen that the CSE per unit mass for the ideal ACD geometry and the single component geometry are $8.03\%\mathrm{kg}^{-1}$ and $7.21\%\mathrm{kg}^{-1}$ respectively, which is not a very significant difference. This shows that the rejection efficiency of the single component configuration is as good as the ideal configuration as far as the HEX experiment is concerned.

Therefore considering the spacecraft weight restrictions, it can be concluded that the bottom ACD is sufficient to take care of Compton suppression of the CZT spectrum over the entire energy range, and more importantly, in the low energy part of the spectrum. Elimination of side ACDs from the geometry results in a 41.7% reduction in shield weight.

Once the ACD shielding geometry has been optimized and defined, the next aim is to determine whether the thickness of the bottom ACD can be reduced without significantly altering the CSE.

The source-detector geometry is the same as that shown in the right panel of fig(3.7), except that for each simulation, the thickness of the bottom ACD is reduced in steps of 0.5 cm, from 2.5 cm to 1 cm. The plot in fig(3.10) shows the energy deposit spectra in the CZT detector in the 30-70 keV region (region of interest with respect to the 46.5 keV line), for the following cases :

- ACD logic not activated
- ACD logic activated for
  - 2.5 cm thick ACD

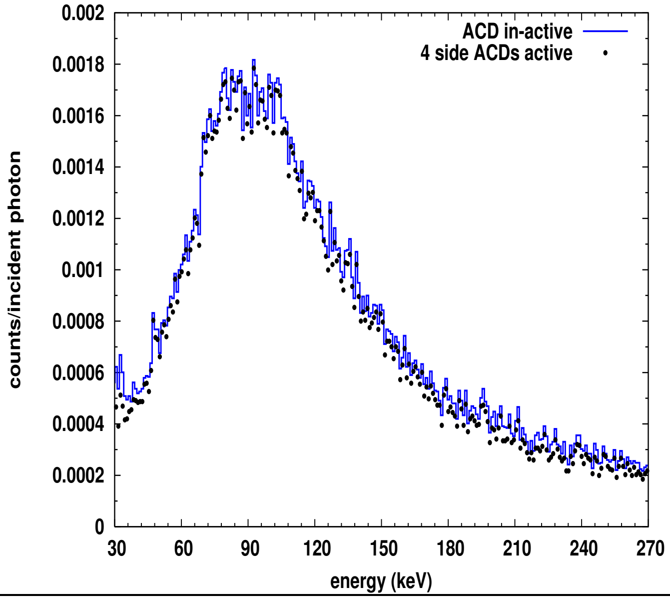

FIGURE 3.8: Energy deposit spectra in CZT detector; four side ACD, logic in-active (solid line) and active (closed circles)

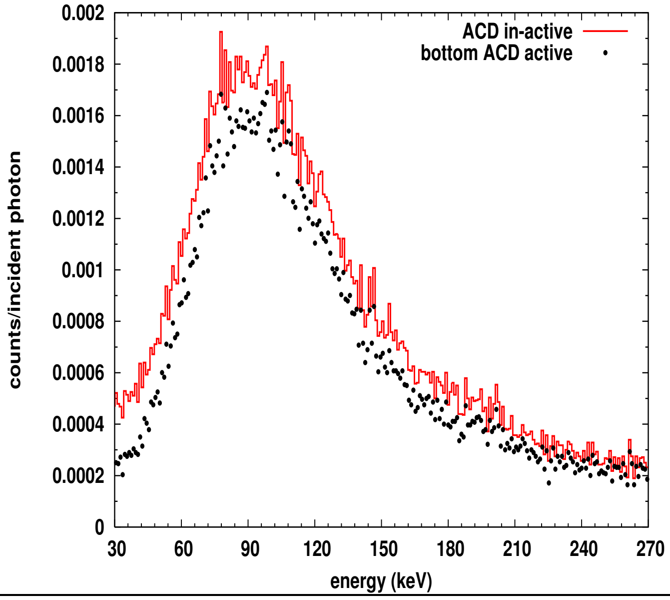

FIGURE 3.9: Energy deposit spectra in CZT detector; bottom ACD, logic in-active (solid line) and active (closed circles)

- 2.0 cm thick ACD
- 1.5 cm thick ACD
- 1.0 cm thick ACD

The y-axis is normalized to units of counts per incident photon.

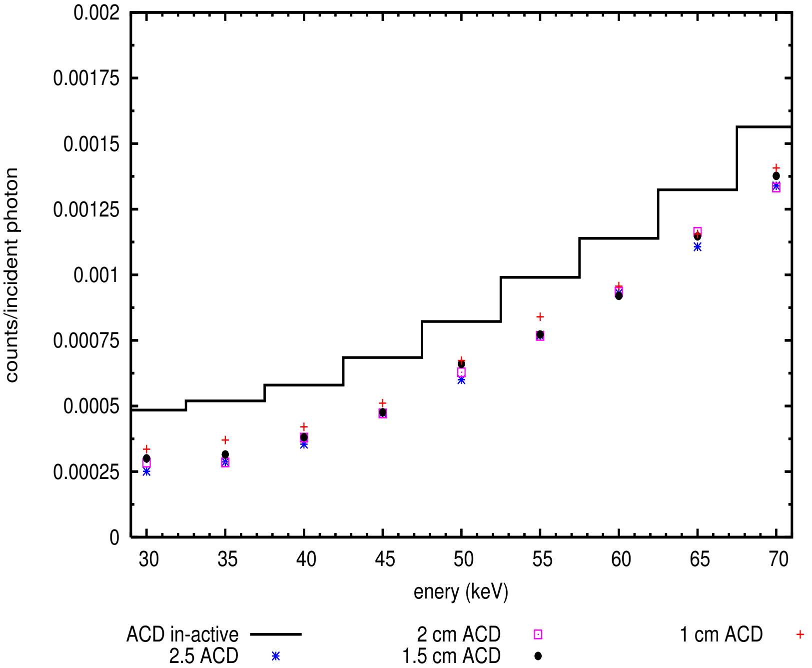

FIGURE 3.10: Energy deposit spectra in CZT in the 30-70 keV region. The solid line represents the CZT spectrum without ACD logic active, while the points symbolize the energy deposit with activated ACD logic. The representation of the symbols are given as legends in the figure. Error bars not shown in the figure to avoid crowding.

The plot shows that though the 2.5 cm thick ACD shows lowest counts per bin, the differences between the counts per bin for each geometry is insignificant within simulation errors. For each of the ACD thicknesses, the computed CSEs for the 30-270 keV energy range are all above the 10% cut off. The CSE per unit mass for each thickness is plotted in the fig(3.11) and it can be seen that the 1 cm thick ACD has most efficient in *in-to-out* background rejection relative to the other thicknesses. When compared with the 2.5 cm ACD, choosing the 1 cm thick detector corresponds to a 60.2% reduction in subsystem weight.

In conclusion, Geant4 has been used to optimize the shielding geometry with respect to Compton suppression in the CZT energy deposit spectrum. Using these results, the flight design of the HEX ACD was finalized to one CsI detector of dimensions 14 cm × 14 cm × 1 cm placed beneath the CZT detector.

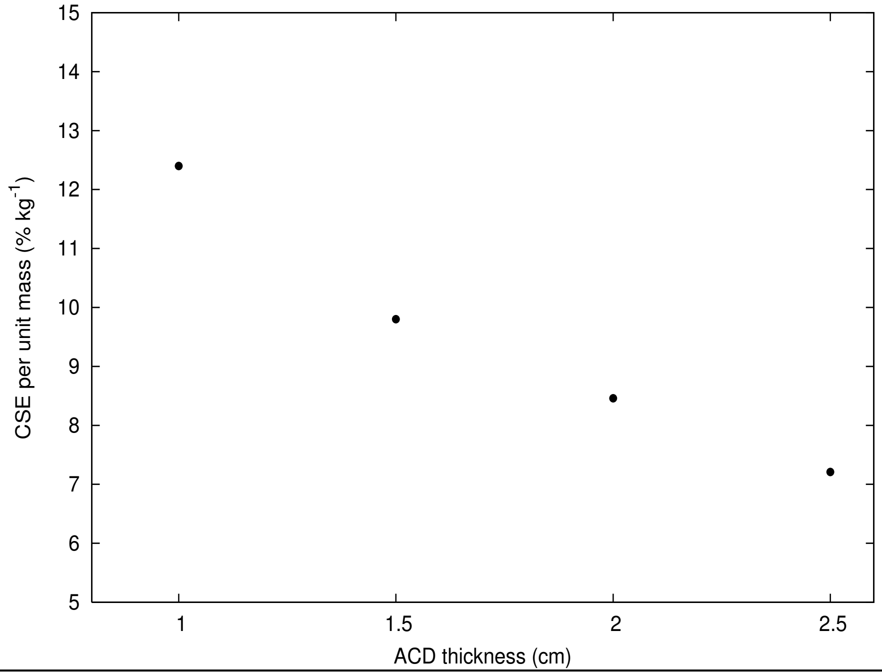

FIGURE 3.11: CSE per unit mass (%kg^{-1}) plotted as a function of ACD thickness (cm)

Since one of the goals of this thesis is to predict the background rejection efficiency of the ACD for various lunar environments, it is a necessary requirement to include the detector response of the ACD in the final simulation. A first step towards achieving this is to characterize the ACD in the laboratory as functions of energy and position with respect to the PMTs. The pulse height spectra of the ACD would be simulated with Geant4 using parameterized equations of the ACD response. The modeled response would then be validated against experimentally measured pulse height spectra, and this would be used to establish confidence in the methodology, along with the approximations and assumptions applied. The next sections discuss the experimental characterization of the ACD as well as the simulation of the pulse height spectra for different photon energies.

3.5 Experimental characterization of the ACD

3.5.1 Light collection and effects on spectral performance

When high energy radiation interacts with a scintillator, light is emitted isotropically and it is essential to collect as much of this light as possible. Scintillation photons undergo multiple reflections within the crystal and a fraction of these photons is lost during these reflections. This fraction becomes large when the light takes a longer path in the crystal before reaching the PMT. The interface between the crystal and the PMT also contributes to the loss of light, so that the number of scintillation photons that finally reach the photocathode is less than the number of photons originally emitted. As discussed earlier, the photocathode has a QE for conversion of scintillation light into photoelectrons, which is a strong function of the wavelength of light and material of the photocathode. Therefore, only a fraction of the scintillation photons that reach the photocathode are converted to photoelectrons.

This means that independent of the QE of the photocathode, the voltage pulse height that is measured at the output will be affected by the number of scintillation photons that reach the photocathode or by the light collection efficiency of the photocathode.

The description of the CsI ACD instrumentation was discussed in section 1.2.3. Figure(3.12) is a schematic which shows the ACD as viewed from the top. Due to payload

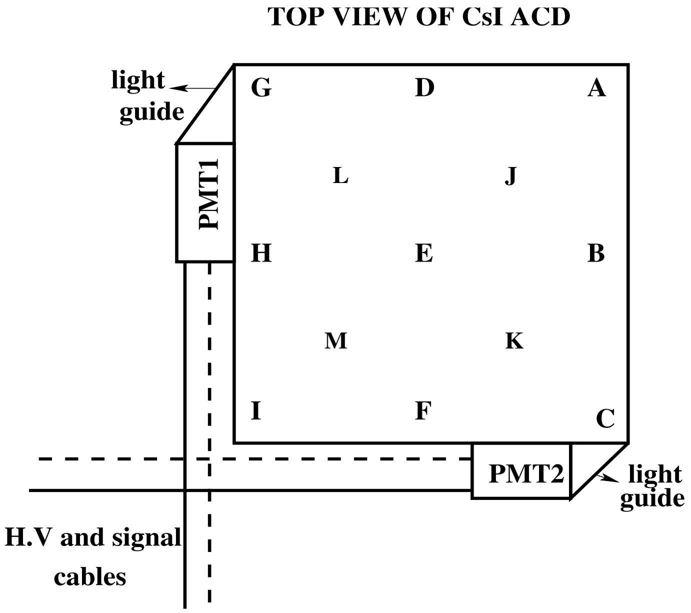

FIGURE 3.12: Schematic diagram of top view of the HEX ACD; the CsI crystal is shown from the top side, with the side mounted PMTs. The light guide prisms, depicted by the two right-angled triangles, is the interface between the crystal and the PMTs. The high voltage (HV) and signal cables for the two PMTs are also shown. The labels on the crystal indicate the locations on the surface, with respect to the PMTs at which measurements were made for experimental characterization

related space constraints, the PMTs were mounted on the sides of the CsI(Tl) crystal, with prisms used as light guides, as shown in fig(3.12). Both PMTs are biased using the same HV value of 690 V, and therefore, should have approximately the same multiplication factor or gain.

The top panel of fig(3.13) shows the pulse heights measured by PMT1 at different distances along the diagonal of the crystal, relative to the pulse height measured near the PMT. The bottom panel of the figure indicates the same for PMT2. Since the relative pulse heights are measured at the end of the signal chain after taking into account all the processes that occur in the system related to light loss, we can define the relative pulse heights as the *light collection efficiency.* Therefore, the light collection efficiency near a PMT is much higher than for a location at the centre of the crystal.

Though both the PMTs should show the same relative pulse height for the source at the same distance from the tube, PMT2 shows a larger value, probably from differences in inherent gain between the two. Correcting for this, one can study the light collection efficiency of the PMTs with respect to this geometric arrangement. The difference between the light collection efficiency measured closest to a PMT and that measured farthest from a PMT is ∼10%, averaged over all energies. Since the light collection efficiency shows dependence on the position of the photon source relative to the PMTs, it is essential to characterize the detector as a function of position on the crystal surface.

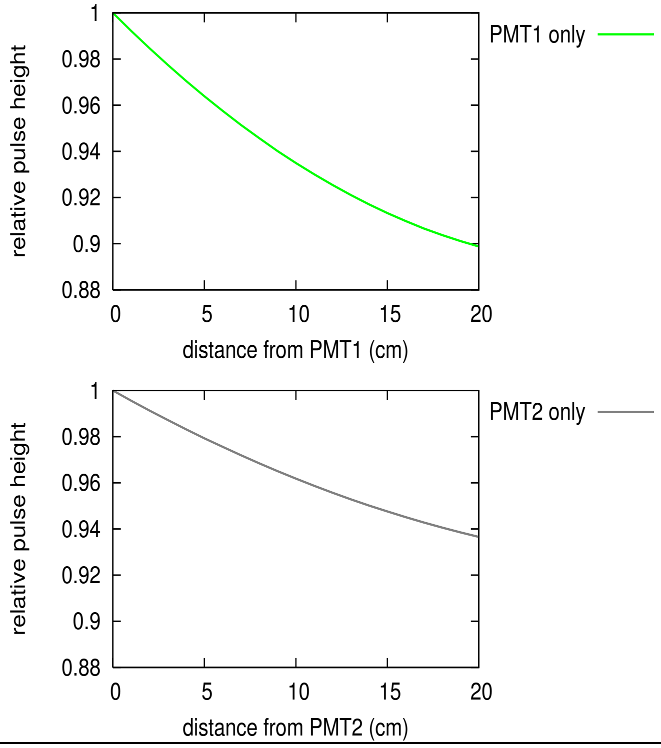

FIGURE 3.13: Position dependence of the relative pulse height; **Top**: PMT1 signals, measured with increasing distance from PMT1; **Bottom**: PMT2 signals, measured with increasing distance from PMT2; the x-axis indicates distance of each measurement from the PMTs along the diagonal of the crystal.

3.5.2 Spectral characterization of the crystal

Using three different radioactive sources ^{241}Am (59.5 keV), ^{133}Ba (30.97 keV, 81 keV and 356 keV), and ^{57}Co (122.1 keV), the ACD was characterized at the operating voltage of 690 V to determine the following

1. variation of the peak pulse height channel as a function of energy, for different locations on the crystal
2. variation of the spectral width parameter, σ with energy, for different locations on the crystal

The locations on the crystal surface where measurements were made are shown in the fig(3.12).

Each photon source was a thin film of radioactive material spread as a disk of size 7 mm in a plastic case of diameter 25 mm, and thickness 3 mm. This source was placed in a cylindrical lead source holder of diameter and height 25 mm, with a thickness of 2 mm. The opening angle for photons impinging on the surface of the crystal is 90°. The output of the CSPA circuit was connected to an ADC-MCA circuit box, which digitized the pulses and created pulse height spectra that could be displayed and recorded on a computer.

At each location, the detector was calibrated to get the position-dependent energy-to-channel conversion equations, and the relation between σ and energy. An x-y coordinate system was defined at the detector surface with origin at the centre of the detector plane (position E). The positions D-F lie on the y-axis, while B-H lie on the x-axis. Therefore, each photon that interacts in the crystal has an (x, y, z) coordinate; the z-axis lies along the thickness of the crystal, with z=0 corresponding to the top of the crystal.

The table(3.1) lists the experimentally measured peak channel number and σ in units channels, for the 59.5 keV and 122.1 keV γ-ray lines for three different locations; G near a PMT, I that is behind both PMTs and represents a larger distance within the crystal that the scintillation photons have to traverse to reach the PMTs (as seen in fig(3.12)), and E which is at the centre of the crystal and under the influence of both PMTs. Looking at the numbers, one can see that the light collection is maximum at G which is near the PMT and minimum at the location I which is farthest from the tubes. The experimentally measured pulse height spectra at the three locations G, E, and I for 59.5 keV and 122.1 keV γ-rays are shown in figures (3.14) and (3.15) respectively.

For each of the 13 locations marked in fig(3.12), the peak channel and σ parameter were measured for the photon sources available in the laboratory.

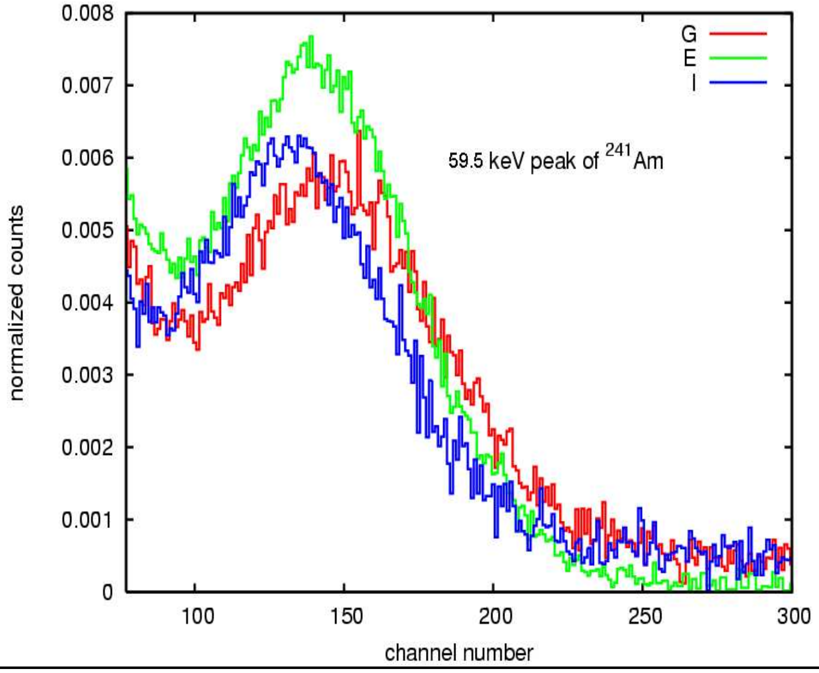

FIGURE 3.14: ^{241}Am pulse height spectra measured with the CsI detector at the locations G (near PMT1), E (at the centre of the crystal) and at I (behind both the PMTs). The x-axis is in units of channel number, while the y-axis is in units of normalized counts.

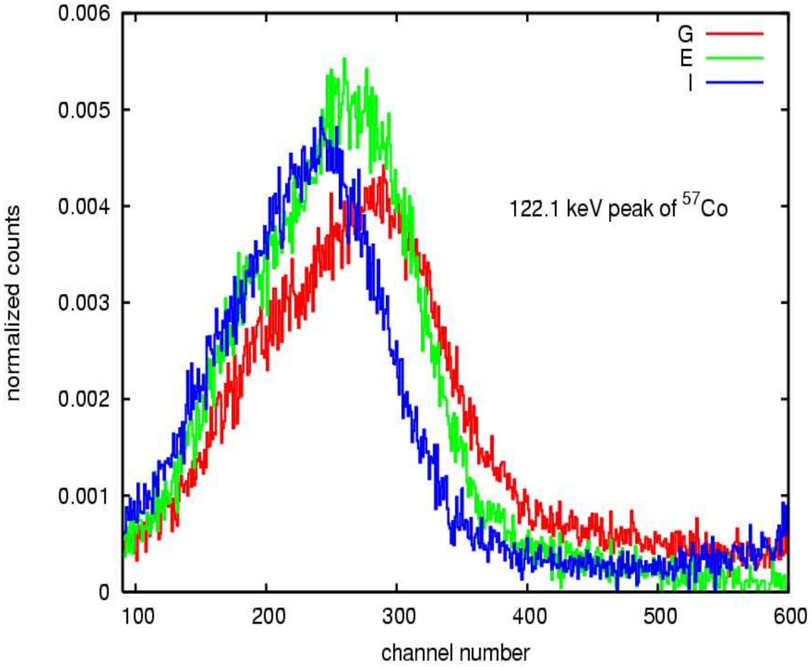

FIGURE 3.15: ^{57}Co pulse height spectra measured with the CsI detector at the locations G (near PMT1), E (at the centre of the crystal) and at I (behind both the PMTs). The x-axis is in units of channel number, while the y-axis is in units of normalized counts.

	Peak channel		σ (chan)	
location	59.5 keV	122.1 keV	59.5 keV	122.1 keV
G	145±0.8	281±1	38±2	61±2
E	140±0.5	265±1	34±0.8	55±3
I	132±0.6	241±1	33±1	50±2

TABLE 3.1: Comparison of the peak channel and spectral width parameter (in channel) of different spectral lines as a function of position with respect to the PMT

One of the aims of the spectral characterization was to provide enough input so as to render the simulation of the CsI(Tl) detector spectral response as close to the experimental response as possible. The instrumentation of the ACD was designed for linearity up to 250 keV. Since the 356 keV peak of ^{133}Ba falls outside this range, its response as measured by the ACD shows non-linear behavior.

Consider the plot in fig(3.16) which represents the peak channels of the 30.97 keV, 59.5 keV, 81 keV, 122.1 keV and 356 keV peaks as a function of energy, measured at position C on the crystal. This plot is representative of similar data for the other positions on the crystal. In the plot, the dashed line represents the linear channel-energy conversion model for all energies excluding 356 keV, while the solid line represents the model which included 356 keV. The measured peak channel of 356 keV is apparently smaller in value compared to what it would have been if the system linearity was extended to higher values. For the channel-energy relation, the linear model is given by a simple straight line equation, while the non-linear model is written as a second degree polynomial, given by equations (3.14) (3.15), respectively.

$$\text{Chan} = ch_{a_l} E + ch_{b_l} \tag{3.14}$$

$$\text{Chan} = ch_{a_{nl}} E^2 + ch_{b_{nl}} E + ch_{c_{nl}} \tag{3.15}$$

Here, ch_{a_l} and ch_{b_l} are the free parameters of the linear model, while $ch_{a_{nl}}$, $ch_{b_{nl}}$ and $ch_{c_{nl}}$ are the free parameters of the non-linear model and E is the energy in keV. The exact energy at which turn-over from linearity to non-linearity occurs was not accurately known due to lack of radioactive sources that covered the energy range up to 250 keV. The location of this turn-over point could have been found using a pulser, but this was not done for this experiment due to certain constraints.

Similarly, the plot in fig(3.17) shows σ (keV) plotted against energy for the 30.97 keV, 59.5 keV, 122.1 keV and 356 keV γ-rays measured at position C on the crystal. This plot is representative of similar measurements conducted on the crystal at other positions. The data points excluding that corresponding to 356 keV were fit with an equation given

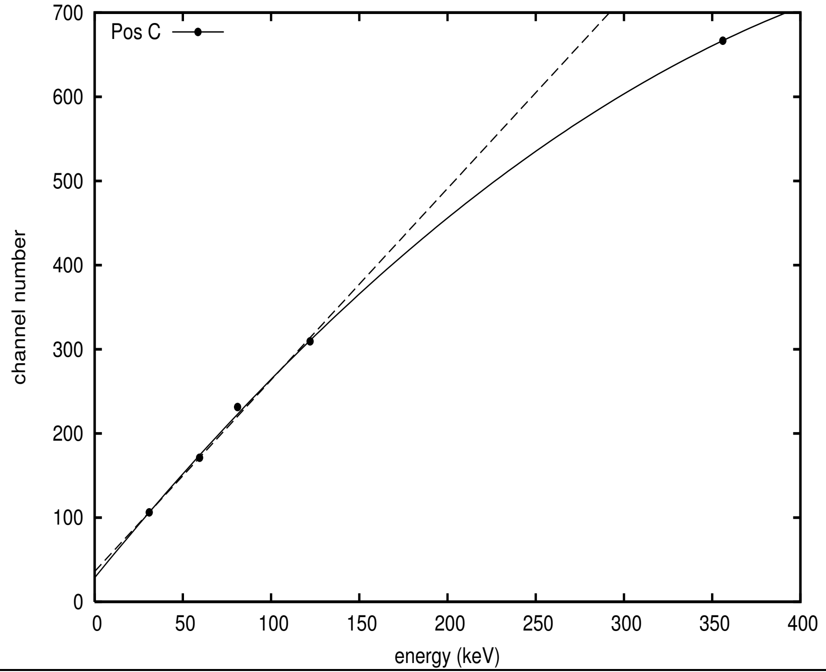

FIGURE 3.16: Channel-energy calibration plot of the CsI(Tl) ACD at position C. The closed circles represent the peak channels of the 30.97 keV, 59.5 keV, 81 keV, 122.1 keV, and 356 keV peaks as a function of energy, the error bars are smaller than the symbols and so are not visible in the plot; the dashed line is the linear channel-energy model while the solid line is the non-linear model, which represents the data better.

by

$$\sigma = \sqrt{\mathrm{A}E + \mathrm{B}} \tag{3.16}$$

which is derived from eqn(1.10) where 'A' represents the product of the Fano factor and w (the minimum energy required to produce one charge carrier pair in the detector system) in units keV and 'B' is the consolidated noise factor written in terms of $(\mathrm{keV})^2$. This model is represented by the dashed line in fig(3.17). As can be seen from the plot, the spectral width of 356 keV is smaller than what it should have been if it followed the relation represented in eqn(3.16). In order to accommodate this non-linear behavior, the σ-energy data have been fit using a simple quadratic model by the eqn(3.17)

$$\sigma = \sigma_a E^2 + \sigma_b E + \sigma_c \tag{3.17}$$

where σ_a, σ_b, and σ_c are the free parameters of the equation, and E is the energy in keV.

For each (x,y) marked on the crystal surface the channel-energy data were fit using eqn(3.15) and the best fit values for each (x,y), $\mathrm{ch}_{a_{x,y}}$, $\mathrm{ch}_{b_{x,y}}$, and $\mathrm{ch}_{c_{x,y}}$ were obtained.

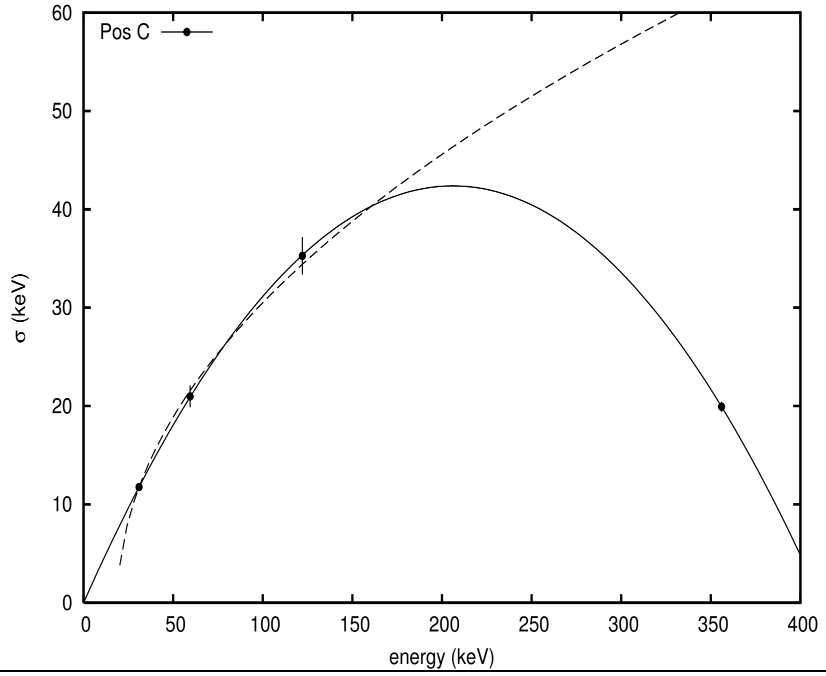

FIGURE 3.17: Plot of σ (keV) as a function of energy of the CsI(Tl) ACD at position C. The closed circles represent the σ values at 30.97 keV, 59.5 keV, 122.1 keV, and 356 keV; the dashed line is the model given by eqn(3.16), while the solid line is the non-linear model, which represents the data better.

Similarly for σ-energy, data at each position were fit using eqn(3.17) to get the best fit parameters $\sigma_{a_{x,y}}$, $\sigma_{b_{x,y}}$, and $\sigma_{c_{x,y}}$. These best fit coefficients were then parameterized with respect to (x,y), i.e. they can be written as functions of (x,y)

$$\begin{aligned} ch_{a_{x,y}} &= f_1(x,y) \qquad & ch_{b_{x,y}} &= f_2(x,y) \qquad & ch_{c_{x,y}} &= f_3(x,y) \\ \sigma_{a_{x,y}} &= g_1(x,y) \qquad & \sigma_{b_{x,y}} &= g_2(x,y) \qquad & \sigma_{c_{x,y}} &= g_3(x,y) \end{aligned}$$

so that one can determine the values of these coefficients for any (x,y). These can then be used in eqn(3.15) and eqn(3.17) to find the position dependent channel-energy and σ-energy relations, respectively. This approach has been outlined as follows:

1. Referring to the coordinate system described above, the surface of the crystal was divided into 13 locations for calibration.
2. Each location was given an (x,y) coordinate in cm, as listed in table(3.2).
3. Spectra of ^{241}Am, ^{133}Ba and ^{57}Co were measured at each location, and the peaks corresponding to the γ-ray lines were fitted with Gaussian functions in order to determine the peak channel and the width of the peak.

4. For the sake of simplicity, the opening angle of the radioactive source was neglected, and it was assumed that the spectra were measured at positions that correspond to the (x,y) coordinates given in table(3.2).

location	(x,y) coordinate in cm
G	(-5.3,5.3)
D	(0,5.3)
A	(5.3,5.3)
L	(-2.62,2.62)
J	(2.62,2,62)
H	(-5.3,0)
E	(0,0)
B	(5.3,0)
M	(-2.62,-2.62)
K	(2.62,-2.62)
I	(-5.3,-5.3)
F	(0,-5.3)
C	(5.3,-5.3)

Table 3.2: (x,y) co-ordinates of the locations on the crystal surface used for calibration

5. Second degree polynomials were used to determine channel-energy and σ-energy relationships for each location

$$ch(x,y) = ch_{a_{x,y}}E^2 + ch_{b_{x,y}}E + ch_{c_{x,y}} \tag{3.18}$$

$$\sigma(x,y) = \sigma_{a_{x,y}}E^2 + \sigma_{b_{x,y}}E + \sigma_{c_{x,y}} \tag{3.19}$$

   Thus, for each of the 13 positions, one gets three coefficients corresponding to the channel-energy relation, and three coefficients for the σ-energy relation. The aim at this point was to derive a position dependency for each of the six coefficients; i.e. to fit each of them as a function of the (x,y) position on the crystal.

6. The coefficients $ch_{a_{x,y}}$, $ch_{b_{x,y}}$, $ch_{c_{x,y}}$, $\sigma_{a_{x,y}}$, $\sigma_{b_{x,y}}$, and $\sigma_{c_{x,y}}$ were interpolated as a function of (x,y) with a finer granularity, and were then individually fit as functions

of (x,y) to get the following equations

$$\begin{aligned}
ch_{a_{x,y}} &= \frac{-0.136 + y}{(-0.124 \times 10^5) - (0.150 \times 10^4 x)} - (0.6963 \times 10^{-3}) && (3.20)\\
ch_{b_{x,y}} &= \frac{(0.527 \times 10^2) + y}{(0.26 \times 10^2) + 1.135x} + 0.103x && (3.21)\\
ch_{c_{x,y}} &= 0.9\exp(-0.173x + 0.0468y^2) + (0.168 \times 10^2) && (3.22)\\
\sigma_{a_{x,y}} &= \frac{0.8393 + y}{(-0.1193 \times 10^4) + 2.855x^2} + (0.874 \times 10^{-3})y && (3.23)\\
\sigma_{b_{x,y}} &= \frac{0.6751 + y}{2.398 - (0.4453 \times 10^{-2})x^2} - 0.4304y && (3.24)\\
\sigma_{c_{x,y}} &= \frac{-0.356 + y}{(-0.852 \times 10^{-1}) + (0.195 \times 10^{-3})x^2} + (0.1225 \times 10^2)y && (3.25)
\end{aligned}$$

7. Thus, the above equations are the surface models of the coefficients $ch_{a_{x,y}}$, $ch_{b_{x,y}}$ and $ch_{c_{x,y}}$ of the channel-energy relation and $\sigma_{a_{x,y}}$, $\sigma_{b_{x,y}}$ and $\sigma_{c_{x,y}}$ of the σ-energy relations respectively.

In this way, spectral characterization of the detector was performed and the response of the ACD was parameterized as functions of energy and position. These relations were then used in a Geant4 application to simulate pulse height spectra of the detector. The methods used to model the ACD response is discussed in the next section.

3.6 Simulation of the ACD response at room temperature

The main aim of the ACD is Compton suppression of the CZT detector signals. The output of the HEX ACD in flight configuration are the counts recorded in four broad band windows. The low and high energy limits of each window are 30-100 keV, 100-170 keV, 170-250 keV, and >250 keV at room temperature. During operation of the CZT detector

1. the counts in individual windows are recorded

2. one window is selected for vetoing events in the CZT - the CZT event is flagged, indicating that a veto event has occurred and it needs to be rejected from the spectrum. The choice of the window for vetoing is command selectable.

It is important to simulate the veto action of the ACD as accurately as possible. The veto efficiency of different windows can be studied for different background conditions of the spacecraft in lunar orbit; one can then use these predictions to pre-select windows for efficient CZT background rejection. The simulation can be used to determine the total background seen by the detector, after applying veto action of the ACD in the region of interest. The following steps were followed in order to achieve this:

1. The ACD response was simulated at the detector level. The simulation was then validated against experimentally measured pulse height spectra, with emphasis placed on reproducing peak channel and σ, as well as the normalized peak intensity and area under the curve.
2. Once the simulated pulse height spectra were validated, the next stage of the simulation could be performed with confidence, which is modeling the ACD four window counts. These simulated counts were then be validated against the ones measured in the laboratory at room temperature.

3.6.1 Detector Level Simulation

A Geant4 application was designed to model the CsI(Tl) detector response. In addition to including the parameterization of the spectral parameters as function of (x,y) and energy, it was necessary to model the detector geometry as close as possible to the real case with all the appropriate materials. The HEX ACD geometry consists of the following components

1. Aluminum housing which contains CsI(Tl) crystal (14 cm × 14 cm ×1 cm), perspex below the crystal (14 cm × 14 cm × 1.5 cm), and two side mounted PMTs of 2.5 cm diameter each. The PMTs that were available were larger in diameter than the area of the crystal surface that they would be viewing; so the perspex was used below the crystal as a light guide
2. flanges outside the Aluminum housing for mounting the ACD tray
3. 0.3 mm thick Aluminum window placed above the crystal
4. 1 mm thick Aluminum top plate with a cut-out to house the window, and for ESD and mechanical protection.

For the simulation, the entire geometry except the PMTs were modeled. The components of the Geant4 detector geometry are shown in figures (3.18), (3.19), and (3.20).

Radioactive source holders were modeled with appropriate materials according to the specifications mentioned earlier and GSPM was used to simulate the radioactive source. The photons emerging from the radioactive source were given an isotropic angular distribution within a 90° opening angle as mentioned in section 3.5.2. Provisions were

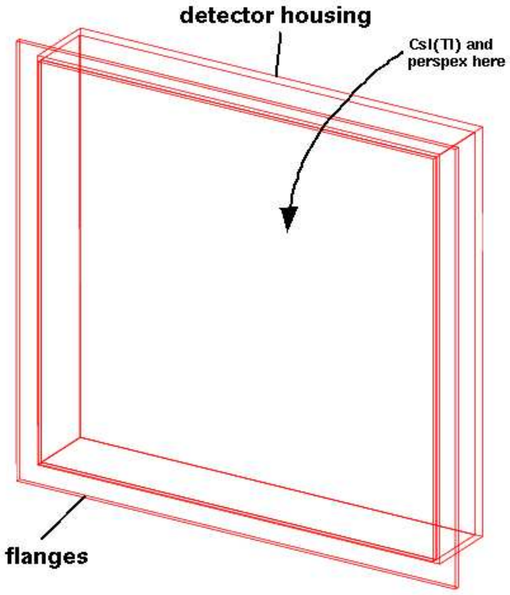

FIGURE 3.18: Wire module of the detector housing showing where the CsI(Tl) crystal and perspex are mounted

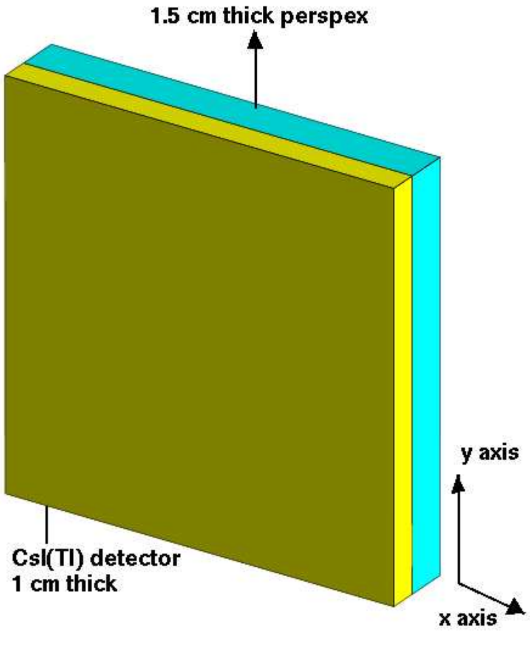

FIGURE 3.19: CsI detector and the perspex mounted one below the other

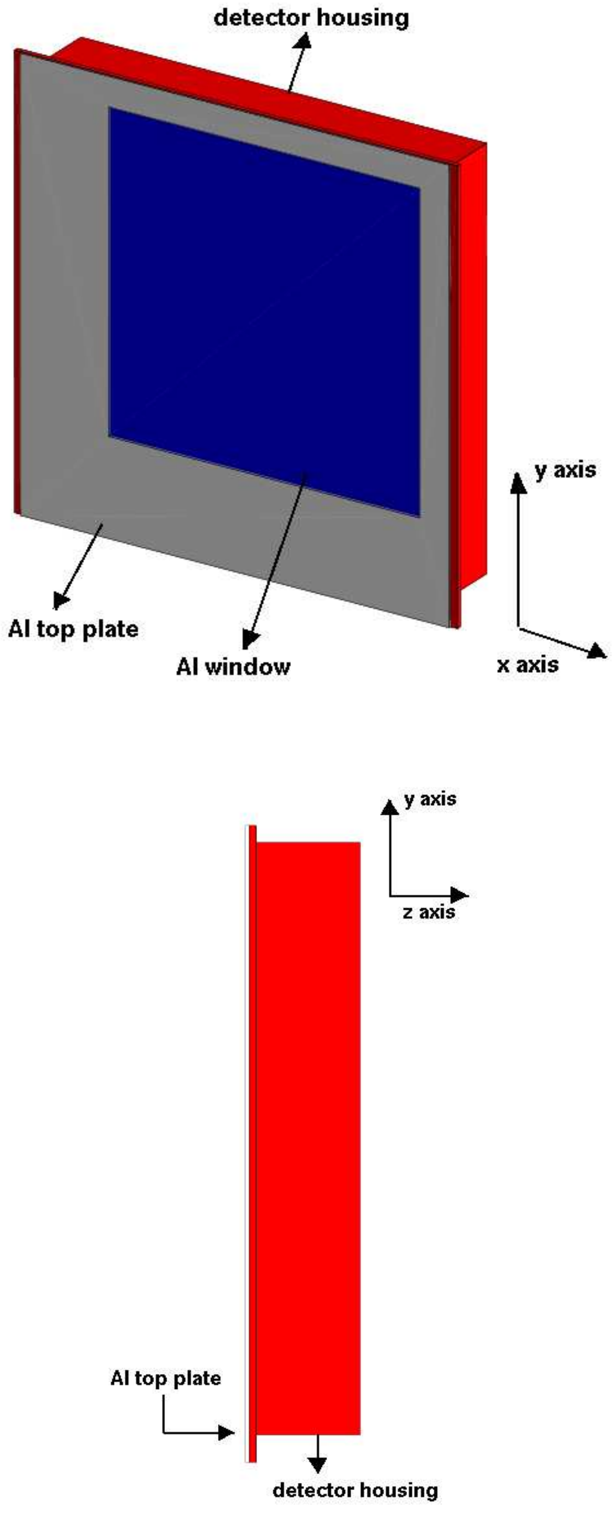

FIGURE 3.20: **Top** : Isometric view of the CsI(Tl) ACD detector geometry as modeled in Geant4, the Aluminum top plate, Aluminum window, and part of the detector housing are seen in this view; **Bottom** : Side view of the CsI(Tl) ACD, showing the housing

made in the application to move the radioactive source to any location over the detector surface.

The physics used in the simulation is listed in table 2.3 and includes all the low energy electromagnetic processes for photons, electrons and positrons, and physics to simulate radioactivity.

The detector was made *sensitive*. The energy deposited in the ACD and the (x,y) coordinate of the interaction were obtained by extracting the *hits* information in the *UserEventAction* class using the object of the *G4HCofThisEvent* class. The equations (3.18) through (3.25) were used in the *UserEventAction* class to compute the channel number and the spectral width parameter for the local energy deposit at every (x,y) position of interaction.

For each radioactive source the simulation was run for 10^6 events. This was repeated for each position on the crystal. The simulation results were channel numbers which were extracted from the *UserEventAction* class. These were then binned from 0-1023 with a bin size of one channel to create a pulse height spectrum of the deposited energy. The figures (3.21) and (3.22) compare the simulated and measured pulse height spectra for ^{133}Ba and ^{57}Co respectively, for the sources placed at location E on the detector. The y-axis is in units of normalized counts, which is the counts in each bin divided by total counts under the curve.

From these spectral results, one can make the following conclusions:

1. ^{133}Ba spectra -
   The 30.97 keV and 81 keV peaks of the simulated ^{133}Ba spectrum match very well with those in the measured spectrum in terms of peak channel, normalization, and spectral width, within experimental errors. However, the same cannot be said about the 356 keV peak. As can be seen, the simulated response underestimates the normalization and shows a left shift in the peak channel. Observing the spectrum carefully, one can see that there are excess counts on the low energy side of the simulated 356 keV peak which can explain the missing counts under the 356 keV photopeak. It appears that it was not possible to reproduce the 356 keV photopeak despite including non-linear terms into the model. This shows that we have not completely understood the high energy response of the ACD, which was not as simple as a quadratic equation and could be due to a combination of non-linearity and saturation due to pile-up. However, this anomaly in the high energy response is not critical for the flight instrument mainly because in the flight instrument, all events that deposit energy >250 keV are binned into one counter (detailed ACD pulse height spectra are not saved onboard).

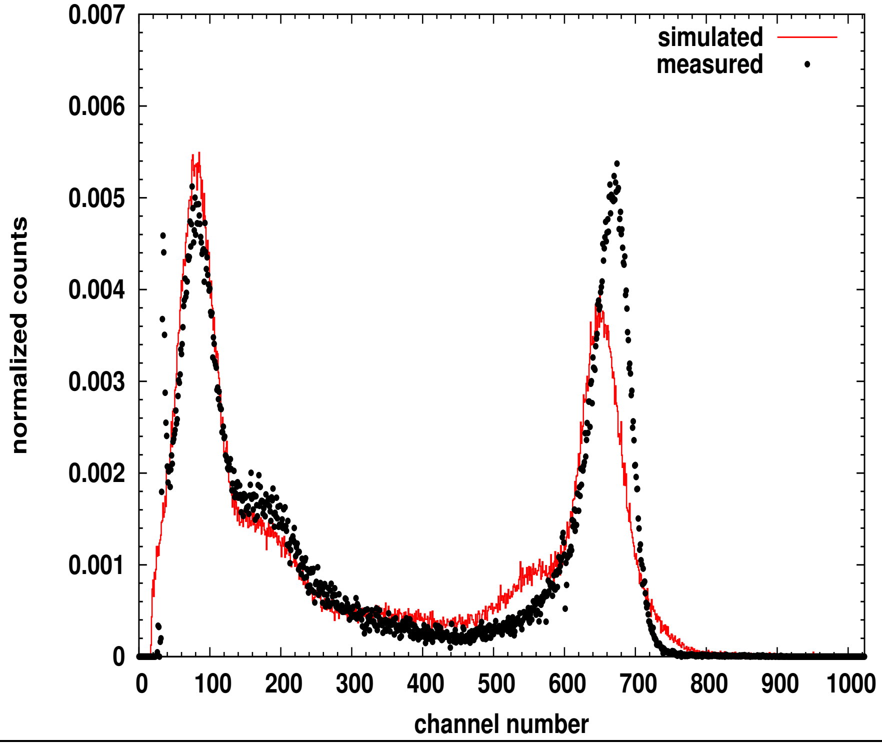

FIGURE 3.21: Comparison between the simulated and measured ^{133}Ba spectra at position E on the CsI(Tl) ACD

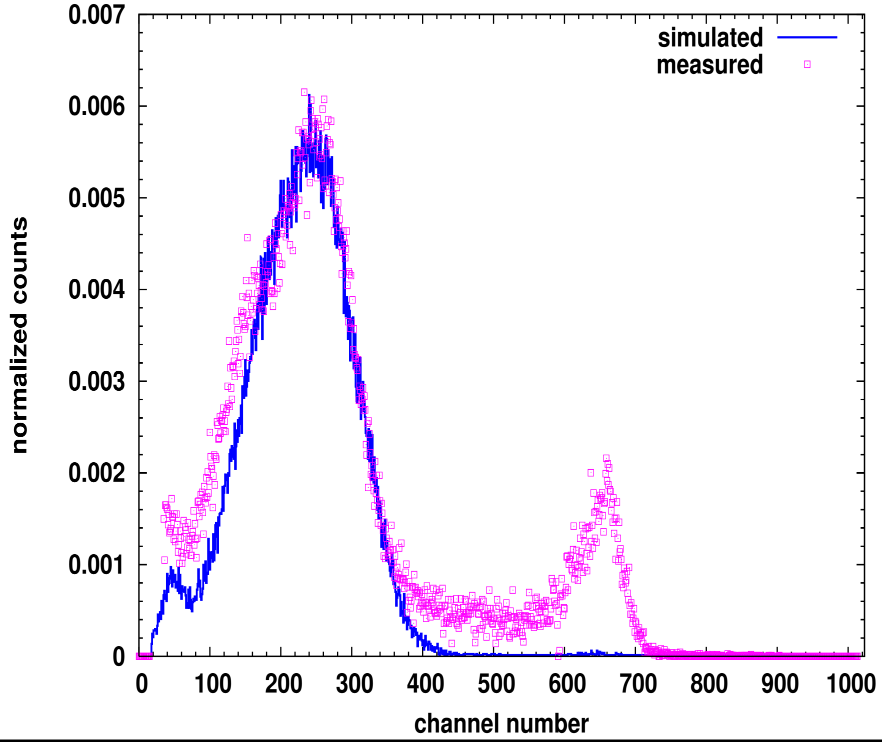

FIGURE 3.22: Comparison between the simulated and measured ^{57}Co spectra at position E on the CsI(Tl) ACD

2. ^{57}Co -

   The simulated 122.1 keV pulse height spectrum matches very well with the one in the measured spectrum with respect to peak channel, normalization, and spectral width, within experimental errors. The excess counts that form a "hump" on the low energy side of the experimental 122.1 keV peak is an artifact of the detector-source geometry that was not modeled into the Geant4 application. The peak-like structure in the measured spectrum around ∼660 channel, is due to saturated high energy counts.

From these observations one can conclude that the CsI ACD response has been successfully modeled using Monte Carlo simulation and this application can be used to model the veto capability of the system.

3.6.2 Package level simulation

Figure (3.23) shows a cross section of the HEX package as modeled using Geant4. The mechanical configuration of the HEX payload was discussed in section 1.2. As can be seen in the figure, all the trays were modeled with appropriate dimensions using the material AZ31BH24, which is a Magnesium alloy with 3% Zinc. In tray 1, the stainless steel collimator of HEX is marked in red, modeled according to the final dimensions. In tray 2 marked in blue, is the CZT array; all nine crystals were modeled, including the ASICs bonded to the rear side, the side-mounted printed circuit board (PCB), and the copper thermal contacts. In tray 3 one can see the CsI ACD and the perspex light guide below it in green and purple respectively. The collimator and all the trays were constructed using the boolean solids functionality to make cut-outs. The approximation made at this stage of the modeling is that none of the electronic components, PMTs and PCBs, except the CZT mother board, were modeled. In short, the modeled geometry of the package contains

- Stainless steel collimator in tray 1, made of Magnesium alloy AZ31BH24
- Tray 2 with the nine CZT detectors; each with two ASICs made of Silicon, PCB, brass heat sinks, copper heat sinks, PCB mother board, and copper plate.
- Tray 3 with the CsI ACD and housing module (as described in section 3.6.1)
- Trays 4, 5, and 6

As discussed in the previous section, the methodology used for simulating the CsI ACD response was successful in reproducing experimentally measured spectra for different

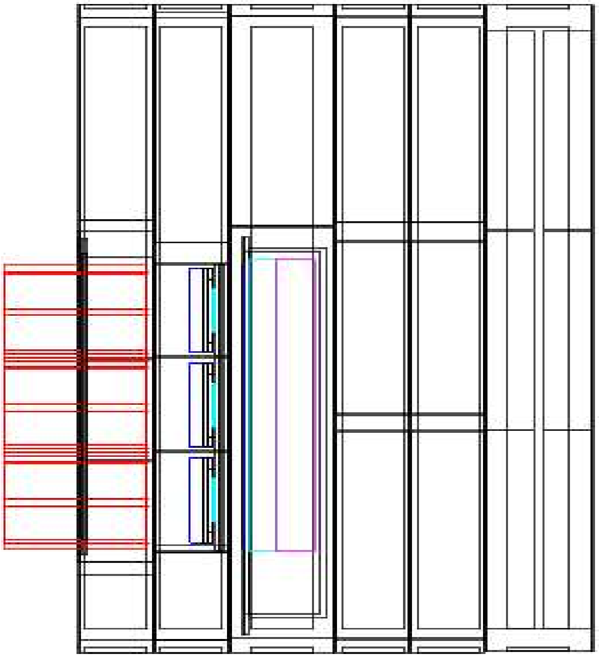

FIGURE 3.23: Geant4 HEX package model: a cross section

photon energies as a function of position on the crystal. The next stage was to simulate the results of the laboratory characterization of the ACD in the full HEX package configuration, which are the counts in each of the four window counters. The reason the ^{133}Ba radioactive source was used for the laboratory characterization of the ACD in order to exploit the presence of high energy γ-rays that can penetrate the stainless steel collimator, the CZT detector arrays and its associated components to reach the ACD.

During the laboratory experiment, the ^{133}Ba source was placed at a height of 20 cm from the top of the collimator and counts in each ACD window were measured and stored using the HEX flight electronics. For purposes of cross-verification, a PHA was connected in parallel with the flight electronics to measure the pulse height spectrum of the source. This spectrum was then divided into four broad bands based on the following pulse height to channel calibration

- Win0 ranges from 470 mV to 1.972, which corresponds to channels 66 through 208 in the PHA.

- Win1 ranges from 1.972 V to 3.464 V, which corresponds to channels 208 through 349 in the PHA.
- Win2 ranges from 3.464 V to 5.24 V, which corresponds to channels 349 through 520 in the PHA.
- Win3 ranges from 5.24 V to 14.763 V, which corresponds to channels 520 through 1023 in the PHA.

The count rate measured with the four ACD windows were then validated against those measured by the PHA broad bands and showed good consistency within errors.

In order to simulate these counts, the experimental setup was modeled maintaining the source-detector geometry and including the CsI detector response. The simulation was executed for 10^7 events. In the *UserEventAction* class, the logic representing the four window counters was included with $\mathrm{E0}_{W0}$ to $\mathrm{E1}_{W0}$, $\mathrm{E0}_{W1}$ to $\mathrm{E1}_{W1}$, $\mathrm{E0}_{W2}$ to $\mathrm{E1}_{W2}$ and $\mathrm{E0}_{W3}$ to $\mathrm{E1}_{W3}$ representing the boundaries of the first, second, third and fourth window counters, respectively. If an event has energy such that it lies between any of the window boundaries, that counter is incremented. In this way, the simulated counts registered by the ACD are written out into four corresponding files and normalized with respect to the total number of counts in all windows.

In order to facilitate validation of the simulated ACD four window counts against experimental measurements, the observations were also normalized with respect to the total counts in each window. The results are summarized in the table(3.3)

Source	Win1	Win2	Win3	Win4
Experimental	0.1603	0.1722	0.1644	0.4488
Simulated	0.1315	0.1872	0.2134	0.4292

Table 3.3: Table summarizing the results of the simulation of the ACD response in the stacked condition. The numbers in each column are the counts in each window normalized with respect to the total counts across the 4 windows

A **t-test** hypothesis test, was performed in **Matlab** to compare the results of the simulation with the experiment. The test is used to compare two small sets of data which are produced independent of each other. The null hypothesis was defined such that the experimentally measured probability in each window and the simulated ones are derived from the same distribution, and are in effect equal. The **p-value** of the t-test, or the probability of observing the given result, assuming the null hypothesis is true, was computed to be **0.969** for a significance level of 0.05 or 5%. This implies that the differences between the two data sets are not significant at the 5% level and that the data sets are equal.

From these results it can be seen that the response of the four window counters of the HEX ACD can be successfully simulated, within experimental errors. The significance of the reproducibility of experimental results is that the user is empowered with confidence in the modeling methodology. This simulation can be used in a variety of applications, a few being

- simulation of the CZT detector spectrum when each of the ACD windows are separately activated, in order to study the effect of each region of the energy deposited in the ACD on background rejection in the CZT spectrum
- plotting a coarse four channel spectrum of the CsI detector for different environmental conditions in space, so as to enable the study of its temporal evolution, most importantly in the event of the occurrence of highly energetic phenomena, such as solar flares, Coronal Mass Ejections (CMEs) or gamma-ray bursts

3.7 Summary and Conclusions

1. The signal generation process in scintillation detectors was studied. The basic principles of anti-coincidence techniques and the different methods by which this logic can be applied were also discussed.
2. Geant4 was demonstrated as a very useful tool for detector geometry optimization. Using the simulation results, the design of the HEX ACD geometry was modified so as to balance both the scientific requirements of the total system and the weight and space restrictions demanded by the spacecraft.
3. Simulated ACD response at the detector level was validated satisfactorily against the experimentally measured response. Spectral characterization of the ACD in full payload configuration was carried out. The CsI detector was subjected to a systematic experimental investigation to determine its response and the characterization yielded spectral parameters such as the pulse height channel and σ, as functions of energy and position. These quantities were then parameterized as functions of position and energy, using two-dimensional interpolation and fitting techniques.
   The package level ACD response was simulated, including as much detail in the geometry modeling as possible. Using the validated ACD response in the application, it was possible to successfully reproduce the experimentally measured ACD four window counts.
4. The four window counter of the ACD can give a coarse spectrum, and studying its evolution with time could give some information about energetic events. This can

be simulated with Geant4 using the known detector response in order to study the significance of such events in the broad band spectrum.

Bibliography

[1c] Chauvie, S. et al., *Geant4 Low Energy Electromagnetic Physics*, in Proc. Computing in High Energy and Nuclear Physics, Beijing, China, pp 337-340, 2001

[2c] Chauvie, S. et al., *Geant4 Low Energy Electromagnetic Physics*, in Proc. IEEE Nuclear Science Symposium Conference Records, N33-165, 2004

[3c] Ivanchenko, V. N et al., *Geant4 standard electromagnetic package for HEP applications* in Proc. IEEE Nuclear Science Symposium Conference Records, N33-179, 2004

Chapter 4

Simulation of the HEX CdZnTe detector spectral response

The focus of this chapter is on simulation of the spectral response of the HEX CdZnTe detector. One of the nine detectors was chosen, characterized, and various experimental parameters were extracted. These were used as input to a Geant4 application developed to simulate the CdZnTe response, so as to reproduce the experimental results. This gives confidence in extraction of spectral parameters and in the methodology of the detector response simulation.

The primary detector of the HEX payload is composed of the compound semiconductor Cadmium-Zinc-Telluride ($Cd_{1-x}Zn_xTe$, x = 0.1). Compound semiconductors are characterized by a larger fraction of impurities and dislocations relative to silicon and germanium semiconductors, which are byproducts of the crystal growth technique. These impurities and dislocations in compound semiconductors act as charge carrier trapping sites. Loss of charge produced by incident ionizing radiation produces a visible distortion of the pulse height spectrum.

HEX is a spectroscopic instrument developed to measure the intensity of various γ-rays from the moon in the 30-270 keV range. In x-ray spectroscopy, the photon spectrum is measured in terms of counts as a function of channel numbers. This measured spectrum is related to the source spectrum by the **response matrix**, R(i,E)

$$C(i) = \int_0^E f(E)R(i,E)dE \tag{4.1}$$

where

C(i) is the total number of counts measured in channel 'i', f(E) is the incident source spectrum, which is to be determined, and R(i,E) is the instrumental response. It provides the probability that an incident photon of energy E will be detected in a channel 'i' of the ADC.

The instrumental response is a continuous function of energy, measured over a discrete number of channels. It can therefore be converted to a discrete response matrix $R_{i,j}$ at discrete values of energy E_j. In a **response matrix**, the incident energy E is *redistributed* across a set of channels. In order to determine the incident source and derive its parameters, a source model M(E) which best represents the characteristics of the incident photon source, is chosen and convolved with the instrument response to predict the observed spectrum corresponding to M(E). The predicted spectrum is then compared with the experimentally observed data; a 'goodness of fit' criteria is used to tune the parameters of the source model M(E), and finally the parameters that provides the optimum fit to the observed data is said to best represent the source.

The response matrix is the product of two components

$$R_{i,j} = R_D(i,j)A(E_j) \tag{4.2}$$

where

R_D(i,j) is the **spectral redistribution function (SRF)**, and is described as the probability that a photon of energy E_j is detected in a channel 'i'; A(E_j) is the total effective area in cm^2 which is the product of the detector geometric area and efficiency, ϵ(E). Thus, the unit of the response matrix is cm^2.

From the point of view of the HEX experiment it is necessary to construct the CZT detector response matrix. One of the initial steps involved towards this is to generate the SRF for all energies within the 30-270 keV range. This can in principle be achieved experimentally. However, practical constraints like unavailability of sources that cover the energy region of interest or infrastructure to conduct an extensive system calibration often prevents the experimental determination of the SRF across the full energy range.

Geant4 is an excellent tool for generation of detector SRF, because it takes into account all the physical processes of particle interaction with matter. It can be used to model the detector geometry as accurately as possible, with appropriate materials and dimensions, and irradiate with different radiation sources, either monoenergetic or any continuum.

This chapter focuses on the methodology for generation of the HEX primary detector SRF. First, experimentally measured spectral parameters are extracted from laboratory detector calibration data. These are then parameterized and used in an application to simulate the detector response.

The following section discusses the principle of pulse formation in semiconductor detectors, and will then we consider the factors that affect the shape of spectra produced by Cadmium-Zinc-Telluride detectors. This is important as understanding the structure of the measured spectra is essential in modeling the detector response.

4.1 Pulse Formation in Semiconductor Detectors

When a p-n junction is formed, majority carriers on either side of the junction diffuse into regions of lower concentration, forming a depletion region or junction with a contact potential which is due to a build up of space charge. This space charge arises from the immobile ions left behind when the majority charge carriers migrate.

When this junction is reverse biased (refer fig(4.1)), the flow of majority carriers across the junction is stopped. This is because, in addition to the contact potential, all the applied bias appears across the junction, creating a potential barrier that the diffusing electrons and holes cannot overcome. Thus, a high resistance is created for majority carriers across the junction. However, there is a small current across the junction due to the motion of minority carriers. Since application of a reverse bias increases the overall potential, there should be a corresponding increase in space charge and an extension of the depletion region into the p and n regions of the detector.

The total depletion region is therefore that region over which the space charge extends, which increases with the applied bias potential. Electron-hole pairs produced by ionizing radiation in the depletion region are swept towards their respective electrodes by this electric field. Semiconductors operated in the reverse bias mode are therefore used as radiation detectors.

Sensitivity requirements of radiation detectors demand interaction of incident particles in as large a volume as possible, so the greatest possible depletion depth is necessary.

The depletion width, d', is given by the equation

$$d = \sqrt{2\,\epsilon\,V_0\,\mu\,\rho_{d'}} \tag{4.3}$$

where μ is the mobility of the majority carrier of the region with lower dopant concentration; V_0 is the applied voltage; ϵ is the dielectric constant; $\rho_{d'}$ is the resistivity of the depletion region in (Ω-cm).

The depletion region has an inherent capacitance associated with it, which can be expressed in terms of capacitance per unit area

$$C_a = \frac{\epsilon}{d'} = \sqrt{\frac{e\epsilon N}{2V_0}} \tag{4.4}$$

where N is the dopant concentration of that side of the junction with the lower dopant concentration. Therefore, increasing the depletion width also decreases the capacitance, improving the noise quality of the system. A completely depleted detector is one in which the depletion region extends into the complete thickness of the detector, d, and this happens for a particular value of bias voltage, V_d. In this condition, the electric field ε, in the depletion region is uniform and planar and is given by V_d/d.

As discussed above, charge carrier pairs generated by ionizing radiation are swept to their respective electrodes by the electric field, and this occurs with a **drift velocity**

$$\begin{aligned} v_e &= \mu_e \varepsilon \\ v_h &= \mu_h \varepsilon \end{aligned} \tag{4.5}$$

These drifting charges give rise to induced charge on electrodes, which cause the bias voltage across the depletion region to reduce. A voltage appears across the load resistor of the external circuit which is equal to the amount by which depletion region voltage dropped. This voltage constitutes the basic signal, and it reaches a maximum when all the charges have been collected. It then returns to equilibrium depending on the time constant of the external circuit.

The amplitude of the voltage signal is proportional to the charge created by the ionizing radiation. Figure(4.1) shows a schematic of a semiconductor (SC) detector system. This schematic represents the dependence of the shape of the pulse on the location of interaction of the radiation within the depletion region.

For the sake of simplicity, it has been assumed that

- charges have been produced at a single position in the depletion region - there is no distribution of interaction positions
- the detector is completely depleted, with a high and uniform electric field
- there is no **trapping** of charges (this concept will be discussed in the next section)

In order to move from their place of generation, the charge carriers use the energy stored in the detector active volume (depletion region), given by $\frac{1}{2}CV_0^2$, where C is the capacitance of the external circuit and V_0 is the bias voltage. If the point of generation of charge carriers is x_0, then the energy dE, required to move total charge q_0 from there to some point x across a potential difference dV is

$$\begin{aligned} dE &= -q_0 dV \\ \frac{dE}{dx} &= -q_0 \frac{dV}{dx} \\ &= q_0 \varepsilon(x) = q_0 \frac{V_0}{d} \end{aligned} \tag{4.6}$$

where $\varepsilon(x)$ is the electric field at x. Integrating eqn(4.6) from x_0 to x gives the energy absorbed in moving the charge over this distance

$$\Delta E = \frac{q_0 V_0}{d}(x - x_0) \tag{4.7}$$

From this, the signal voltage across the load resistor R and the final collected charge are given by

$$\begin{aligned} V_R &= \frac{\Delta E}{C V_0} = \frac{q_0}{Cd}(x - x_0) \\ Q &= C V_R = \frac{q_0}{d}(x - x_0) \end{aligned} \tag{4.8}$$

As can be seen, the signal voltage and the final collected charge depend on the distance traveled by the charge carriers.

The charge collected as a function of time, Q(t) is dependent on the electron and hole charge collection times t_e and t_h respectively, which in turn depends on the point of interaction in the active volume. This in turn determines the electron drift distance $x_e = v_e t_e$ and the hole drift distance $x_h = v_h t_h$.

$$Q(t) = \frac{q_0}{d} \times (\text{electron drift distance} + \text{hole drift distance}) \tag{4.9}$$

Let the photon interact at a point distance ‘x’ from the anode. Let the electron-hole pairs be created at time t=0. Under the influence of the electric field the electrons drift a total distance x to the anode and the holes drift a total distance (d-x) to the cathode. When $t<t_e$ and $t<t_h$, the charge collection profile is given by

$$\begin{aligned} Q(t) &= q_0 \left(\frac{x_e}{d} + \frac{x_h}{d} \right) \\ &= q_0 \left(\frac{v_e}{d} t + \frac{v_h}{d} t \right) \end{aligned} \tag{4.10}$$

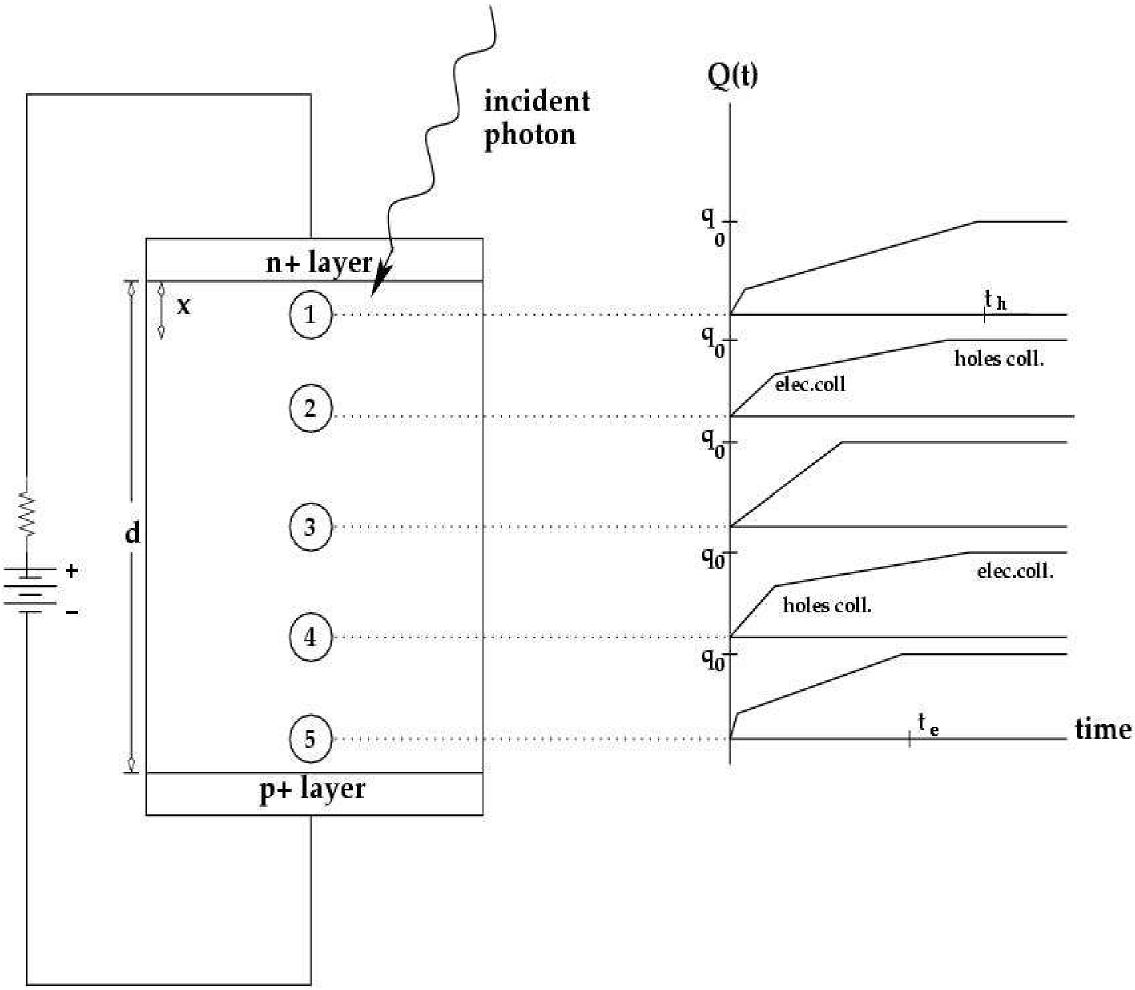

FIGURE 4.1: Schematic of a semiconductor detector (adapted from [4a]) operated in the reverse bias condition. 'd' is the thickness of the detector which is completely depleted, and the direction of photon incidence is shown. The electron-hole pairs are formed in the direction of 'd' and 'x' is an example location of a photon interaction in the active volume (the region between the n^+ and p^+ contacts). The numbering in the active volume indicates five different positions where the photon can interact and produce charge carriers. Along side of the schematic are the shapes of the leading edges of the charge pulses formed due to motion of charge carriers from each of these locations to the electrodes. From this figure, the dependence of the pulse shape on the location of charge production is clearly visible.

Consider two cases

- when the interaction point is close to the anode :- the electrons are collected faster than the holes, which will still be drifting
  For $t_e < t < t_h$
  $$Q(t) = q_0 \left(\frac{x}{d} + \frac{v_h}{d} t \right) \tag{4.11}$$
- when interaction point is close to the cathode :- the holes are collected faster than the electrons, which will still be drifting
  For $t_h < t < t_e$
  $$Q(t) = q_0 \left(\frac{v_e}{d} t + \frac{(d-x)}{d} \right) \tag{4.12}$$

In addition to the shape of the leading edge of the charge pulse, the **amplitude** of the pulse is also affected by the position of interaction of the photon in the detector. This will be discussed in section 4.3.

4.2 CdZnTe Radiation Detectors

Silicon (Si, Z=14) and Germanium (Ge, Z=32) are the most widely used SC materials for radiation detectors. They provide good energy resolution at x-ray and γ-ray energies among all radiation detectors; this is due to their small band gaps (1.12 eV and 0.7 eV for Si and Ge, respectively). They are also excellent for timing studies due to their fast time response. The reasons that these detectors and scintillators are not good choices for hard x-ray spectroscopy in deep space missions are summarized in section 1.1.2.

It is desirable to have a radiation detector with energy resolution better than that of scintillators at hard x-ray energies, without the need for cryogenic cooling. This is where **wide band-gap** SCs come in - these are basically **compound** SCs, which are alloys between elements from the II, III, IV, V and VI groups of the periodic table. Typical SC materials are shown in table(4.1) Compound SC have band gaps wide enough for room temperature operation. At x-ray energies, line broadening is dominated by leakage current. This can be minimized by employing Peltier coolers or by passive cooling, using radiative plates.

$Cd_{1-x}Zn_xTe$ (Cadmium-Zinc-Telluride or CZT) is a ternary compound of CdTe and ZnTe, where x is the blending fraction of ZnTe in CdTe. Alloying Zn in CdTe, another room temperature γ-ray detector, allows “stretching” of the band gap. Varying x from

Standard SC	Si, Ge
II-VI compound	CdS, CdSe, CdTe, ZnS, ZnSe, ZnTe, $Hg_{1-x}Cd_xTe$, $Cd_{1-x}Zn_xTe$
III-V compound	GaP, GaAs, GaSb, InP, InAs, InSb
IV-VI compound	PbS, PbSe, PbTe, $Pb_{1-x}Sn_xTe$, $Pb_{1-x}Sn_xSe$
IV-IV compound	SiC, $Si_{1-x}Ge_x$
V-VI compound	Bi_2Te_3
Chalcopyrite	AgGaS, $AgGaSe_2$, $CuInS_2$, $CuInSe_2$, $ZnGeP_2$, $CdGeP_2$

Table 4.1: List of Semiconductor Materials from [1d]

0.04 to 0.2, the band gap can be varied from 1.53 eV to 1.64 eV. The increased band gap increases the resistivity (10^9 ohm-cm), lowers the leakage current, and hence allows operation at higher temperatures. Resistivities of CZT detectors are one to two orders of magnitude higher than that of CdTe detectors.

CZT is a very attractive SC detector material for hard x-ray/soft γ-ray astronomy and

- has a higher stopping power than Si, as it is three times more dense
- has a greater photoelectric to Compton cross-section ratio that either Si or Ge because its effective atomic number, Z_{eff} is 50, compared to Z of 32 for Ge and Z of 14 for Si
- facilitates operation at higher temperatures, providing a compact, energy-efficient detection system

CZT detectors can be fabricated as planar detectors with monolithic electrodes, or with pixellated or cross-strip read-out which can be used for position sensing. CZT detectors are being used on the Burst Alert Telescope (BAT) on the SWIFT mission [2d]. The Energetic X-ray Imaging Survey Telescope (EXIST) [3d] plans to use CZT detectors along with a coded mask aperture, for imaging in the 5-600 keV energy region. The Atmosphere-Space Interaction Monitor (ASIM) [4d] will be mounted on the International Space Station (ISS) to study the impact of space weather on our atmosphere, and will include a Modular X and Gamma-ray Sensor (MXGS) that uses CZT detectors in the 7-500 keV energy region. CZT and CdTe detectors have wide applications in medicine and a comprehensive review can be found in [5d].

The disadvantage of CZT detectors, and compound detectors in general are their poor charge carrier transport properties; in CZT, the mobility μ_e of electrons is an order of magnitude higher than that of holes. Due to the crystal growth techniques, stresses, dislocations and impurities populate the band structure, leading to reduced lifetime of holes τ_h in the crystal, compared to electrons. **Carrier lifetime** defines the time before a carrier is trapped in the crystal lattice due to recombination at impurity or dislocation sites. This will be discussed in detail in the next section.

Leakage currents are reduced when the resistivity of the material is high, which is the case when the purity of the material improves. There are techniques employed to create high purity materials, but there will still be some trace impurities left behind in the material - this results in the material being either slightly n-type (represented by the symbol 'ν') or slightly p-type (represented by the symbol 'π'), depending on the predominance of the residual donor-type or acceptor-type impurities. Materials are also **compensated**, which means that residual impurities are balanced out by doping the purified material with donors of the opposite type of the impurities. The material still ends up being either ν or π, because of the difficulty to precisely balance out the concentration.

It is desirable to use fully depleted SC as radiation detectors. When a heavily doped material (designated as p^+ and n^+) is placed in contact with a lightly doped or intrinsic material of the opposite type, the depletion width extends into the lightly doped region. This happens in order to balance the charge on either side of the junction. On the heavily doped side, the depletion width is very thin.

When a purified or compensated material is placed between thin layers of n^+ and p^+, one of the contacts is a **rectifying contact** while the other one is a **blocking** or **non-injecting contact**. This depends on whether the material in between, is ν or π. A rectifying contact is one that forms a depletion region at the contact, and blocking contact prevents injection of majority carriers into the SC. In the reverse bias condition, the positive terminal is always connected to n^+ and the negative to p^+. Contacts can be also be made between metals and SC ; metal-SC contacts (MSC). These can be either of **blocking (Schottky)** kind or **ohmic** kind.

A Schottky MSC has current-voltage (I-V) characteristics similar to that of a p-n junction, while for an ohmic MSC, the I-V characteristics are linear, following Ohm's law. The difference between the two is in the **barrier height in the SC for electrons** - it is narrower for ohmic contacts than for Schottky contacts. Due to the lower barrier height in ohmic contact, there is an easier flow of electrons from the SC to the metal; this constitutes an additional noise factor in addition to the thermal motion of electrons, which is present in Schottky contacts as well. Therefore, the leakage currents measured in devices with ohmic contacts are an order of magnitude higher than those measured in devices with Schottky contacts.

Tests have been performed on CZT detectors to study the dependence of resistivity and hence leakage currents on the type of contacts used [8d]. Standard IMARAD CZT detectors [6d] (from Orbotech) use Indium-Indium ohmic contacts, which showed an order of magnitude higher leakage current compared to CZT detectors with blocking contacts.

Radiation damage in SC affect the charge lifetime, charge collection efficiency and leakage currents. Displacement of atoms from the crystal lattice to interstitials result in the formation of charge traps. This causes incomplete charge collection, and hence degradation in resolution. Resolution also worsens due to increasing leakage current. Incomplete charge collection also affects the gain of detector, which corresponds to shift of the peak channel.

The CZT modules used for the HEX instrument have been procured from Orbotech Medical Solutions, Israel [6d], grown by the modified Horizontal Bridgman technique. The specifications of these modules are listed in table(4.2)

Density	5.85 g cm^{-3}
Bulk resistivity	3-8 $\times 10^9$ ohm-cm
Mean Zinc content	9-11%
Electron-hole production energy	4.43 eV
Electrode type	ohmic
Electrode material	Indium
CZT material type	n-type
Cathode	Monolithic
Anode	Pixellated
Number of pixels	256
Anode pad size	1.86 mm × 1.86 mm
Pixel pitch	2.46 mm
Read out	XAIM 3.2 ASICS, IDEAS, Norway
Number of channels per ASIC	128
Number of ASICs per module	two
Expected energy resolution (25°C)	5% at 122.1 keV

Table 4.2: Specifications of the CZT modules procured from Orbotech Imaging for the HEX instrument

4.3 Charge trapping and Pulse Amplitude

Recent compound SC growth techniques are still not able to completely eliminate crystal non-uniformities, defects, and impurities. These defects in the crystal lattice can act as traps for charge carriers as they drift along electric field lines. Traps are energy levels or centers in the band gap of the crystal that rapidly capture charge carriers and then release them at a much slower rate. Impurities in the SC, like positively charged donor ions in n-type materials and negatively charged acceptor ions in p-type materials have their energy levels in the SC band gap and act as traps. If charges are trapped in the lattice while they drift towards their respective electrodes, they will not be able to contribute to the measured current signal. Therefore, the signal measured in the presence of traps have a smaller amplitude than signals measured in the absence of traps.

In the absence of an applied electric field, an excess charge created in a SC due to external processes like thermal energy or ionizing radiation causes the equilibrium of the system to get disturbed. The system reverts back to the equilibrium condition by the process of **recombination**. The simplest way that electrons and holes can recombine is via band-to-band recombination, in which an electron in the conduction band fills a hole in the valence band. Charge carrier traps, as discussed above, have energy levels in the SC band gap and are called **recombination-generation centres (RGC)**. Recombination of an electron or hole with a charge trap is called **trapping** and can be defined as

- *electron trapping* - transfer of an electron from the conduction band to the RGC
- *hole trapping* - transfer of an electron from RGC to the valence band

This is illustrated in the fig(4.2).

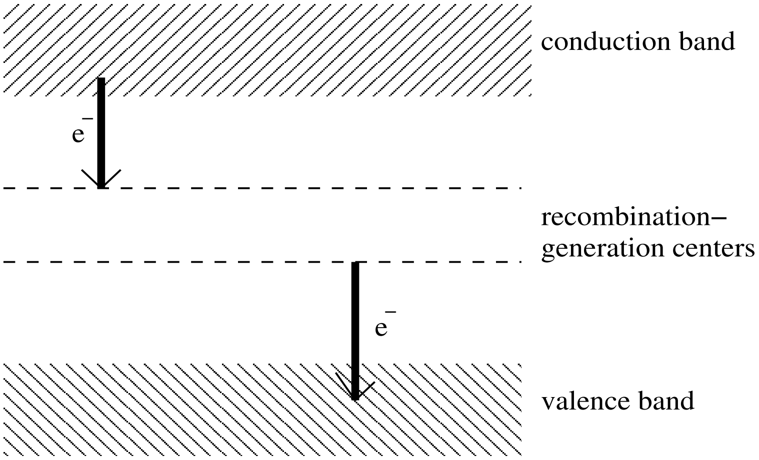

FIGURE 4.2: This is a schematic representing charge trapping. The shaded regions are the conduction and valence bands, while the dashed lines in the band gap are the recombination-generation centres (RGCs). The transfer of an electron from the conduction band to the RGC represents *electron trapping*, while the transfer of an electron from the RGC to the valence band is *hole trapping.*

When the thermal equilibrium of a SC is disturbed, the rate of recombination should increase to bring the system back to equilibrium. In the case of electrons and holes, the capture rates are proportional to

- the concentration of traps or R-G centres, N_t
- the concentration of carriers at thermal equilibrium
- the probability that a trap site is occupied by an electron, f_t, which is given by Fermi-Dirac statistics (pertinent to hole trapping)

N_t is larger in compound SC like CZT compared to Si and Ge. In an n-type compound SC, the Fermi level lies close to the bottom of the conduction band, which means that all trap levels below it have an electron occupancy of 1; the event of a hole encountering such a R-G site always ensures its capture. For p-types, the concentration of holes is large at thermal equilibrium, and so the capture rate is higher compared to that of electrons. This means that the **lifetime** of a hole, or the average time before a hole encounters a RGC, in either n-type or p-type material, is short. This fact coupled with the low intrinsic **mobility** of the holes compared to the electrons ensures that holes have poorer charge transport properties than electrons.

For a charge carrier, the product of the mobility μ, the lifetime τ and the electric field strength ε is λ, the **trapping length** of the carrier and is the distance that the carrier can travel in the detector under the influence of ε, before it is trapped. Typically, the electron and hole mobility-lifetime products, $(\mu\tau)_e$ and $(\mu\tau)_h$ are 10^{-3} $\mathrm{cm^2V^{-1}}$ and $10^{-5}\mathrm{cm^2V^{-1}}$ respectively for CZT detectors. For a bias voltage of -500 V and detector thickness of 0.5 cm, the electric field is 1000 $\mathrm{Vcm^{-1}}$. Assuming that the field within the detector is uniform, one can compute λ_e as 1 cm and λ_h as 0.01 cm. If the distance ‘x’ that a charge carrier has to travel to reach its electrode is greater than its λ, the probability that this charge is lost through trapping is higher than for a carrier whose λ is greater than x. From the above numbers, it is obvious that the holes have a higher probability of getting trapped than electrons.

The poor transport properties of holes demand illumination from the cathode side of the detector; holes generated near the cathode by low energy incident radiation do not suffer the kind of trapping that holes generated by more penetrating radiation do. High energy x-rays and γ-rays are more penetrating and interact through out the detector active volume. Holes generated near the anode have to traverse a path that is longer than their trapping length and hence are lost and cannot contribute to the total charge collected.

From eqn(4.9), it can be seen that the total induced charge is dependent on the distance traveled by the electrons and holes. In the *absence* of charge trapping, the *shape* of the charge pulse is dependent on the distance traveled. However, the presence of traps also affects the **amplitude** of the charge pulse, because once a charge carrier has been trapped in an RGC, it is no longer mobile and does not contribute to the induced charge. So the signal collected will have an amplitude that is always less than what it should have been in the absence of charge trapping. The Hecht equation [24d]

$$\eta = \frac{\lambda_e}{d}\left(1 - e^{-\frac{(d-x)}{\lambda_e}}\right) + \frac{\lambda_h}{d}\left(1 - e^{-\frac{x}{\lambda_h}}\right) \tag{4.13}$$

gives the **charge collection efficiency (CCE)**, η which is the ratio of the charge induced at the electrodes to the total charge created at the site of radiation interaction in the detector, and it shows the dependence of interaction position on the amplitude of the signal pulse. In eqn(4.13), x is the distance of the interaction position from the cathode, and d is the depletion width or the active thickness of the CZT detector. From this equation it can be seen that going for thinner detectors improves η. Also, increasing the bias voltage increases the trapping lengths thus improving η. Hole trapping causes signal pulses due to monoenergetic radiation, to have varying amplitudes, and these manifest themselves in pulse height spectra as "tails" at the low energy side of the Gaussian photopeak. The number of counts in the photopeak is larger for the same photon energy in the absence of trapping than otherwise. Trapping of electrons however, results in gain shifts or shifts in the photopeak position in the pulse height spectra.

The spectra of high energy photons measured by CZT detectors show more prominent hole tails than low energy photons that interact near the cathode. This leads to lower **spectral peak sensitivity**, which is defined as the ratio of the counts under the photopeak to the total counts under the spectrum. When a radiation source consisting of multiple photon energies are measured by CZT detectors, the sensitivity of low energy peaks are lost, because of the increased low energy continuum, caused due to overlap of hole tails of higher energy spectral lines. So, loss of line-to-continuum sensitivity is the major effect of hole trapping in CZT detectors.

Hole tailing is important in applications where the distance that the carriers have to travel is larger than the trapping length. It depends on the energy of the photons that are being measured. The carrier lifetimes vary within a single detector, so careful calibration of the detector and subsequent extraction of the mobility-lifetime products for both electrons and holes, $(\mu\tau)_{e,h}$ is an important part of detector characterization.

This chapter focuses on the simulation of the HEX CZT detector response using Geant4. Experimental determination of $(\mu\tau)_{e,h}$ products is an essential part in the modeling of CZT spectral response, along with experimental measurements of variation spectral parameters with energy. This experimental characterization is discussed in the next section.

4.4 Laboratory Tests on a single CZT module

The nine CZT detectors used in HEX were characterized at the Physical Research Laboratory (PRL) Ahmedabad in a hot-cold chamber. The details of the experimental set up and experimental methodology can be found in [25d]. The radioactive sources ^{241}Am and ^{57}Co were placed at appropriate distances from the test set up so as to enable uniform pixel illumination. The chamber temperature was varied from -20°C to 25°C in steps of 5°C. At each temperature, spectroscopic measurements were made at three different operating bias values, -500 V, -600 V and -700 V. For the present work, only data measured by one of the flight detectors B11290, was analyzed for extraction of $\mu\tau$ products and spectral parameters, with the assumption that the overall response of other detectors were not significantly different.

4.4.1 Extraction of Mobility-Lifetime products

The method of extraction of charge carrier mobility-lifetime ($\mu\tau$) products has been adapted from [26d]. Here, the pulse height spectra recorded by the detector at different bias voltages are fit simultaneously with a model that take into account a Gaussian photopeak and a low energy exponential tail. This exponential tail follows from eqn(4.13). So in effect, the pulse height spectrum is modeled and this model is then fit to the experimental data to extract the $(\mu\tau)_{e,h}$ products.

The spectra due to 122.1 keV photons from the ^{57}Co source were used to extract the $(\mu\tau)_{e,h}$ values, as photons of this energy interact throughout the active volume of the detector and its spectral shape best represents the charge carrier transport properties.

Raw data were reduced using specifically written PERL scripts for further analysis using Sherpa [27d] in CIAO [28d]. CIAO (Chandra Interactive Analysis of Observations) is a flexible, multi-dimensional software designed for the analysis of data from Chandra X-ray Observatory. The design of CIAO is mission independent - it can be used to analyze data from any another mission or even laboratory data. All CIAO tools read and write in several formats, from ASCII text to FITS images and tables. Sherpa is the modeling and fitting tool of CIAO, which fits models to N-dimensional data. In addition to Sherpa's built-in models, user-defined models can be constructed and registered with Sherpa, and used in same manner as the built-in models. The scripting language S-Lang [29d] has been embedded in CIAO, and is used to extend the functionality of Sherpa. S-Lang is an array based language, featuring conditional and looping syntax, global and local variables, user-defined structures and functions, and to a lesser extent, pointers.

The model to fit the ^{57}Co data was written in S-Lang. The ^{57}Co pulse height spectrum is modeled in S-Lang as follows :

1. The detector was divided into a number of thin slices.
2. Using the attenuation coefficient for the photon energy under study, the interaction probability dI(x) was calculated for each depth dx. The total number of counts under the spectral region of interest is then multiplied by the interaction probability at each depth to obtain the counts detected at that depth.
3. Using the Hecht equation and Ch_{max} (the channel number at which the Hecht equation is equal to unity), the pulse amplitude at each depth was computed. This was repeated for each operating voltage.
4. These pulse amplitudes are then convolved with a Gaussian distribution which represents the broadening due to Fano statistics and electronics noise.
5. The counts at each depth and the pulse height at each depth now give the model spectra for each operating voltage.

This model is compiled and executed in a Sherpa command batch script.

For a particular temperature, the ^{57}Co data measured at one of the bias voltages, is split by a specifically written PERL script into 256 files, each file corresponding to one pixel. This is repeated for each of the other two bias voltages, resulting in a total of 768 data files for that temperature. So, for one temperature, a pixel of the detector will have three files attached to it, each file corresponding to a high voltage value.

The spectral fitting with the model is done pixel-wise. A Sherpa batch file reads in the three spectral data files corresponding to one pixel, and then compiles and registers the model before fitting the data.

The model consists of eighteen parameters, as each bias voltage has six parameters attached to it; $(\mu\tau)_e$, $(\mu\tau)_h$, spectral width parameter σ, electric field value, Ch_{max}, and the total number of counts within the region of interest of the spectrum used for the fitting. Out of these eighteen parameters, the electric field values are frozen, and the six $(\mu\tau)_{e,h}$ values are linked together as their values are dependent on the material properties. Ch_{max} is that channel which corresponds to complete charge collection, in the absence of trapping. It is proportional to the total charge generated by the incident photon at the interaction site. It is independent of the applied electrical field, and so, in order to eliminate the effects of the electric field, data measured at three different bias voltages are fit simultaneously. Therefore, the three Ch_{max} values are also linked. This brings the number of free parameters to nine, whose values are obtained from the fit.

The initial guess values of the parameters are supplied to the fitting algorithm, and the three data files are fit simultaneously with the model, till the best fit is arrived at, for this pixel. The same is done for all the other pixels.

This process is repeated for all the temperatures in the range over which the measurements were taken. Only those pixels that had clean spectra, i.e. spectra with well resolved photopeaks, were chosen for the analysis.

The fig(4.3) and fig(4.4) show the distribution of the $(\mu\tau)_e$ and $(\mu\tau)_h$ products respectively, over all clean pixels, for each temperature. These distributions were constructed by binning these values as a function of pixel number, i.e. by finding the frequency distribution of $(\mu\tau)_e$ and $(\mu\tau)_h$ products as a function of CZT pixel. This is repeated for each temperature.

The $(\mu\tau)_e$ distribution shows a bipolar trend for all temperatures. Averaging over temperature, about 80% of the pixels used in each distribution, fall in the larger peak. This bipolar trend indicates that the $(\mu\tau)_e$ values of some pixels are overestimated, that is, showing a smaller value than majority of these pixels. These pixels with smaller values of $(\mu\tau)_e$ could be the edge pixels of the detector module, as evidenced by studies in [31d] and references within. In order to verify this with respect to the HEX CZT, one has to map these pixels onto the CZT pixel map supplied by the manufacturer to see where these are located with respect to the crystal, i.e. whether they are edge pixels or inner pixels, or if they are randomly distributed over the crystal.

The $(\mu\tau)_h$ distribution on the other hand shows more deviation between pixels, for each temperature. The bi-polarity, if it exists as in the case of $(\mu\tau)_e$, would have been smeared out by this large deviation. Slight evidence of this bi-polarity can be seen for some temperatures. For the purpose of studying the variation of the $(\mu\tau)_{e,h}$ as a function of temperature, the data were averaged over all pixels. This was done for each temperature by taking the arithmetic mean over the pixels; this was used instead of Gaussian determination of mean because it was required to make use of data of all the pixels. The pixel averaged values are designated as $(\mu\tau)_{e_{avg}}$ and $(\mu\tau)_{h_{avg}}$.

Figure(4.5) shows the variation of $(\mu\tau)_{e_{avg}}$ and $(\mu\tau)_{h_{avg}}$ values with temperature. It can be seen that $(\mu\tau)_{e_{avg}}$ and $(\mu\tau)_{h_{avg}}$ vary linearly with temperature, with $(\mu\tau)_{e_{avg}}$ flatter than $(\mu\tau)_{h_{avg}}$. Linear fits to the data show that for every 5°C variation with temperature, $(\mu\tau)_{e_{avg}}$ varies by 0.7% while $(\mu\tau)_{h_{avg}}$ varies by 2.3%. The larger variation seen for $(\mu\tau)_{h_{avg}}$ is due to the inherent spread of the $(\mu\tau)_h$ values seen in fig(4.4).

Before one studies the significance of this variation of the charge carrier $(\mu\tau)_{e,h}$ with temperature, one must first understand the significance of these parameters on the shape of the pulse height spectrum. $(\mu\tau)_e$ defines the location of the peak or maximum value

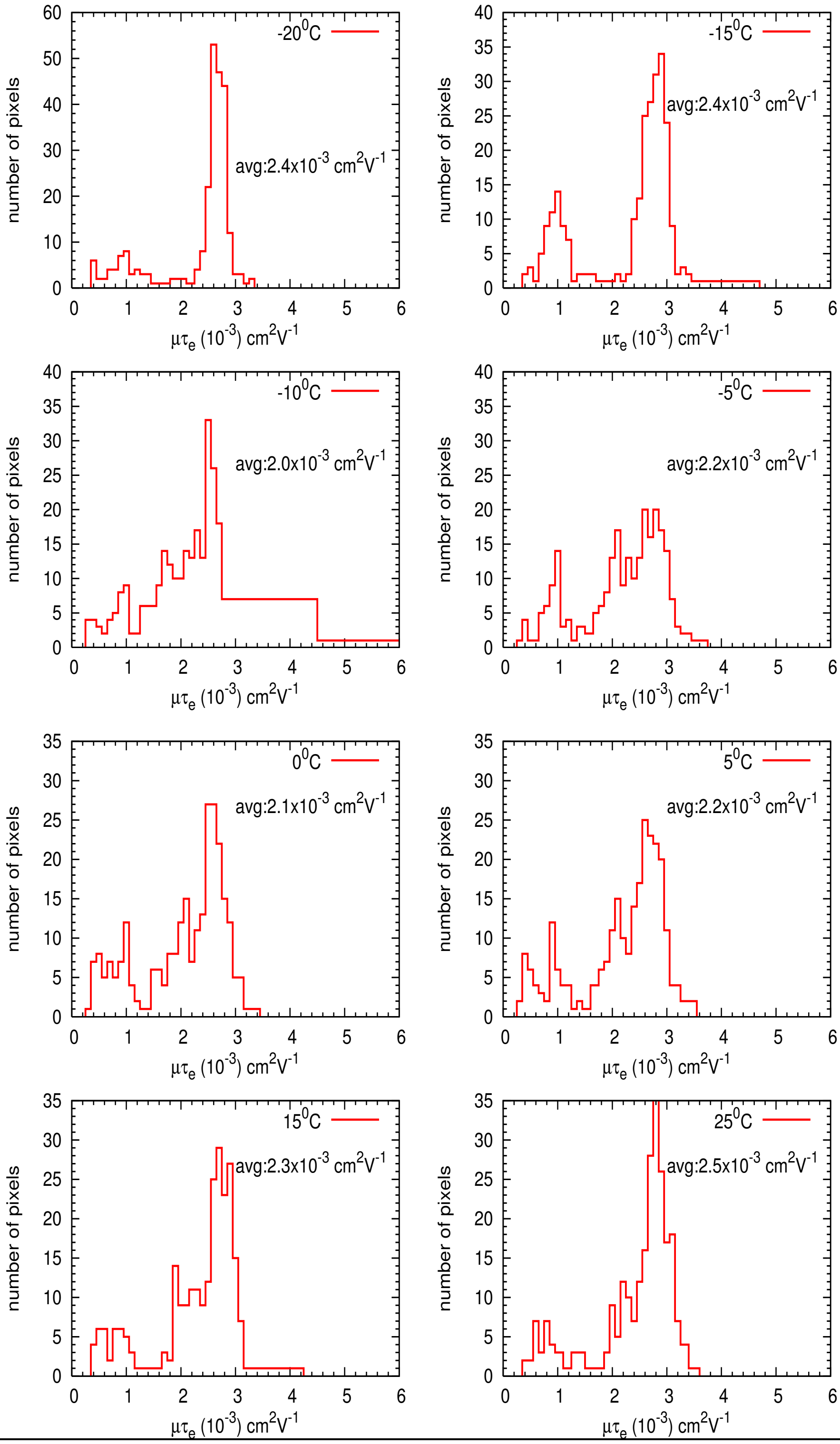

FIGURE 4.3: Distribution of $(\mu\tau)_e$ over all pixels, for each temperature.

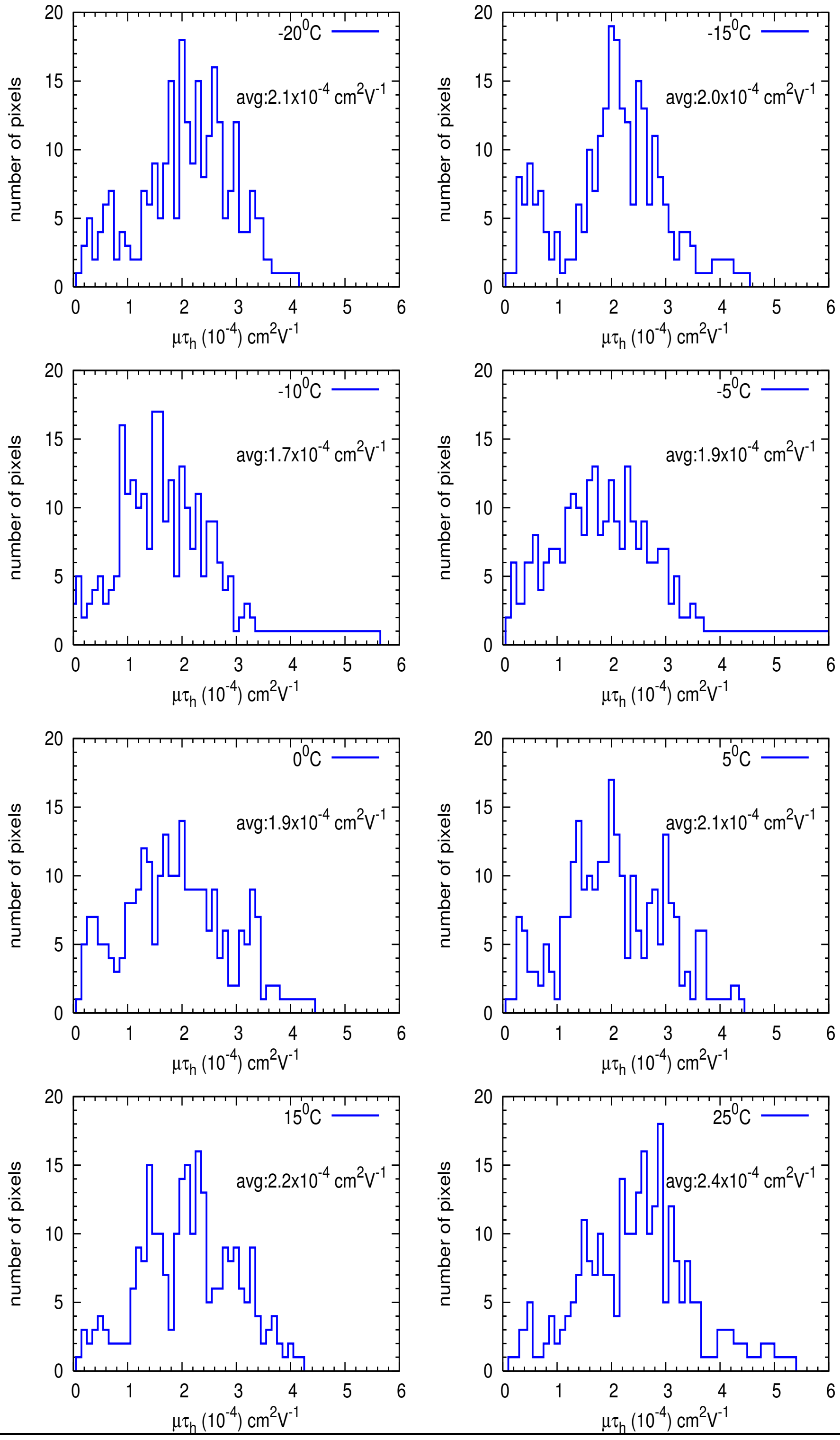

FIGURE 4.4: Distribution of $(\mu\tau)_h$ over all pixels, for each temperature.

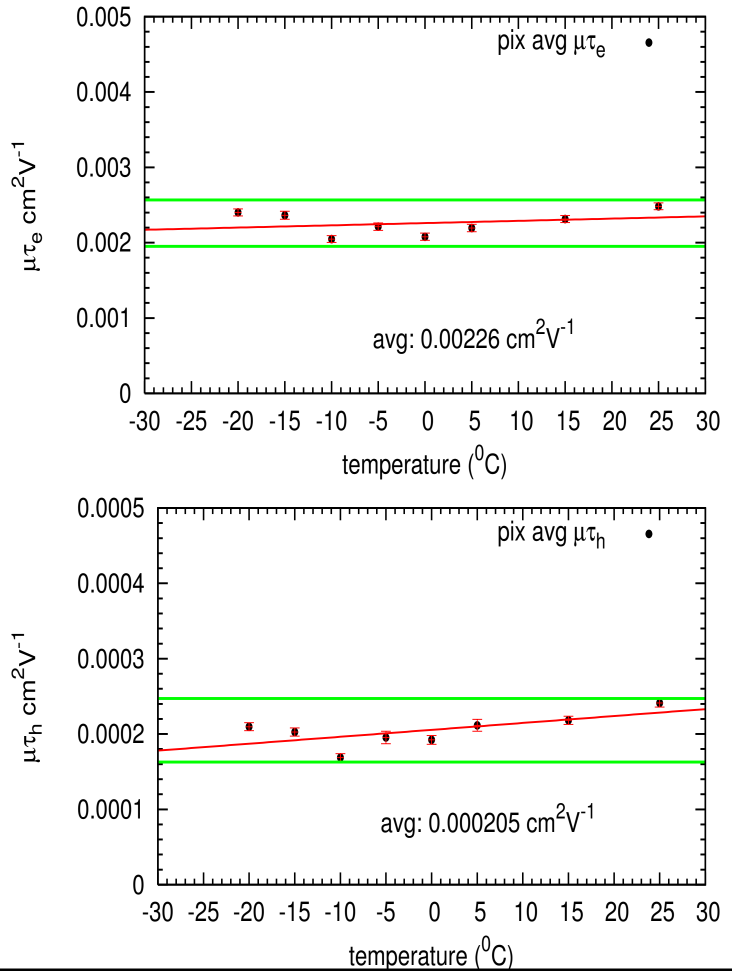

FIGURE 4.5: Pixel averaged $(\mu\tau)_e$ and $(\mu\tau)_h$ plotted as a function of temperature. The horizontal green lines in each plot are the 2σ limits.

of pulse height that is measured at a particular operating voltage. $(\mu\tau)_h$ defines the amount of tailing observed in a spectrum for a particular value of electric field and $(\mu\tau)_e$. For low values of $(\mu\tau)_h$, the counts under the photopeak or the **photopeak area** is less compared to high $(\mu\tau)_h$ values.

Using eqn(4.13) one can study the variation of η over the detector thickness for different values of $(\mu\tau)_e$, $(\mu\tau)_h$, and electric field ε. One can define a "photosensitive" region of the detector as that depth of the detector which contributes to the photopeak of the spectrum. In order to define this, the benchmark for defining this region has been chosen to be that depth over which the η varies from 100% to 70%. All subsequent η calculations have been performed for the case of x-ray illumination from the cathode side.

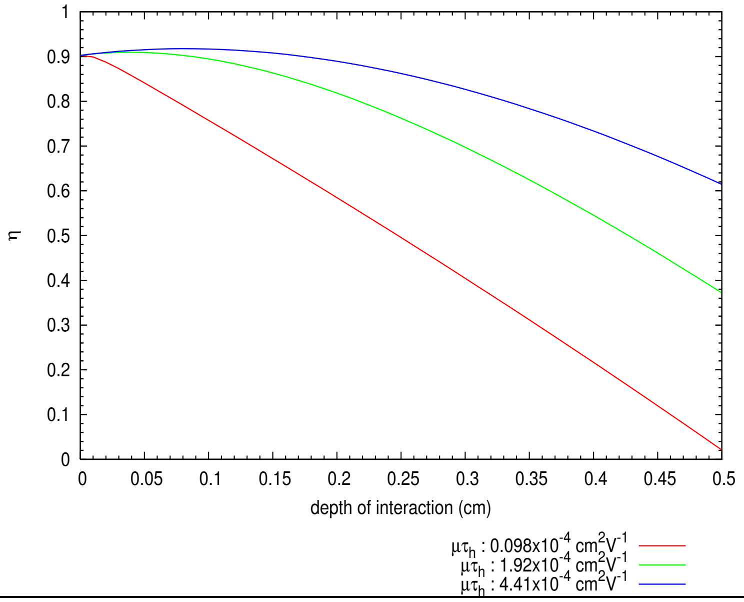

FIGURE 4.6: Charge collection efficiency (CCE) η, plotted as a function of interaction depth for an operating bias of 530 V, at a temperature of 0°C. η was calculated using 3 different values of $(\mu\tau)_h$, as indicated, and the pixel averaged $(\mu\tau)_e$ value for 0°C. The x-axis represents the depth of the detector, from the cathode side. 0 cm indicates the cathode, and 0.5 cm indicates the anode.

Consider fig(4.6); it shows the variation of η for different values of $(\mu\tau)_h$ at 0°C, computed using the eqn(4.13) - the electric field is calculated for 530 V (which is the CZT in-orbit operating bias voltage), and the $(\mu\tau)_e$ value used is the pixel averaged value. As can be seen, η falls off faster for the lowest value of $(\mu\tau)_h$, compared to the slow fall for the highest value. In terms of the earlier definition for the photosensitive region,

- only 27% of the total detector depth contributes to the photopeak for the lowest $(\mu\tau)_h$ value; this means that for N photons of energy E that interact throughout the detector, 73% of the events fall under the low energy tail
- 86% of the total detector depth contributes to the photopeak for the highest $(\mu\tau)_h$ value; this means that for N photons of energy E that interact throughout the detector, 14% of the events fall under the low energy tail
- for the intermediate value of $(\mu\tau)_h$, the photosensitive region is 60% of the total detector depth; this means that for N photons of energy E that interact throughout the detector, 40% of the events fall under the low energy tail

This indicates the significance of $(\mu\tau)_h$ on the tailing observed in the pulse height spectra; lower the $(\mu\tau)_h$ value, larger will be the fraction of photopeak counts "lost" in the tail compared to that for higher $(\mu\tau)_h$ values.

Therefore, as seen in fig(4.5), the variation of $(\mu\tau)_{e,h}$ with temperature will be reflected in the shape of the measured pulse height spectrum.

Figure(4.7) illustrates the effect of increasing the bias voltage on the photopeak efficiency. The temperature averaged values of $(\mu\tau)_{e,h}$ from fig(4.5) were used in eqn(4.13) to calculate η for 530 V, 600 V, and 700 V. There is a visible difference in η as seen in the figure, which corresponds to a difference of 12% in sensitive volume between the highest and lowest operating voltage value.

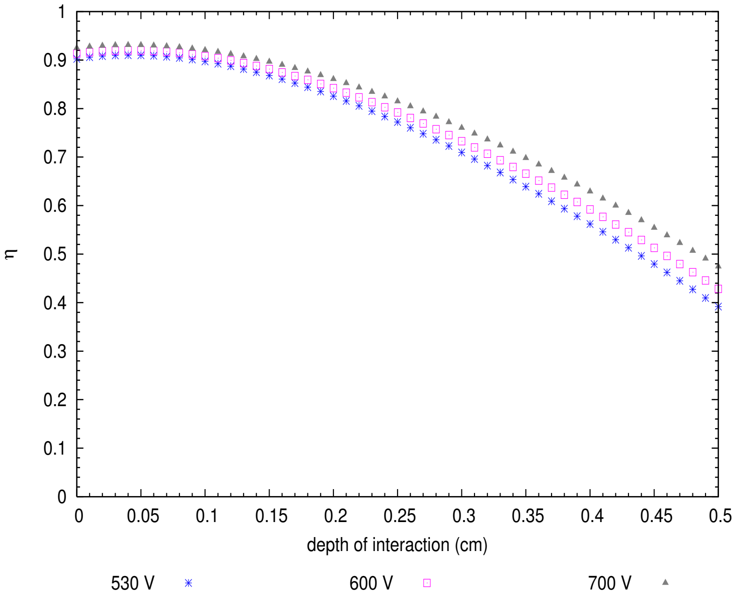

FIGURE 4.7: Charge collection efficiency (CCE) η, plotted as a function of operating voltage using the temperature averaged values of $(\mu\tau)_{e,h}$. The x-axis is along the depth of the detector, from the cathode side. 0 cm indicates the cathode, and 0.5 cm indicates the anode.

The CCE also depends on the energy of the incident photon, which determines the distribution of photon interaction sites within the detector. In fig(4.8), 0 cm indicates the cathode and 0.5 cm indicates the anode for a 0.5 cm thick detector. The green dots in each plot is the interaction site or **depth of interaction (DOI)** of the incident photon in the detector. For the purpose of this calculation, photons of energy 30 keV and 122 keV were considered. The DOI for each energy in the CZT were extracted using Monte Carlo simulations. A simple simulation application was developed for a CZT detector modeled with appropriate materials; γ-ray photons where made to illuminate the region of the crystal which was designated as the cathode. For each incident photon energy, the DOI in centimeters was extracted and written into an output file. For each energy, the DOI were inserted into eqn(4.13) to compute η. The η for each energy is indicated by the red points in fig(4.8). The $(\mu\tau)_{e,h}$ values used in the calculation of η were the temperature-averaged values as shown in fig(4.5) and the operating voltage used was 530 V.

From the plots it can be seen that all the 30 keV interactions contribute to the photopeak (defined by the photosensitive region discussed above), while only 60% of the 122 keV interactions in the detector contribute to the photopeak. This is because of the difference in DOI distribution between the two energies; for 30 keV, the DOI distribution is tightly bunched near the cathode (corresponding to depth 0 cm), while for 122 keV, the DOI distribution is more or less spread over the detector volume. This indicates that the 30 keV spectral peak will show insignificant tailing compared to the 122 keV peak.

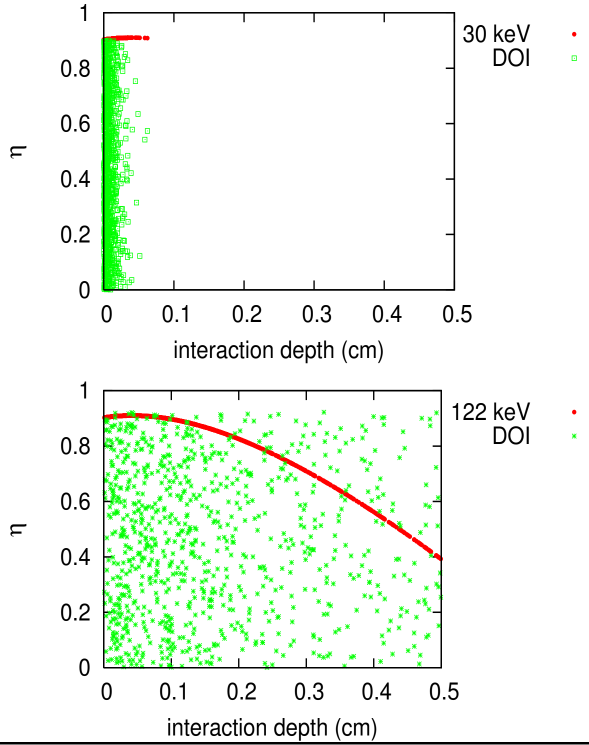

FIGURE 4.8: Variation of charge collection efficiency (CCE) η, with incident photon energy. The x-axis represents the depth of the detector, from the cathode side. 0 cm indicates the cathode, and 0.5 cm indicates the anode. The top plot shows the variation of η with interaction depth in the detector for 30 keV. The green squares represent the depth of interaction (DOI) of each of the incident 30 keV photons within the detector, and the red points represent the η value at that DOI. The same applies to the bottom plot which shows the variation of η with DOI in the detector for 122 keV.

To summarize

- Knowledge of the detector charge transport properties is essential for accurate modeling of the CZT detector response.
- $(\mu\tau)_e$ determines the location of the maximum pulse height amplitude.

- $(\mu\tau)_h$ determines the low energy tailing in the spectrum.
- Photopeak efficiency (ratio of photopeak area to area under spectrum) improves with larger values of $(\mu\tau)_h$.
- Lower energy photons exhibit little or no tailing in their spectra, while it is enhanced for higher energy photons.

In order to complete the modeling of the detector response, one must extract spectral parameters from the experimental data and study their variation with energy and temperature.

4.4.2 Extraction of Spectral Parameters

The spectral parameters for CZT module B11290 were extracted by analyzing the data measured by the detector at -500 V, for different temperatures. This voltage value was chosen because it is closest to the voltage that will be used for flight (-530 V). The data analysis was performed as follows:

- IDL (Interactive Data Language) [30d] scripts were written to fit the ^{241}Am and ^{57}Co spectra of each pixel for each temperature. As a consequence of the spectral fitting, the peak channels for the 59.5 keV and 122.1 keV peaks were obtained for each pixel, and the gain and offset values were obtained by a two point calibration using the relations below

  $$(Ch_{122.1})_i = G_i * (122.1) + O_i \tag{4.14}$$

  $$(Ch_{59.5})_i = G_i * (59.5) + O_i \tag{4.15}$$

  where $(Ch_{122.1})_i$ and $(Ch_{59.5})_i$ are the peak channels of 122.1 keV and 59.5 keV respectively, for the ith pixel; G$_i$ and O$_i$ is the gain and offset of the ith pixel. The gain and offset are terms that define the linear relation between the channel number and energy (similar to the slope and intercept); gain and offset are in units of channel/keV and channel, respectively.

- Using the gain-offset values obtained for each pixel, the spectra for each pixel are converted from channel space to energy space. Due to the large amount of data, 100 pixels were randomly selected for each temperature. The energy spectra are fit with Gaussian functions (eqn(4.16)) to extract σ for each energy in units of keV.

  $$f(x) = A * exp\left[-\frac{(x-H)^2}{2\sigma^2}\right] \tag{4.16}$$

where H is the peak energy, A is the maximum value (counts or count rate) at H and σ is the FWHM divided by 2.35, the 'spectral width parameter' in keV.

- The above steps are performed for all temperatures, and so the gain, offset and σ-energy relation for each pixel of the module are obtained as a function of temperature.

4.4.2.1 Variation of Channel number with temperature

The gain varies from pixel-to-pixel by 3%, while the offset varies by 10% for all temperatures. Since these variations lie within the 2σ confidence intervals, gain and offset values are averaged over all pixels, for each temperature, by computing the arithmetic mean. The variation of pixel averaged gain (G_{pix}) and offset (O_{pix}) with temperature is linear, and each data set is fit with a straight line. The best fit equations are given by

$$G_{pix}(T) = 8.072 - (0.012)T \tag{4.17}$$

$$O_{pix}(T) = 491.08 + (0.051)T \tag{4.18}$$

where T is the temperature in degrees C.
From these equations, it has been determined that there is a 1 channel increase, for every 1°C rise in temperature, after taking into account the entire energy range of operation.

4.4.2.2 Variation of Spectral Width Parameter with Energy and Temperature

Figure(4.9) shows three plots, each one representing one energy. The x-axis in each plot is the pixel number or ID and the y-axis is the σ in units of keV measured for that energy. The different symbols in each plot corresponds to a particular temperature (refer the legends). From the plots it is observed that

- there is minimal variation of σ among pixels
- for each energy, σ shows no observable temperature dependence
- pixel and temperature averaged σ shows no energy dependence

In order to understand these results, one must consider those factors that contribute to spectral line broadening in a detector. As discussed in chapter 1, the measured variance in the detected signal is given as the sum of the following components

$$\sigma^2_{tot} = \sigma^2_{Fano} + \sigma^2_{ENC} \tag{4.19}$$

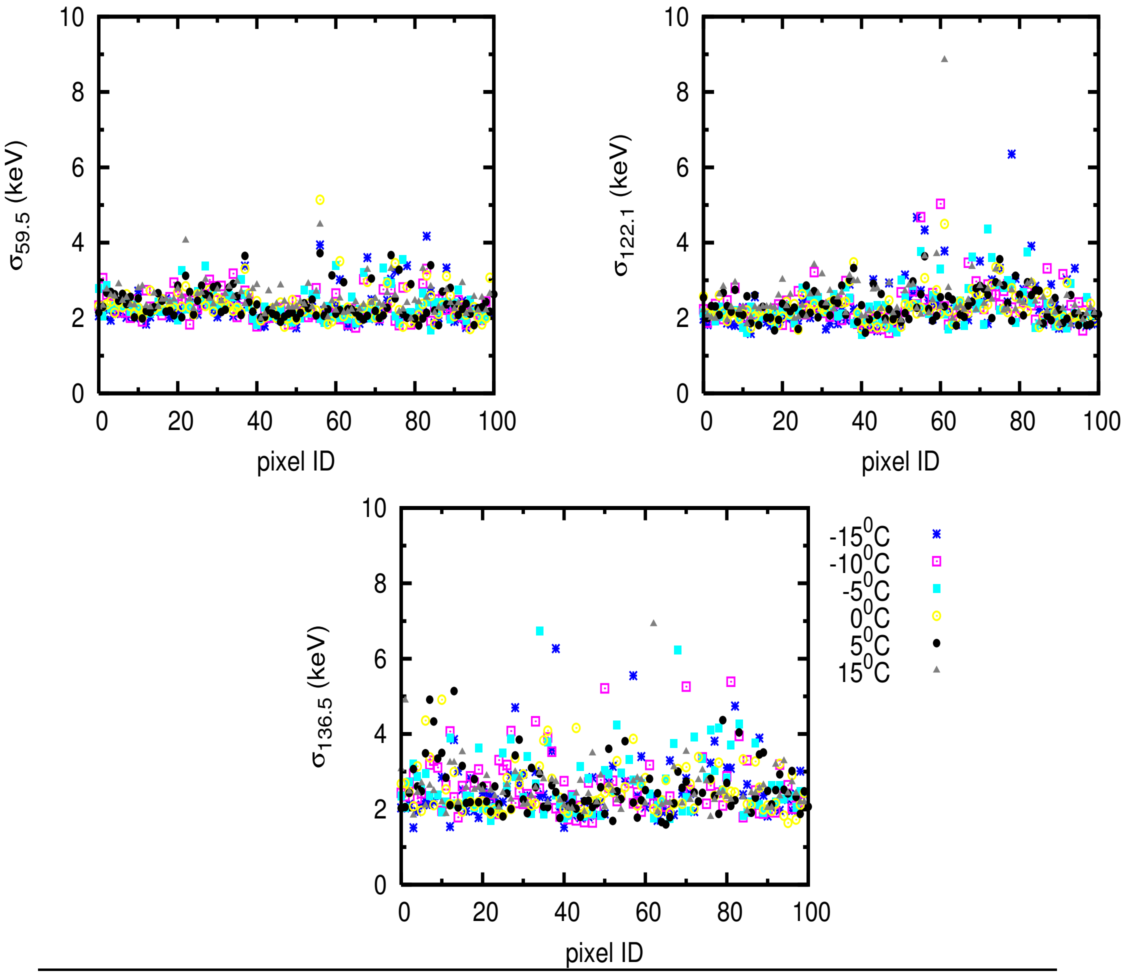

FIGURE 4.9: Representation of the distribution of σ (keV) with pixel number, for the three different energies. The different symbols represent σ measured at different temperatures. The figures show minimal variation of σ between pixels, and no visible energy or temperature dependence. **Top left**: σ for 59.5 keV, the temperature averaged value is 2.36 (± 0.41) keV; **Top right**: σ for 122.1 keV, the temperature averaged value is 2.35 (± 0.57) keV; **Bottom**: σ for 136.5 keV, the temperature averaged value is 2.57 (± 0.74) keV

where σ^2_{Fano} is the contribution to spectral line broadening due to statistical fluctuations in the number of charge carriers produced by incident radiation, and σ^2_{ENC} is the contribution due to electronic noise, or ENC (refer section 1.1.3) in units of number of electrons. These terms are expressed mathematically in units of (keV)^2 by

$$\sigma^2_{Fano} = FEW \tag{4.20}$$

$$\sigma^2_{ENC} = W^2(\text{ENC})^2 \tag{4.21}$$

As discussed earlier, the spectral width parameter, σ(E) is the square root of $\sigma^2(E)_{tot}$, and can be written in terms of its constituents as

$$\begin{aligned} \sigma &= \sqrt{\sigma^2_{tot}} \\ &= \sqrt{\sigma^2_{Fano} + \sigma^2_{ENC}} \\ &= \sqrt{(FEW) + W^2(\mathrm{ENC})^2} \qquad (4.22) \end{aligned}$$

where F is the Fano factor of the material, E is the energy of the photon, W is the minimum energy required to create an electron-hole pair in the detector. F is experimentally measured for the AMPTEK CdTe detector (section 2.4.1) and this value is used for the CZT detector in this calculation; the value of W is taken as that given by the manufacturers (see table(4.2)). These two parameters are frozen for the fit. For each temperature, data corresponding to pixel averaged σ versus energy were fit using eqn(4.22), and the value of ENC was extracted as the best fit parameter. The ENC values extracted from the fit for each temperature using the equation show no dependence on temperature. Leakage current for these detectors show a slow exponential decrease with decrease in temperature, but this has been washed out by some temperature independent component. The source of this noise could be the ASICs that are bonded to the CZT detector. After averaging over temperature the ENC value is, 510 electrons.

In order to illustrate the effects of the ENC on the energy dependence of σ, consider fig(4.10). It shows the contribution of ENC and inherent statistical fluctuations to the measured spectral width, as a function of energy. The measured values (black points) are pixel-averaged values for 0°C, and the error bar on each point is the standard deviation. If the dominant source of peak broadening was due to statistics of charge generation in the CZT detector (calculated using eqn(4.21)), then the σ values would show an energy dependence σ_{Fano}, as shown by the blue points in the graph. The horizontal line represents the σ_{ENC} due to the ENC alone (calculated using eqn(4.21), using the experimentally measured value of 510 electrons); the measured σ values are the quadrature sum of σ_{Fano} and σ_{ENC}. As seen, the ENC dominates the measured σ values, washing out the energy dependence. This is the case for all temperatures.

To summarize

- Channel number increases by one unit (~70 eV for this system) for every 1° rise in temperature.
- σ shows no energy dependence or significant variation with temperature. Pixel-to-pixel variation of this parameter is minimal and can be neglected for all practical purposes.

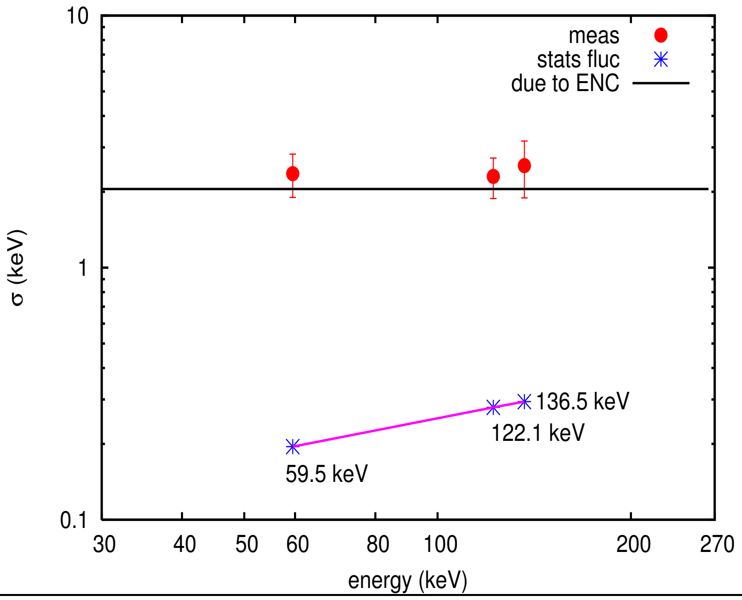

FIGURE 4.10: This plot shows the effect of ENC on the value of σ. The x-axis is the energy (keV). The red points are the experimentally measured values of σ at 0°C, and the blue points are what the measurements would have been if the only contribution were from statistical fluctuations of charge generation. The blue points show dependence on energy. The ENC contribution is shown by the solid line, which corresponds to 510 electrons.

- The energy dependence and temperature dependence of σ is smeared out by a dominant, temperature independent source of electronic noise. This is attributed to a non-thermal noise component arising from the ASICs.

The data obtained from laboratory characterization of the detector was used to extract the $(\mu\tau)_{e,h}$ which are important for modeling the detector SRF. Spectra obtained during detector calibration were used to measure spectral parameters like gain, offset and σ and study their behavior with energy and temperature. The final response matrix will however have to be constructed using data measured by the CZT in the flight configuration.

The HEX payload was characterized in a thermovaccum chamber with purpose of monitoring its operation in vacuum with varying temperatures. As part of the procedure, the CZT detectors were calibrated and the events were processed and stored using the flight electronics.

The next section discusses the results obtained after analysis of data measured during calibration in the thermovaccum chamber.

4.5 Results from the Thermovacuum calibration of module B11290

HEX was placed in a thermovacuum chamber and cycled through a temperature range of -20°C to +45°C for a period of 10 days under a vacuum of a few 10^{-5} torr in order to assess the performance of the payload under a simulated space environment. The CZT detectors were powered on only between temperature limits of -20°C to +15°C. This thermal range of operation was constrained due to CZT array temperature limits. Unlike the laboratory calibration which was done individually for the bare crystals using the electronics provided by IDEAS (section 1.2.2), during the thermovacuum calibration

- all nine detector modules were mounted on the same board and were simultaneously biased from a common power supply developed as part of the payload
- all associated locally developed electronics were also mounted in the actual flight configuration
- the power was supplied via DC/DC converters as expected during actual operation in space
- the stainless steel collimator was mounted in front of the CZT detector array; the radiation used to calibrate the detectors was thus modulated by the collimator response before incidence on the detectors.

The data measured by the module B11290 was reduced and analyzed as described in section 4.4.2.

The channel-energy relation expressed by eqn(4.23) was used to extract the gain and offset for different temperatures.

$$\text{Channel} = \frac{\text{Energy}}{\text{Gain} * 10^{-3}} + \text{Offset} \tag{4.23}$$

where gain and offset are in units of eV/channel and channel, respectively.

Gain and offset were extracted for each pixel for every temperature. The pixel-to-pixel variations of the gain and offset were not very significant and so were averaged over all pixels. Thus, for every temperature, there is a pixel-averaged value of gain and offset, G_{pix} and O_{pix} and the equations (4.24) and (4.25) express the temperature dependence of these two parameters

$$G_{pix}(T) = 192.7 + (0.256)T \quad \text{eV/channel} \tag{4.24}$$

$$O_{pix}(T) = -85.47 + (1.76)T \quad \text{channel} \tag{4.25}$$

where T is the temperature measured in degrees C.

These equations show that the channel number increases by one unit (~244 eV for this system) for every degree rise in temperature, which is consistent with what was seen from the laboratory calibration.

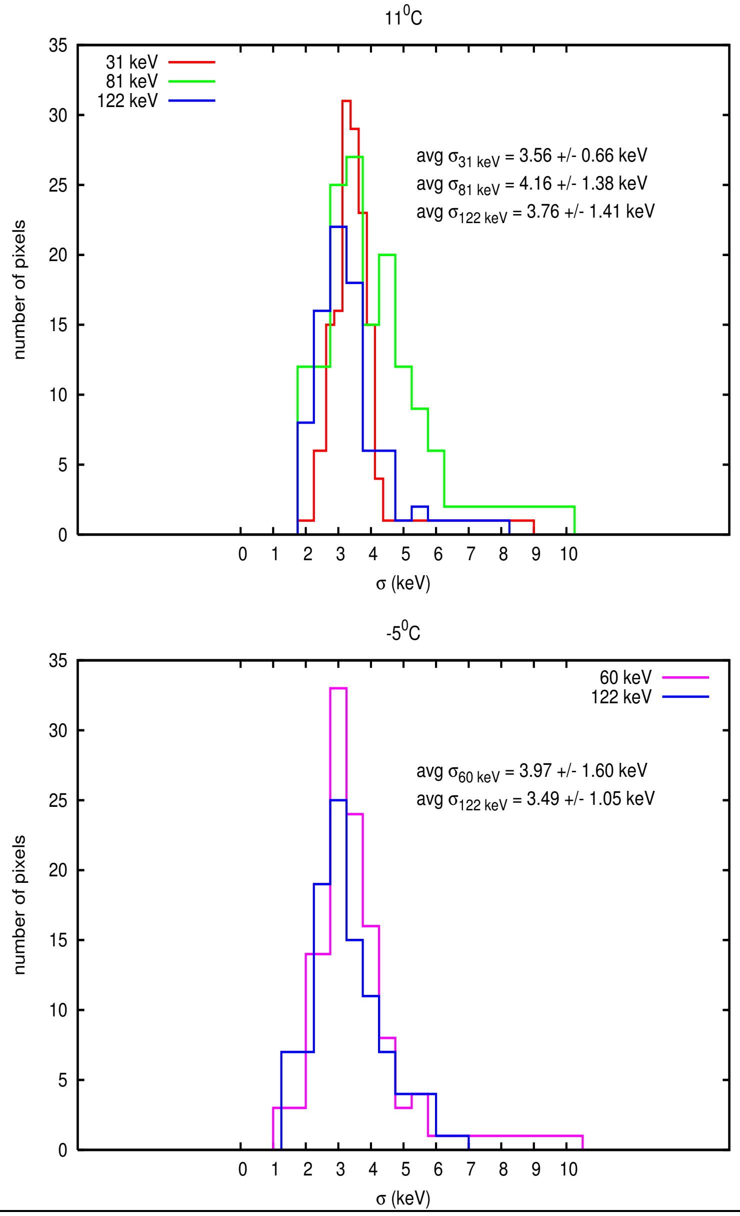

FIGURE 4.11: These plots are σ-histograms; the σ (keV) values for pixels are binned. **Top**: σ-histograms for 30.97 keV, 81 keV, and 122.1 keV, measured at a temperature of 11°C; the average σ values show no dependence on energy; **Bottom**: σ-histograms for 59.5 keV and 122.1 keV measured at a temperature of -5°C; there is still no energy dependence seen. Also note that there is no difference between the mean σ of 122.1 keV measured at high and low temperatures.

Figure(4.11) shows two plots which are σ-*histograms*; these are constructed by binning σ (keV) values of all pixels, for each energy. The σ-histograms are plotted here for 30.97

keV, 81 keV, and 122.1 keV at a temperature of 11°C. As can be seen, the graphs follow a Gaussian distribution, and it is evident that for each energy, the peaks of the Gaussian lie at the same value on the x-axis. This indicates that the mean σ value for each of the energies is the same, within errors. σ-histograms are also plotted for 59.5 keV and 122.1 keV at -5°C; once again it can be seen that the peaks of the distributions lie at the same value. Also, the mean value of σ computed for 122.1 keV shows no difference between higher and lower temperatures. From this one can observe that the energy and temperature dependence of σ have been smeared out by a dominant noise factor.

Equation(4.22) was used to fit pixel and temperature averaged σ values versus energy to extract the ENC value in units of number of electrons, and this value was found to be 818 (± 27) electrons. As was depicted in fig(4.10), the dominant effect of ENC on the measured value of σ during thermovacuum calibration is shown in fig(4.12). From the above study, it is clear that the contribution of this temperature independent noise is larger when measurements are made with the **flight electronics**. The average σ measured using thermovacuum data is larger by a factor of 1.5 compared with the average σ measured using laboratory data. Potential sources of this noise include the power line noise from the DC-DC converters.

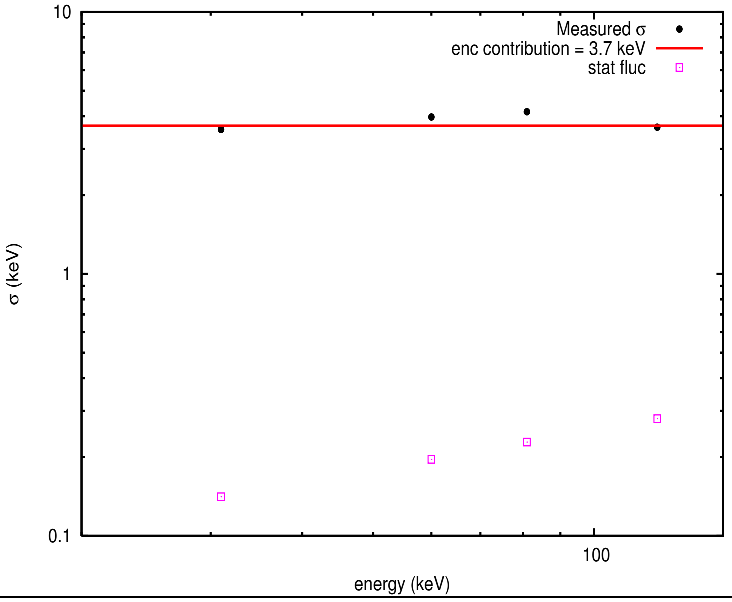

FIGURE 4.12: This plot shows the effect of ENC on the value of σ. The x-axis is the energy (keV). The black points are the experimentally measured values of σ, and the open squares are what the measurements would have been if the only contribution were from statistical fluctuations of charge generation. The ENC contribution is shown by the solid red line, which corresponds to 818 (± 27) electrons.

The next section discusses simulation of the CZT detector response using the spectral parameters extracted from experimental data.

4.6 Simulation of CZT detector response

The previous sections described the analysis of data from laboratory and thermovacuum calibrations of CZT module B11290, and discussed the important conclusions that could be drawn from the results. The main aim of this exercise is to simulate the SRF of the CZT detector over the entire energy range. The first step towards this is to simulate source spectra corresponding to laboratory calibration and validate the modeled spectra against experimental measurements of the same. This is a requirement in order to establish confidence in the procedure adopted.

A Geant4 application was designed to simulate the SRF for the pixels of a single CZT module as per laboratory calibration. The simulation was to be run for different temperatures for high energy photons of the radioactive source ^{57}Co.

A simple model of the detector geometry was chosen. The CZT detector was made *sensitive* by setting the pointer of the object of the CZT sensitive detector class to its logical volume. The energy deposited in the CZT detector was obtained by extracting the *hits* information in the *UserEventAction* class via the object of the *G4HCofThisEvent* class. The source geometry was simulated using the GSPM. During laboratory calibration, the source was positioned such that all pixels were uniformly illuminated. For the simulation, this source arrangement was approximated; a square plane source was used with a parallel photon beam in order to simulate uniform illumination. The physical processes included are listed in table 2.3.

Since the energy deposit in the CZT is extracted in the *UserEventAction* class, one must include the following as input to this class in order to modulate the absolute energy deposit

- the pixel, energy and temperature averaged σ which will be used to induce spread to the absolute energy deposit
- temperature dependent energy-channel conversion equation
- individual $(\mu\tau)_e$ and $(\mu\tau)_h$ values for every pixel, for each temperature

The radioactive source ^{57}Co was simulated in GSPM. The application was executed for the six different temperatures, with each execution consisting of 10^6 events.

The flow of logic that is used for the response simulation, implemented in the *UserEventAction* class is as follows:

- consider the first simulation run for temperature T_1°C and pixel p_1; the $(\mu\tau)_{e,h}$ for this temperature and pixel are entered as input to the application
- when a photon of energy E interacts with the detector, its total energy deposit and depth of interaction are extracted using the object of *hits* collection in the *UserEventAction* class; this is the first event
- the Hecht equation (eqn(4.13)) is part of the code, and the depth of interaction for this event is input into the equation and the CCE η for the event is obtained as a result
- σ is hard coded into the application as a constant value which has no energy or temperature dependence
- E and σ are passed as arguments to the function *G4RandGauss*, which generates a Gaussian energy distribution using E as the mean value and σ as the spread
- this function then randomly selects a value of energy from the distribution, and this is returned as the output of the function
- this value is now the energy deposited in the detector which includes the inherent statistical fluctuations and electronics noise which was contained within σ; let this energy be represented by E_{smear}
- E_{smear} is then multiplied by the η for the event; then the final energy deposit, E_{final} is obtained, which now includes the effects of charge collection
- for temperature T_1°C, the gain and offset are computed using equations (4.24) and (4.25); then the gain, offset and E_{final} are input into eqn(4.23), where the channel number Ch_{final} for that event is obtained
- in this way, Ch_{final} corresponding to each event is generated and these channel numbers are written into a file
- at the end of the run, the file containing the channel number is binned to generate a pulse height spectrum, which is the SRF
- this procedure is repeated for different temperatures; the simulated results are validated against experimentally measured SRF

The simulated and experimental spectra are normalized and represented in units of probability per unit channel. The parameters used for validating the simulated and experimental results are

- Overall spectral shape

- Reproducibility of the peak channel numbers
- Reproducibility of the spectral width parameter (σ)

The results of the simulation are shown in fig(4.13) for four randomly selected pixels, each at a particular temperature.

As can be seen from these plots, there is good agreement between experimental data and the simulated pulse height spectra. According to the legends in the figures, one can see that irrespective of the location of the pixel within the detector module, or the temperature at which the measurements were made,

1. the experimentally extracted values of $(\mu\tau)_{e,h}$ products are correct within uncertainties as the peak normalization and the exponential low energy tail are very well matched for the selected pixels and for the temperatures.
2. the good match between experimental and simulated data support the assumptions made regarding the pixel-to-pixel variation and temperature dependence of spectral parameters

From the simulation of the CZT detector response using spectral parameters extracted from laboratory data, there is ample confidence in the methodology to take the work to the next level, which is the simulation of the detector response using the spectral parameters extracted from thermovacuum calibration data and the generation of the SRF for all energies within the 30-270 keV range.

As discussed earlier, the CZT detector response simulation relies on a procedure set up for generation of the SRF for the detector within the 30-270 keV region. Figure(4.14) shows the simulated SRF for the entire CZT detector, taking into account the $(\mu\tau)_{e,h}$ averaged for each pixel, and the spectral parameters extracted using the data measured with the flight electronics at 11°C in the thermovacuum chamber. The SRF has been generated for three γ-ray lines, 30.97 keV, 81 keV, and 122.1 keV. Similarly, the SRF can be generated for any γ-ray line within the energy range of interest. The y-axis corresponds to the probability that an incoming photon energy E is redistributed into channel 'i'. These values, when generated for all the energies, can then be used to populate a two-dimensional matrix with the rows representing energies and columns representing channel number. The SRF is represented in a tabular form or in the form of a two-dimensional matrix as shown in table(4.3), where E_j represents the energy from 30-270 keV (j), Ch represents the channel number from 0 to 1023 (i), and $\mathrm{p}_{j,i}$ is the probability that E_j is measured in Ch_i. Connecting table(4.3) to fig(4.14), one can see that 30.97 keV is E_1 and the numbers from $\mathrm{p}_{1,1}$ to $\mathrm{p}_{n,1}$ are the probability values for

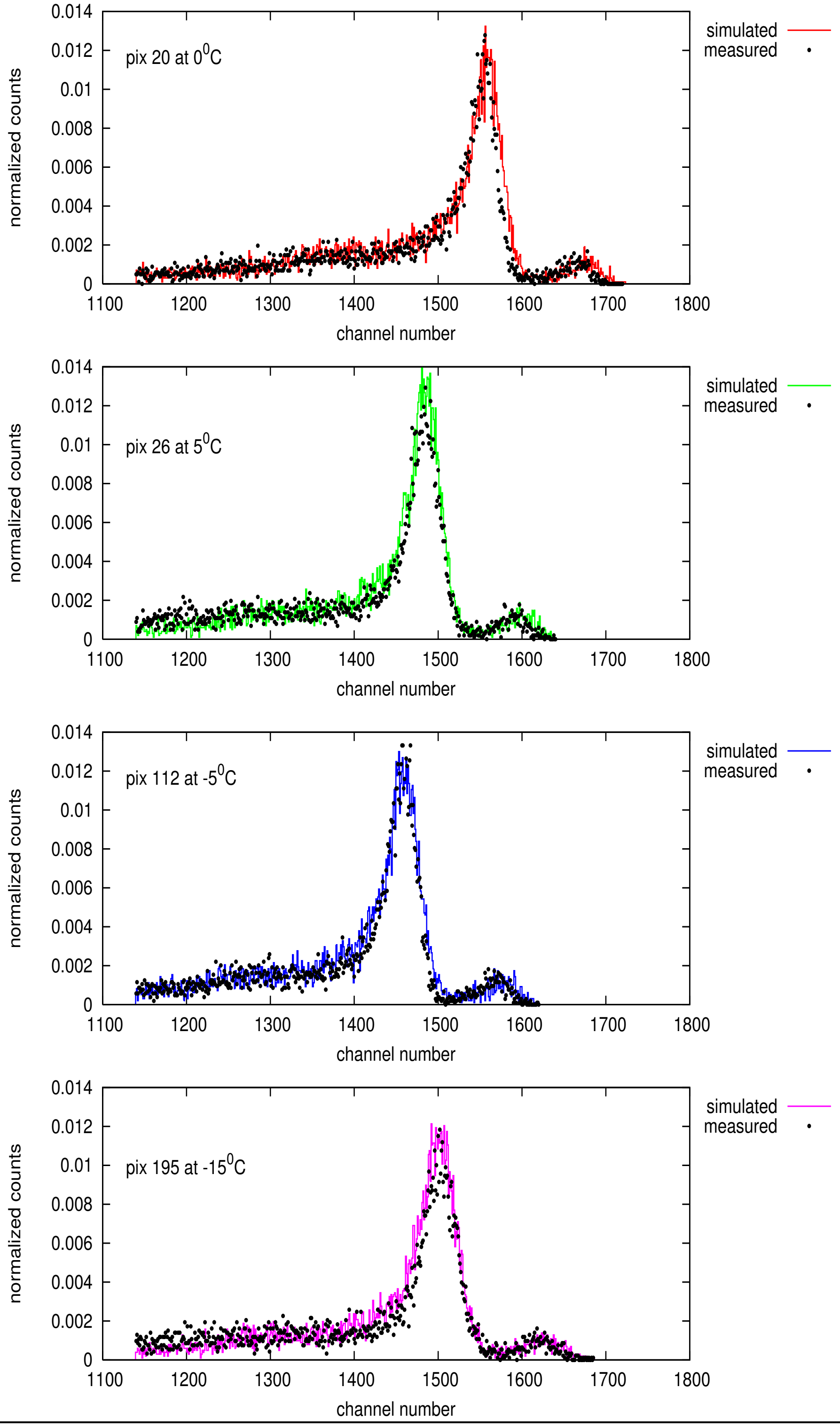

FIGURE 4.13: Reproduction of experimentally measured CZT detector response with Geant4 using spectral parameters extracted from analysis of experimental data. Solid lines represents simulated values, while black points represent experimentally measured values.

Channel→ Energy(keV)↓	Ch_1	Ch_2	Ch_3	$\dots$	Ch_n
E_1	$p_{1,1}$	$p_{1,2}$	$p_{1,3}$	$\dots$	$p_{1,n}$
E_2	$p_{2,1}$	$p_{2,2}$	$p_{2,3}$	$\dots$	$p_{2,n}$
E_3	$p_{3,1}$	$p_{3,2}$	$p_{3,3}$	$\dots$	$p_{3,n}$
$\vdots$	$\vdots$	$\vdots$	$\vdots$	$\vdots$	$\vdots$
E_n	$p_{n,1}$	$p_{n,2}$	$p_{n,3}$	$\dots$	$p_{n,n}$

TABLE 4.3: Tabular representation of the Spectral Redistribution Function (SRF)

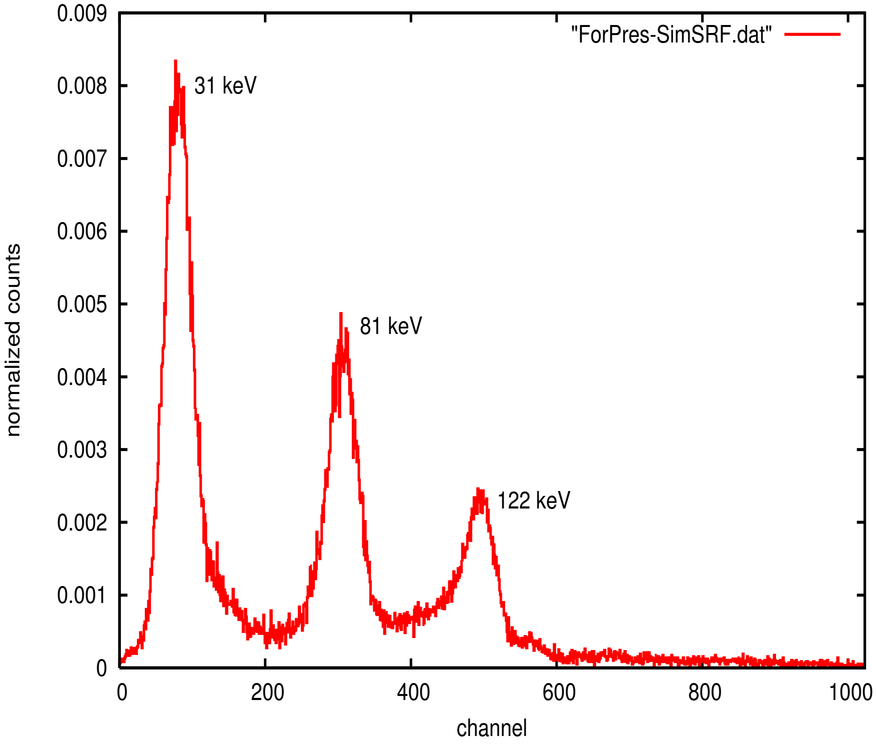

FIGURE 4.14: This figure is a graphical representation of the CZT detector spectral redistribution function (SRF) for 3 γ-ray lines, for the detector module B11290, using the spectral parameters extracted from data measured with the flight electronics in the thermovacuum chamber. The $(\mu\tau)_{e,h}$ products have been averaged over all pixels for this work

30.97 keV from channel 0 to 1023. Similarly, 81 keV is E_2, and 122.1 keV is E_3. At the present time, the generation of the SRF represented in fig(4.14) was done using pixel averaged values of $(\mu\tau)_{e,h}$. At a later stage one would like to incorporate the individual pixel $(\mu\tau)_{e,h}$ values and determine the difference between the two by comparison with actual experimental data. This comparison would help in determining whether the approximation of pixel averaged $(\mu\tau)_{e,h}$ products produces any significant variations.

4.7 Summary and Conclusions

1. The aim of this chapter is to simulate the response of the CZT detector so as to generate the detector spectral redistribution function (SRF) . This is the first step to construction of the response matrix, and was demonstrated.

2. The signal generation in CZT detectors and the effect of charge trapping on the signal pulse height was studied.

3. Using CZT spectral data measured in the laboratory at different operating voltage, $(\mu\tau)_{e,h}$ were extracted for different temperatures using a spectral fitting routine written in IDL. These parameters were extracted for different temperatures for all the pixels of the CZT detector module under study.

4. The variation of the mobility-lifetime products with temperature was studied by taking into consideration the pixel-averaged values. For every 5°C variation in temperature, the $(\mu\tau)_e$ values vary by 0.7% while the $(\mu\tau)_h$ values by 2.3%.

5. Independent data analyses were performed on the CZT detector spectra measured in the laboratory with vendor supplied ground electronics and in the thermovacuum chamber with custom built flight electronics and the differences in the spectral parameters extracted were studied. The most important observation was the measured value of σ

   - In both sets of data it was observed that there was no energy dependence or temperature dependence of σ.
   - **Laboratory Data** - Average σ = 2.4 keV, ENC = 510 electrons
   - **Thermovacuum Data** - Average σ = 3.8 keV, ENC = 819 electrons

   It may be concluded that the energy dependence of σ was washed out by a dominant noise term that showed no dependence on temperature. As can be seen, measurements made with the flight electronics in the themovacuum chamber shows a higher incidence of noise.

6. Using these inputs from experimental data, the CZT detector response was successfully simulated. The confidence gained in reproducing experimental data for individual pixels and for different temperatures lead to the simulation of the detector SRF.

Bibliography

[1d] Osamu Oda, *Compound Semiconductor Bulk Materials and Characterizations*, Aichi Science and Technology Foundation, Japan, 2007

[2d] Barthelmy, S.D et al., *The Burst Alert Telescope (BAT) on the Swift MIDEX Mission*, Space Science Reviews, Volume 120, Number 3-4, pp 143-164, 2005

[3d] Grindlay, J.E. et al., *EXIST: All-sky hard x-ray imaging and spectral-temporal survey for black holes*, New Astronomy Reviews, vol. 49, Issues 7-9, pp 436-439, 2005

[4d] Neubert, T., *ASIM-an Instrument suite for the International Space Station*, AIP Conference Proceedings, Volume 1118, pp 8-12, 2009

[5d] Scheiber, C. et al., *Medical applications of CdTe and CdZnTe detectors*, Nuclear Instruments and Methods A, vol. 458, pp 12-25, 2001

[6d] Orbotech Medical Solutions (OMS)
12 Hamada Street, Park Rabin for Science
Rehovot, Israel

[7d] Narita, T. et al., *Design and Preliminary test of a Prototype CZT imaging array*, Proc. SPIE, Volume 4497, pp 79-87, 2002

[8d] Vadawale, S.V et al., *Multipixel characterization of imaging CZT detectors for hard X-ray imaging and Spectroscopy*, Proc. SPIE, Volume 5540, pp 22-32, 2004

[9d] Slavis, K. R. et al., *Performance of a prototype CZT detector module for Hard X-ray Astrophysics*, Proc. SPIE, Volume 4140, pp 24-32, 2000

[10d] Zanarini, M. et al., *Radiation damage induced by 2 MeV protons in CdTe and CdZnTe semiconductor detectors*, Nuclear Instruments and Methods B, vol. 213, pp.315-320, 2004

[11d] Hull, E. et al., *The effects of 199 MeV proton radiation damage on CdZnTe photon detectors*, IEEE Transactions on Nuclear Science, Volume 44, Number 3, pp 870-873, 1997

[12d] Franks, L. et al., *Radiation damage measurements in room temperature semiconductor radiation detectors*, Nuclear Instruments and Methods A, Volume 428, Number 1, pp 95-101, 1999

[13d] Sivaraman, G., *Characterization of Cadmium Zinc Telluride Solar Cells*, M.S Thesis, University of Florida, 2003

[14d] Kelly, L.A, *Performance Evaluation of two CZT Gamma Ray Imaging Systems*, M.S Thesis, Louisiana State University and Agricultural and Mechanical College, 2005

[15d] Owens, A. et al., *The X-ray response of CdZnTe*, Nuclear Instruments and Methods A, Volume 484, pp 242-250, 2002

[16d] Narita, T. et al., *Development of a Prototype Pixellated PIN CZT detector*, preprint, astro-ph/9806179, June 1998

[17d] Krawczynski, H. et al., *Thick Detectors for Space Borne X-ray Astronomy*, preprint, astro-ph/0410077, October 2004

[18d] Bartlett, L.M et al., *Radiation damage of CdZnTe by intermediate energy neutrons*, Proc. SPIE, Volume 2859, pp 10-16, 1996

[19d] Varnell, L.S et al., *Radiation effects in CdZnTe Gamma-Ray Detectors produced by 199 MeV protons*, Proc. SPIE, Volume 2806, pp 424-431, 1996

[20d] Ramsey, B.D, *(Fine-Pixel) Imaging CdZnTe Arrays for Space Applications*, Proc. IEEE Nuclear Science Symposium Conference Proceedings, pp 2377-2381, 2001

[21d] Dimitrijev, S., *Principles of Semiconductor Devices*, Oxford University Press, 2006

[22d] Ravi, K.V, *Imperfections and Impurities in Semiconductor Silicon*, John Wiley and Sons, 1981

[23d] http://www.amptek.com/anczt2.html

[24d] Hecht, K., *Zum Mechanismus des lichtelekrischen Primästomes in isolierenden Kristallen*, Zeits. Phys., vol 77, pp.235, 1932

[25d] Vadawale, S.V et al., *Characterization and selection of CZT detector modules for HEX experiment onboard Chandrayaan-1*, Nuclear Instruments and Methods A, Volume 598, Issue 2, pp 485-495, 2009

[26d] Sato, G., et al., *Characterization of CdTe/CdZnTe Detectors*, IEEE Transactions on Nuclear Science, Volume 49, pp 1258-1262, 2002

[27d] Freeman, P.E et al. *Sherpa : a mission independent data analysis application* Proc. SPIE, Volume 4477, pp 76-87, 2001

[28d] Fruscione et al. *CIAO : Chandra's data analysis system*, Proc. SPIE, vol 6270, pp.62701V, 2006

[29d] http://www.s-lang.org

[30d] http://idlastro.gsfc.nasa.gov/idl_html_help/home.html

[31d] Zhang, F. et al., *Analysis of Detector Response using 3-D Position Sensitive CZT Gamma-Ray Spectrometers*, IEEE Transactions on Nuclear Science, Volume 51, Number 6, pp 3295-3299, 2006

Chapter 5

The HEX background simulation

This chapter discusses various sources of background in space-based radiation detectors and the simulation of the background of the HEX detector in a lunar environment, using Geant4.

Since the Earth's atmosphere absorbs x-rays and γ-rays, detectors have to be sent above and out of the atmosphere, either on balloons or on satellites, to observe celestial sources of x-/γ radiation. Outer space is not a complete vacuum, but contains dust, energetic particles (nuclei of atoms, electrons and neutrinos), and electromagnetic radiation. This intense ambient radiation environment interacts with the material of the detector and the spacecraft, producing secondary particles. These can interact with the detector, its surrounding material and shields to produce a **background** or noise against which feeble celestial signals have to be measured. This background is called **instrumental background** and is sensitive to the material used for the detector, the distribution of mass around it, including the shielding components used. Instrumental background is very mission specific; it depends on the mission profile, i-e, the orbit type, inclination, altitude, and the solar activity during the mission.

There also exists the pervasive cosmic diffuse x-/γ-ray background which is largely homogeneous and isotropic in nature. When these photons enter the detector aperture, they add to the detector background. X-/γ-ray detectors that are used for remote sensing the surfaces of planets with little or no atmosphere (Mars, Mercury and the Moon), have to deal with planetary "albedos" that enter the detector, either directly through its aperture, or indirectly after interacting with its housing and shields. These "albedos" are produced by the interaction of high energy radiation with planetary surfaces or atmospheres.

Thus, the total background observed by a space-based radiation detector can be expressed as

$$b_{total} = b_{instr} + b_{diffuse} + b_{GCR} + b_{albedo}$$

where b_{total} is the total observed background, b_{instr} is the instrumental background, $b_{diffuse}$ is the background in the detector due to the diffuse photon component, b_{GCR} is the induced background due to GCRs, and b_{albedo} is the background due to albedo radiation.

The sensitivity of a hard x-ray/soft γ-ray detector (tens of keV to hundreds of MeV) is limited by detector background and the low photon intensity at these energies. Sensitivity of a detector is defined the minimum source flux that it can measure, taking into account various factors, like the total background recorded by the detector, the exposure time etc. Thus, precise determination of the detector background is essential in making accurate predictions of the sensitivity of the detector to various energies, for pre-determined exposure times and required statistical significance of the results.

5.1 Components of the Space Radiation Environment

The space radiation environment within the solar system consists of galactic cosmic rays (GCRs), and electromagnetic and particulate radiation from the Sun. Due to the influence of the solar magnetic field, the intensity of cosmic rays with energies less than 1 GeV vary with solar activity. This is called **solar modulation**. The isotropic cosmic diffuse x-rays and γ-rays also pervade interplanetary space. The HEX instrument on Chandrayaan-I is designed to measure the intensity of spectral lines in the 30-270 keV region from the surface of the Moon, at an orbital altitude of 100 km. So, from the point of view of this experiment, the radiation that enters the detector through its aperture are the lunar γ-ray and neutron albedos produced by the interaction of the high energy GCR protons with the lunar surface.

5.1.1 Galactic Cosmic Rays

Galactic cosmic rays are high energy particles that are composed of 87% protons, 12% helium nuclei, and electrons and heavier nuclei, and originate from outside the solar system. They are basically atomic nuclei which have been stripped off their electrons by energetic processes. Primary cosmic rays are those that are accelerated by astrophysical sources. Secondary cosmic rays are produced by the interaction of these primaries with the interstellar medium during their propagation through the galaxy, for example, lithium, beryllium and boron, which are not abundant end-products of stellar nucleosynthesis.

GCRs with energy up to 10^{21} eV are produced by shock acceleration in supernova remnants (SNRs), active galactic nuclei (AGN). GCRs originating from SNRs are not accelerated by the explosion itself. The remnants of the explosion are expanding clouds of gas and associated magnetic fields that can last for thousands of years. The second order Fermi acceleration of the energetic charged particles within the expanding magnetic clouds results in energy gain. These particles ultimately gain so much energy that they cannot be contained by the remnant and so escape into the galaxy. The amount of energy gained by the cosmic rays depend on the size of the acceleration region and the complexity of the magnetic field.

GCRs are affected by magnetic fields. The interplanetary magnetic field, embedded with the solar wind varies with the solar activity, increasing during solar maximum. This magnetic field deflects and excludes GCRs with energies below 1 GeV/nuc, thereby decreasing the intensity of low energy particles. This is how solar modulation takes place, and it results in the anti-correlation of the GCR intensity at low energies with the solar activity. Figure(5.1) shows the GCR proton spectra for various values of solar modulation, corresponding to solar minimum, solar maximum and average solar activity. These spectra have been calculated from [8b] using the formula expressed in eqn(2.9).

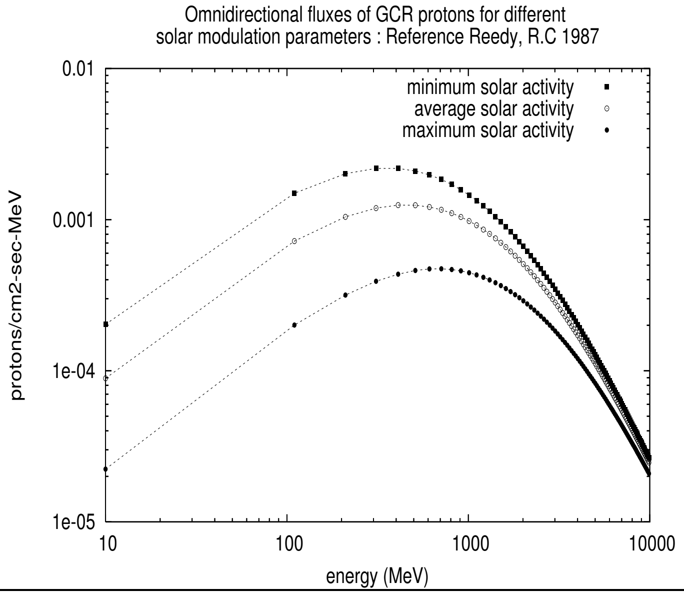

FIGURE 5.1: Galactic cosmic ray proton spectrum calculated from [8b] for different values of solar modulation parameter. For the HEX background simulation, the solar modulation parameter chosen was 550 MeV, which corresponds to average solar activity.

5.1.2 Solar Energetic Particles

Solar Energetic Particles (SEPs) are high energy particles coming from the Sun, consisting of protons, electrons and heavy ions. SEPs can originate from either of these two processes:

1. **Solar Flare**, a violent explosion that takes place in the chromosphere and corona of the Sun, heating the plasma to tens of millions of Kelvins, and accelerating electrons, protons, and heavy ions to high energies and produce electromagnetic radiation across the spectrum. Flares occur at sunspots, where intense magnetic fields emerge from the Sun's surface into the corona, and releases the stored magnetic energy through what is generally believed to be a reconnection process. Streams of highly energetic particles are released into the solar wind, which can enter the Earth's magnetosphere.
2. **Coronal Mass Ejections (CMEs)** are bursts of highly energetic plasma caused by the release of magnetic energy at the Sun. They are not always associated with solar flares. The thin plasma in the heliosphere is shocked when a CME occurs, causing the generation of electromagnetic radiation and acceleration of charged particles. When these particles hit the geomagnetic field, temporary deformation of its structure can occur, causing reconnection of the field at the side of the Earth that is not sunlit. This results in the entry of charged particles into the Earth's atmosphere where they cause auroras.

For the SEPs to reach the Earth or Moon, the particles need to first propagate through the corona to the foot of an interplanetary magnetic field line by diffusion. This can cause significant attenuation of the particle intensity if the distance between the acceleration site and the field line is large. The particles have to travel through interplanetary space along the magnetic field lines which adopt a spiral configuration during solar quiet periods. Diffusion and acceleration by interplanetary shocks can cause scattering of the particles in the medium, resulting in quasi-isotropic fluxes.

5.1.3 Lunar Gamma-ray and Neutron Albedos

Lunar albedo particles are produced due to the interaction of high energy protons from GCRs and SEPs with the lunar crust. The γ-ray spectrum measured by the Gamma-ray Spectrometer (GRS) on the Lunar Prospector (LP) gives abundance information of elements on the Moon like Oxygen, Silicon, Titanium, Aluminum, Iron, Magnesium, Calcium, Potassium and Thorium. Potassium and Thorium decay by natural radioactivity, while the other elements emit γ-rays during de-excitation due to neutron activation. Inelastic scattering and capture of neutrons produced by incident high energy protons generate γ-rays. Reference [1e] states that γ-rays produced by neutron-induced reactions occur at depths of $\sim$140 g cm^{-2} of material, and the scattering of γ-rays within this mass thickness causes a continuum of γ-ray energies to escape the crust along with nuclear lines. These weak lines superimpose the dominant continuum, resulting in their decreased detection sensitivity. In this present study, this simulated continuum spectrum or the lunar gamma-ray albedo (LGRA) was used to determine the background measured by the HEX CZT detector. The continuum is shown in fig(5.2)

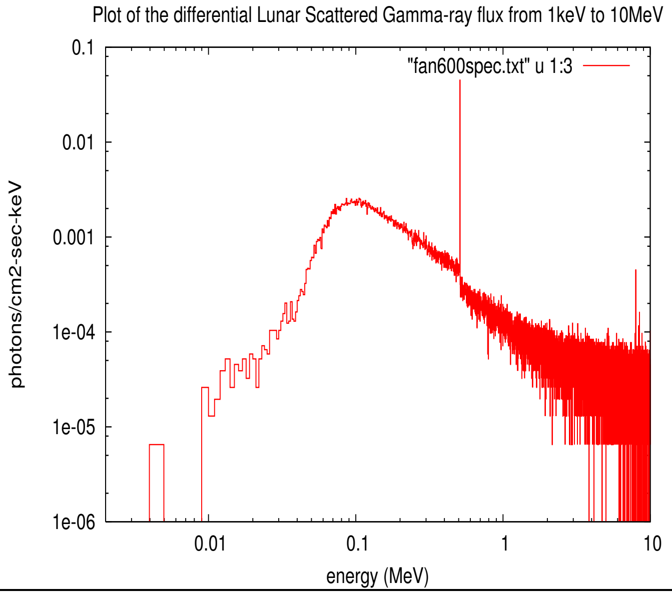

FIGURE 5.2: The lunar gamma-ray albedo (LGRA) from [1e] for the lunar material, ferroan anorthosite. This spectrum ranges from 1 keV to 10 MeV and is simulated using Geant4 by bombarding a lunar target material with GCRs. The intense line at 0.511 MeV is due to electron-positron annihilation.

The lunar neutron albedo (LNA) was measured by the Neutron Spectrometer (NS) of LP. The results of measurements of thermal, epithermal and fast neutron flux from the moon are published in [2e], [3e], and [4e]. Adams et al [5e] reported Geant4 calculations of the LNA which is then compared with LP data. This spectrum from 10^{-2}eV to 10 GeV is used to determine the background in the HEX CZT detector using Geant4. This is illustrated in fig(5.3).

In this thesis, the HEX background is simulated using Geant4 for GCR protons and the LGRA and LNA. SEPs were not used for the calculation at this stage.

What is of interest to the HEX experiment at this point is:

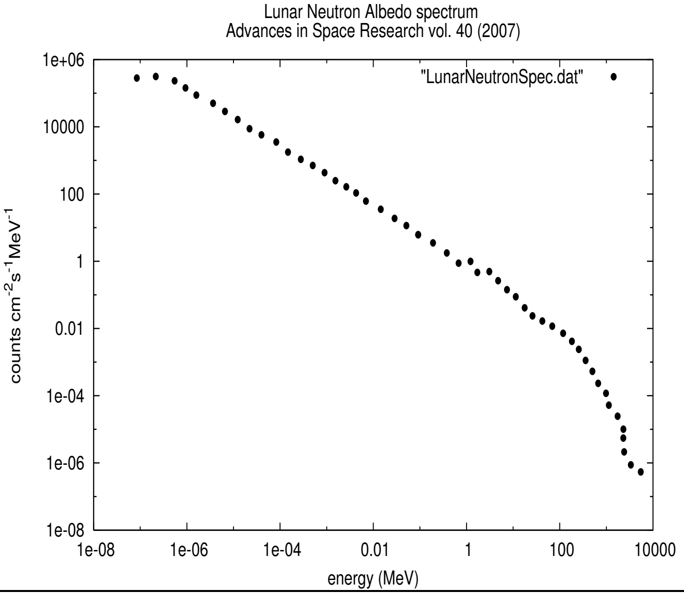

FIGURE 5.3: The lunar neutron albedo (LNA) simulated using Geant4 from [5e]. This spectrum ranges from 10^{-2}eV to 10 GeV.

- the background in the CZT detector due to secondary particles produced by GCRs and the LNA
- how it compares to the background due to LGRA
- the effectiveness of the ACD to minimize this background

The next section discusses the processes by which secondary particles are produced by GCRs.

5.2 Particle Shower Production by Galactic Cosmic Rays

When high energy GCR protons collide with a target nucleus of the spacecraft or detector material, or in the crust or atmosphere of a planet, the nucleus breaks up, producing a large number of secondary particles. These secondaries are mostly hadrons - nucleons, charged and neutral pions, K mesons, hyperons and their corresponding anti-particles. This explosive disintegration or spallation of the target nucleus imparts high energy to the resulting secondary particles, and these high energy nucleons undergo collisions with more nuclei, producing more of the above mentioned secondary particles. These are called **hadronic showers**, where one hadron interacts with a nucleus, producing more hadrons via the strong interaction. As the hadronic shower progresses, the energy of the spallation nucleons decrease to the point that they do not produce any more secondaries, and are stopped in the material by ionization.

The fig(5.4), adapted from [9a] depicts the formation of a secondary particles due to high energy cosmic ray interaction.

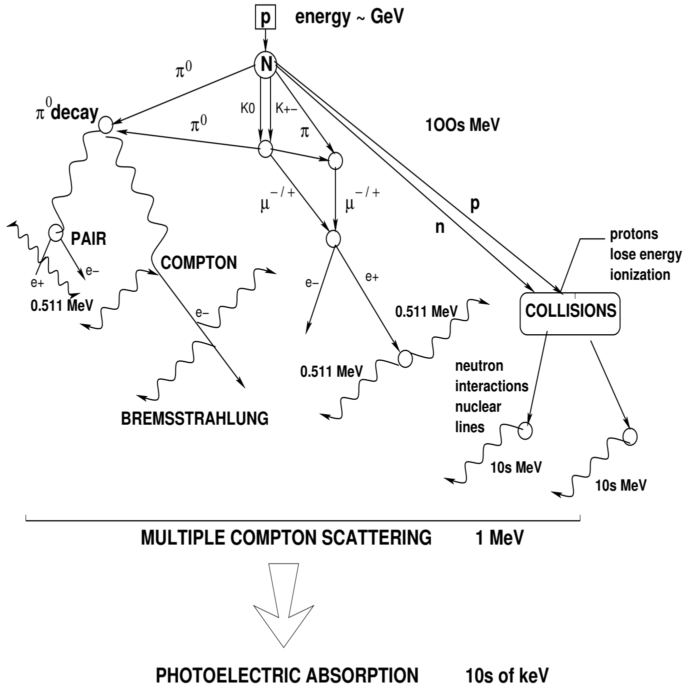

FIGURE 5.4: This schematic adopted from [9a] illustrates the process of secondary particle shower formation when a high energy cosmic ray interacts with matter. Nuclear reactions take place producing hadrons, which decay to give energetic electrons, positrons and photons. Nucleons are also produced, which lose energy by ionization in the case of protons, and inelastic scattering in the case of neutrons. The electrons and positrons lose energy by the emission of bremsstrahlung photons, and ultimately annihilate to produce 0.511 MeV γ-rays. Energetic photons produce more electrons and positrons. The shower progresses in this fashion, till the photons are left with energy sufficient to undergo Compton scattering. This reduces the photon energies further, till it reaches energies relevant for absorption by the photoelectric effect. The electrons ultimately come to rest within the material. Neutrons on the other hand lose energy by scattering and get thermalized. The end result is that nuclear γ-lines are emitted from the material.

The charged pions produced in the hadronic showers have a mean life of 2.6×10^{-8} seconds, and decay by weak interaction in flight to produce charged muons.

$$\begin{aligned} \pi^+ &\rightarrow \mu^+ + \nu_\mu \\ \pi^- &\rightarrow \mu^- + \overline{\nu}_\mu \end{aligned} \tag{5.1}$$

The $\mu^{\pm}$ produced by decay of $\pi^{\pm}$ have a mean life of 2.19×10^{-6} seconds, and are generated with relativistic energies because the pions decay in flight. Charged muons are also produced by the weak decay of K-mesons. Muons decay into electrons/positrons and neutrinos

$$\begin{aligned}\mu^{+} &\rightarrow e^{+}+\nu_e+\overline{\nu}_\mu \\ \mu^{-} &\rightarrow e^{-}+\overline{\nu}_e+\nu_\mu \end{aligned} \tag{5.2}$$

These high energy electrons and positrons emit photons via bremsstrahlung. Neutral pions π^0, also produced in the hadronic showers, have a very short lifetime of 10^{-16} seconds, decaying into two high energy γ-rays. These high energy γ-rays initiate the electronic showers by the process of pair-production. More electron-positron pairs are produced, generating photons via annihilation. The entire process continues, forming an **electromagnetic shower**. The shower continues till the electrons and positrons are produced with lower energies. This **critical energy** at which the shower is stopped ranges from ~100 MeV for air to ~50 MeV for Aluminum. These electrons and positrons slow down to rest mass energies by collisional energy losses in the material, and the positron is annihilated with the emission of two 0.511 MeV photons in opposite directions. The energy of the photons are now such that they lose energy via Compton scattering.

Neutrons and γ-rays produced in these showers are the major contributors to instrumental background, and are the main constitutes of planetary and atmospheric albedos. The next section discusses their interaction and transport in matter, and the contribution to background due to neutrons and γ-rays.

5.2.1 Production of background due to secondary radiation

5.2.1.1 Background from neutrons

The basic concepts of neutron interaction with matter was described in section 1.1.5.2. Neutrons interact with nuclei, and are either annihilated, giving rise to secondary radiation or are scattered leading to a change in direction and/or energy. The secondary radiation produced as a result of neutron interactions are heavy charged particles and in some cases γ-rays. When energetic neutrons suffer a number of collisions with nuclei at room temperature, they are “thermalized” to this energy.

Fast neutrons are free neutrons with energies $\gtrsim$1 MeV and are generally produced in nuclear fission reactions. They are “moderated” to thermal energies by scattering in certain media, like heavy water or graphite. Thermal neutrons are those with energies characterized by the Boltzmann distribution, with energy 0.025 eV being the mode of the distribution at room temperature. Epithermal neutrons are those with energies from 0.025 eV to 1 eV. Thus, all neutrons with energies < 0.5 eV can be classified as **slow neutrons**, while those with kinetic energies > 0.5 eV are **fast neutrons**.

Thermal neutrons have a larger effective nuclear absorption cross section than fast neutrons, and are therefore absorbed more easily by an atomic nucleus. This results in **neutron-induced reactions**, such as **radiative capture** (n,γ). This is **neutron activation** and is the ability to induce radioactivity in materials. Radiative capture is probable in all nuclides but is predominant for heavy nuclides. When a neutron is captured, it forms a compound nucleus, which de-excites by emitting one or more γ-rays.

The probability of neutron scattering increases with energy. The secondary radiation produced by this are recoil nuclei, which pick up a considerable amount of energy during the scattering. The neutron is moderated at each interaction site, till it gets thermalized. Inelastic scattering occurs if the energy of the neutron is sufficiently high, and when this happens, the recoil nucleus gets excited and de-excites promptly with the emission of one or more γ-rays characteristic of the nuclei. Absorption of neutrons by nuclei with emission of heavy charged particles (like protons and α particles) is possible when the energy gained by the neutrons is sufficient to penetrate the Coulomb barrier potential of the nucleus. Sometimes, γ-rays are also emitted with these charged particles.

Fast neutrons can also cause **spallation** of nuclei, which is akin to fission; the residual nuclei are excited and de-excite by nuclear “evaporation”, emitting additional neutrons and γ-rays.

Transport of neutrons depend very much on the composition of the material in which they are produced. Neutrons are slowed down by elastic scattering and the amount of slowing depends on the mass of the nucleus from which the scattering takes place. The lighter the nucleus, greater is the amount of energy the neutron can lose per scatter. Absorption of neutrons with energy < 1 keV is also dependent on the nuclide, again affecting neutron transport.

5.2.1.2 Background from gamma-rays

The most significant physical processes that contribute to the attenuation of high energy photons are the photoelectric effect, Compton scattering and pair production, as discussed in section 1.1.5.2. The photoelectric effects dominates at low energies and high Z values, pair production dominates at high energies and high Z values, while Compton scattering is the most probable interaction process at intermediate energies (hundreds of keV to ∼1 MeV) for all Z and is significant even at low Z and low energies. The nuclear photoeffect is also a means by which γ-rays are attenuated, but its interaction cross section is very small; only one γ-ray in 10^5 or 10^6 interact with nuclei, and the end product of the reaction is a neutron.

In spacecraft materials and the atmosphere or crust of planets, line and continuum γ-ray emission are produced by a variety of mechanisms. Natural radioactivity of elements like ^{40}K, and the isotopes of the U-Th decay chains produce nuclear γ-ray lines. Neutron-inelastic scattering and neutron-capture reactions lead to the formation of excited nuclear states and this leads to the prompt emission of γ-rays characteristic of the nuclide. Continua are produced by the bremsstrahlung of energetic secondary electrons and the decay of neutral pions, which are by-products of GCR proton particle showers. γ-rays produced in any material by these processes are scattered by interaction with atoms and lose energy in the process. These scattered photons add to the continuum at low energies.

Therefore, the background in γ-ray detectors consist of a broad continuum on which are superimposed lines due to natural and induced radioactivity.

It is essential to avoid contaminating the signals of interest with detector background produced by these particles. This is achieved by shielding the detector with materials that stop these particles from entering its field of view. As discussed previously, the HEX experiment employs **active** shielding via anti-coincidence techniques.

The next section discusses a Geant4 application specifically designed to calculate the background detected by the HEX detector on Chandrayaan-I, and to determine the background rejection efficiency of the CsI ACD.

5.3 Simulation of the HEX CZT background and ACD efficiency

The aim of the section is to estimate the background of the CZT detector of the HEX experiment due to GCR protons (average solar activity), LGRA and LNA, and to determine the background rejection efficiency of the ACD.

5.3.1 Geant4 Application Design

The HEX payload was modeled using Geant4, as shown in fig(3.23). All the trays were modeled according to the design, and included the CZT detector and ACD in their respective trays. The electronics cards and components in trays 1, 3, 4, 5 and 6 were not modeled. The Chandrayaan-I spacecraft was modeled as shown in fig(5.5); the components of the spacecraft that were modeled are

- all the panels of the spacecraft, made of Aluminum
- the central cylinder, made of Aluminum, which houses the fuel tanks
- the fuel tanks made of Titanium
- the fuel and oxidizer- monomethylhydrazine and MON-3

These components are shown separately in the fig(5.6). The location of the HEX payload with respect to the spacecraft is indicated in fig(5.5).

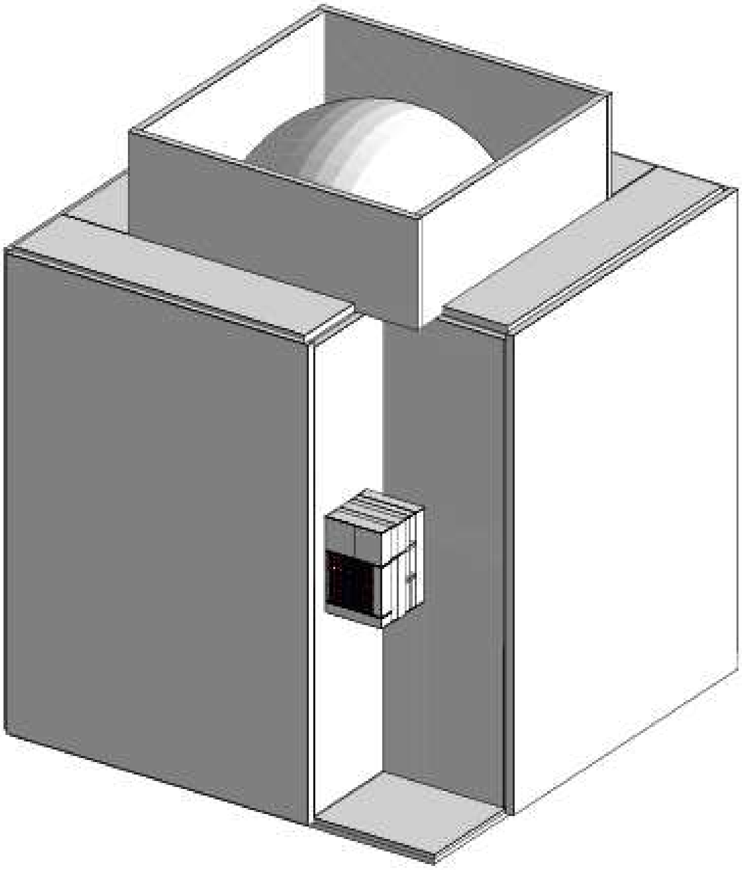

FIGURE 5.5: Geant4 model of the Chandrayaan-I spacecraft with the HEX payload. Note that the other payloads and the solar panels have not been modeled

The ACD and CZT detector responses that were modeled in chapters 3 and 4 are included in this application, with both the detectors made *sensitive*.

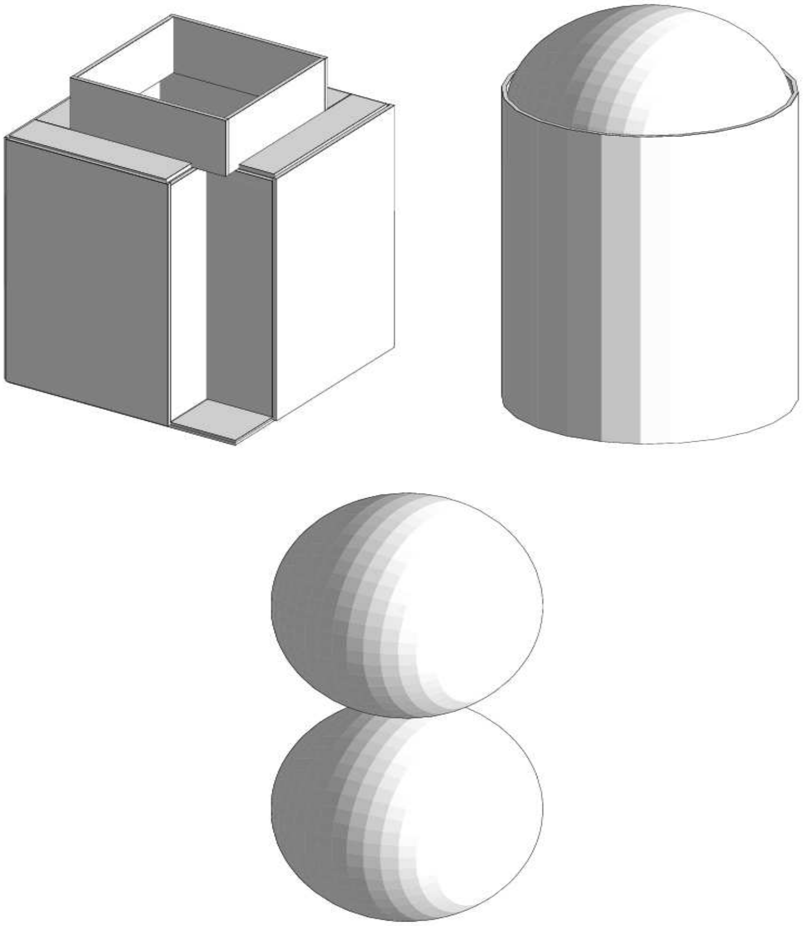

FIGURE 5.6: Break-down of the components of the spacecraft model - **Top left:** the panels of the spacecraft, on which the payloads and solar panel are mounted; **Top right:** the cylindrical structure at the centre of the spacecraft for housing the fuel tanks and fuel; **Bottom:** Fuel tanks

The physics that was used in this background calculation was verified with the results from the Apollo 15 as discussed in chapter 2 and is listed in table 2.6. The electromagnetic physics used is listed in table 2.3.

An important factor to take care for the HEX CZT background simulation is the source-detector geometry. The next sections discuss the approximations and computations undertaken to determine the source-detector geometry for the cases of background simulation using Geant4.

5.3.2 Source geometries for lunar albedos

The lunar gamma-ray and neutron albedo radiations are incident from the surface of the Moon and travel upwards to strike the spacecraft and instrument. Consider the schematic on the left hand side of fig(5.7); here, S indicates the position of the spacecraft with respect to the Moon, and H is the height of its orbit, which is 100 km. As can be seen, at any instant the radiation that strikes S comes from within the region marked between points A and B. These are the positions on the Moon where the tangents drawn from S touch the surface. In order to determine the length of the arc AB, one must make use of the radius of the Moon, R and the orbital altitude H to compute the angle Φ subtended by AB at the centre of the Moon. Using the formula

$$L = R\Phi \tag{5.3}$$

one can calculate the length L of the arc AB. In order to compute Φ, consider the schematic on the right hand side of fig(5.7), and more specifically, the right angled triangle △SAO, where

$$\begin{aligned} \angle\text{SAO} &= 90^\circ \\ \text{AO} &= R = 1738 \quad \text{km} \\ \text{SO} &= SM + MO = H + R = 1838 \quad \text{km} \end{aligned}$$

The unknowns are

$$\begin{aligned} \angle\text{ASO} &= \frac{\Theta}{2} \\ \angle\text{SOA} &= \frac{\Phi}{2} \end{aligned}$$

and

$$\Phi = 180^\circ - \Theta \tag{5.4}$$

Using trigonometry,

$$\begin{aligned} \frac{\Theta}{2} &= \sin^{-1}\frac{AO}{SO} \\ &= \sin^{-1}\frac{1738}{1838} = 71^\circ \end{aligned} \tag{5.5}$$

and therefore, Θ is 142°; substituting this value in eqn(5.4), Φ is 38°. Coverting this from degrees to radians and using eqn(5.3), the length L of the arc AB was computed to be 1152 km. Thus, the region of the Moon which irradiates the spacecraft can be assumed to be bound within a square of sides 1152 km in length.

For an experiment with time constraints like HEX, it is impractical to run a Geant4 simulation using the actual values of L and H. In such a situation a few approximations were made.

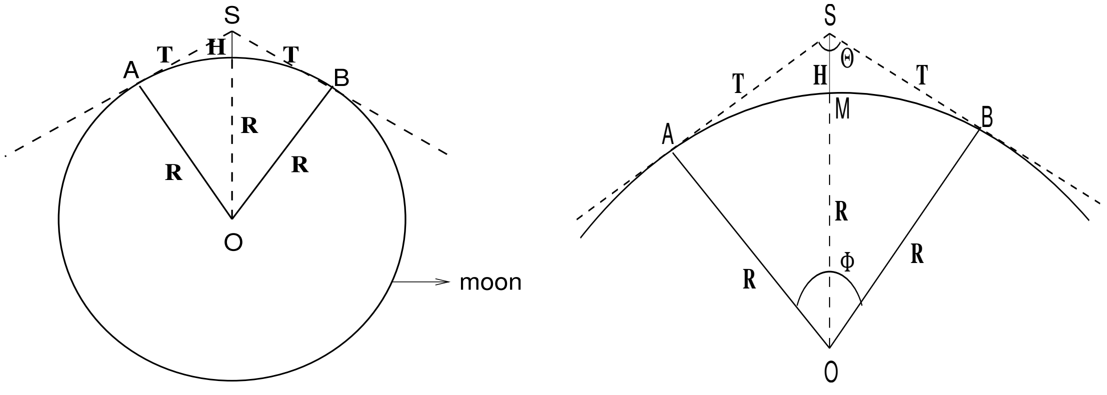

FIGURE 5.7: Schematic to illustrate the Lunar Albedo source-geometry mathematics

First the dimensions were scaled down from kilometers to meters. Then, the ratio between L and H was used to resize the distance of the spacecraft from the source and the area of the irradiating square. For practical purposes, the smallest possible distance between the spacecraft and source was selected with the criterion that the source generator was large enough to irradiate the entire spacecraft, while maintaining the ratio between the two.

The next step is to compute the equivalent integration time T the LGRA and LNA using eqn(2.7) for this source-detector geometry. Using the same methodology outlined in section 2.5, for each radiation source with integral flux $I'(E)$, one determines the number of particles N collected in a vacuum counter of area A corresponding to N_0 primary incident particles. The integral flux of the LGRA and LNA have been computed by fitting the spectra in fig(5.2) and fig(5.3) to functions using the least-square fitting method (using piece-wise functions in energy wherever necessary), and then integrating over the valid energy range. For each case,

- **Lunar Gamma-ray Albedo**
  $N_0 = 10^8$
  $I'(E) = 1.008$ photons $cm^{-2}s^{-1}$
  N = 153257
  A = 144 cm^2 (area of detector)

$$\begin{aligned} T &= \frac{N}{A\,I'(E)} \\ &= \frac{153257}{1.008 \times 144} \\ &= 1056\,\text{seconds} \end{aligned}$$

Given the 10^8 incident particles and the spectrum, this translates to an equivalent integration time of 1056 seconds.

- **Lunar Neutron Albedo**
  $N_0 = 10^8$
  $I'(E) = 10.3$ neutrons $cm^{-2}s^{-1}$
  $N = 293942$
  $A = 144$ cm^2 (area of detector)

$$\begin{aligned} T &= \frac{N}{A\,I'(E)} \\ &= \frac{293942}{10.3 \times 144} \\ &= 198\,\text{seconds} \end{aligned}$$

Given the 10^8 incident particles and the spectrum, this translates to an equivalent integration time of 198 seconds.

5.3.3 Galactic Cosmic Ray Protons

GCR protons are isotropic in space and in principle, should bombard the spacecraft from all directions. But considering the geometry of the spacecraft-Moon as shown in fig(5.8), the Moon shades the spacecraft from GCR protons that come from below. From this it can be seen that the source geometry can be modeled as a hemisphere. Using GSPM, the source geometry for GCR protons was made a hemisphere with radius 2.5

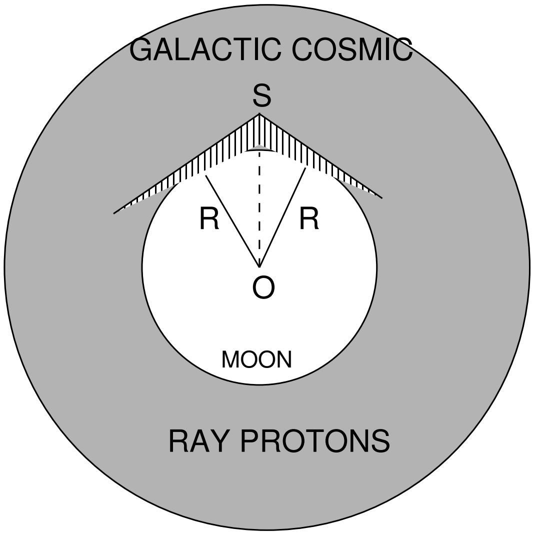

FIGURE 5.8: GCR proton source geometry with respect to the moon and spacecraft.

m, centered at the origin of the co-ordinate system, where the centre of the spacecraft model was also located. Using eqn(2.7), one can compute the integration time with respect to the source geometry and the integral flux of the GCR protons for average solar activity. This is given as,

- $N_0 = 10^8$
  $I'(E) = 3.14$ protons $cm^{-2}s^{-1}$
  $N = 66162$
  $A = 144\ cm^2$ (area of detector)

$$\begin{aligned} T &= \frac{N}{A\,I'(E)} \\ &= \frac{66162}{3.14 \times 144} \\ &= 146 \text{ seconds} \end{aligned}$$

Given the 10^8 incident particles and the spectrum, this translates to an equivalent integration time of 146 seconds.

5.3.4 Simulation Results

For each of the three cases; LGRA, LNA, and the GCR protons for average solar activity, the Geant4 application to simulate the HEX CZT detector background, and suppression by ACD was executed. The output of each the simulations were

- total energy deposit in the CZT detector
- background suppressed energy deposit in the CZT detector
- the ACD four window counts

The energy deposit spectra were normalized with respect to the area of the detector, the integration time as computed above, and the size of the energy binning.

The spectra shown in fig(5.9) have been simulated assuming that the spacecraft is stationary over the region defined by the source in GSPM. The contribution to the total detector energy deposit by the GCR protons are represented by the closed circles, while the open squares and blue asterisks correspond to the LNA and LGRA respectively. As can be seen the maximum contribution comes from the GCR protons, while the LGRA contributes the least; the numbers are tabulated in table(5.1)

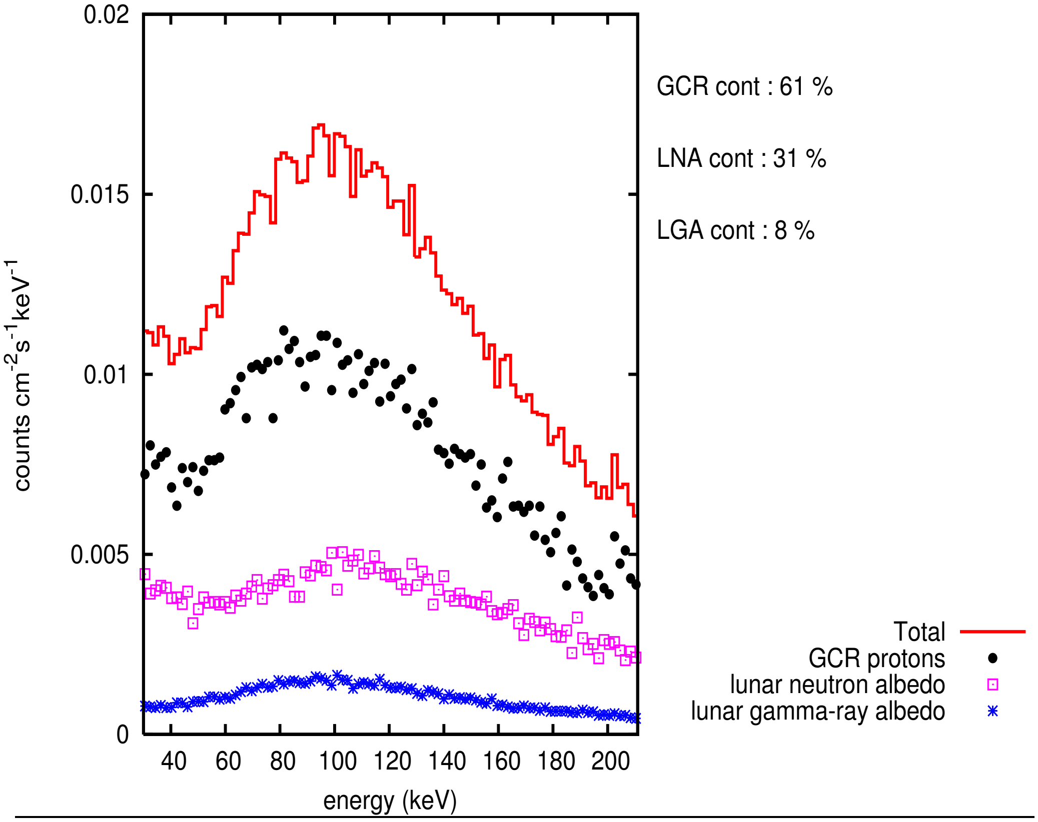

FIGURE 5.9: The total CZT background is represented by the solid red line, while the different components that contribute to this background are shown; the closed circles represent the contribution due to GCR protons, the open squares represent the contribution due to LNA, and the blue asterisks represent the contribution due to the LGRA

Component	Percentage contribution
LGRA	8%
LNA	31%
GCR	61%

TABLE 5.1: Table summarizing the percentage contribution of the lunar albedos and the GCR protons to the energy deposit in the HEX CZT detector, assuming that the spacecraft is stationary over the region defined by the source

These results show that the locally produced secondaries due to interactions of GCR protons with the material surrounding the detector contributes most to the simulated CZT background.

Fig(5.10) shows the total modeled CZT background and the background after veto rejection. The predicted veto efficiency of the ACD over the entire energy range is 21%.

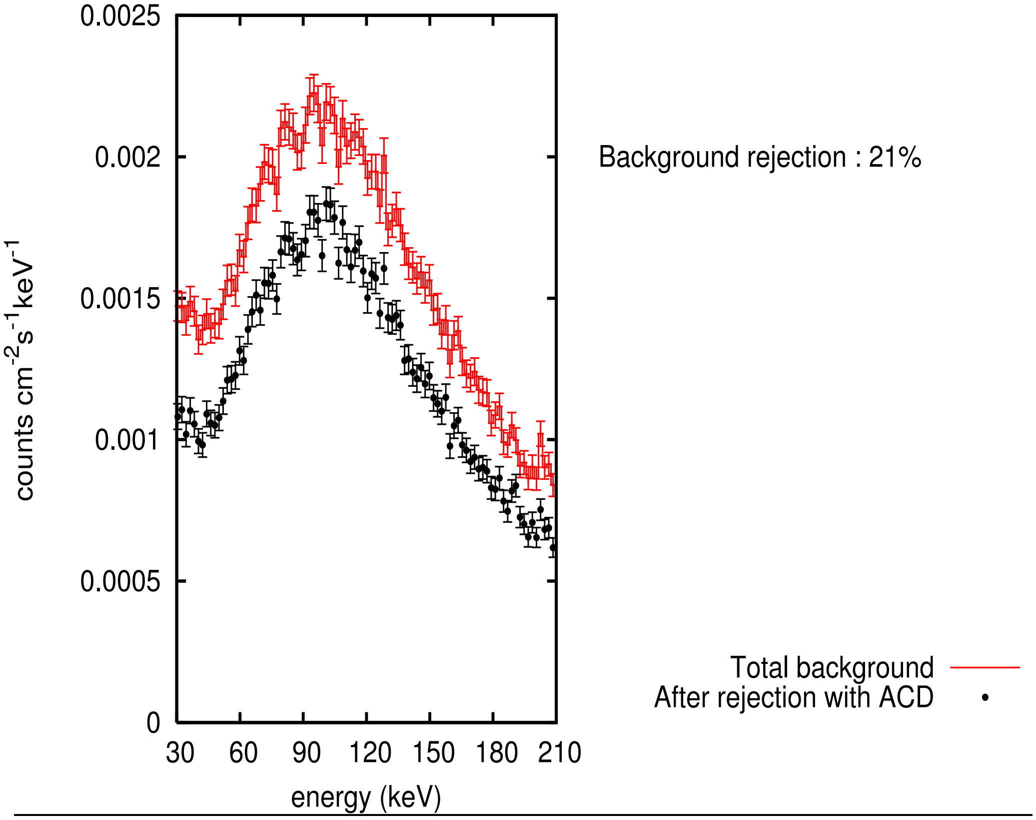

FIGURE 5.10: The total CZT background with and without ACD suppression

When one considers veto efficiency for each of the three components individually as listed in table(5.2), it appears that the ACD is most effective in suppressing events due to the GCR protons. As discussed earlier, these protons are incident on the back and sides of the spacecraft, so the secondary flux that they generate when they interact with the spacecraft, fuel and fuel tanks, have to pass through the CsI ACD before they reach the CZT. This sort of suppression by the ACD is an *out-to-in* process; this means that unlike the Compton scattered photons, these events come from outside the CZT and are stopped by the shielding placed below it. The ACD veto efficiency due to the LGRA is a pure *in-to-out* effect; this means that this is due to Compton scattering that occurs from the CZT into the ACD. This is evident from the fact that the veto efficiency of the ACD due to LGRA photons is similar to the CSE computed for the 1 cm thick CsI ACD (refer chapter 3).

Component	ACD veto efficiency
LGRA	11%
LNA	13%
GCR	37%

TABLE 5.2: Table summarizing the ACD veto efficiency for each of the three components that contribute to energy deposit in the HEX CZT.

Finally, the table(5.3) gives the count rate of the four ACD windows in units of counts per minute, due to the three components that contribute to the total background; the error due to counting statistics is also given. The energy range spanned by each window is indicated in the table. These results are depicted by way of a graph in fig(5.11) as a four window or 'four-channel' spectrum; it appears that for all three components of the background radiation, Window 2 (170-250 keV) has the highest count rate, while the GCR protons cause most of the energy deposition in the ACD. Thus, from the simulation results, Window 2 can be selected during flight as that window with the most efficient veto action.

Component	Win0(30-100 keV) cts/min	Win1(100-170 keV) cts/min	Win2(170-250 keV) cts/min	Win3(>250 keV)
LGRA	22.5±1.13	29.0±1.28	42.5±1.55	37.0±1.45
LNA	316.1±9.79	421.5±11.3	569.7±13.14	404.5±11.07
GCR	832.9±18.63	1026.7±20.68	1104.6±21.45	752.5±17.71

TABLE 5.3: Table summarizing the results of the simulated count rate of the four ACD windows of the HEX instrument, due to different components of the lunar environment. The count rate is in units of counts per minute.

5.3.5 Relevance of simulation results for HEX

The simulation of the HEX background using Geant4 is a composite work that started with the validation of different aspects that would be used as input to the simulation, and included modeling the response of the two detectors of the HEX instrument. All these steps culminated with the estimation of a revised background computation for HEX in the lunar environment. Further work that can be done with respect to this are as follows:

1. include energetic solar protons and electrons in the list of sources that contribute to the background, for different stages of solar activity

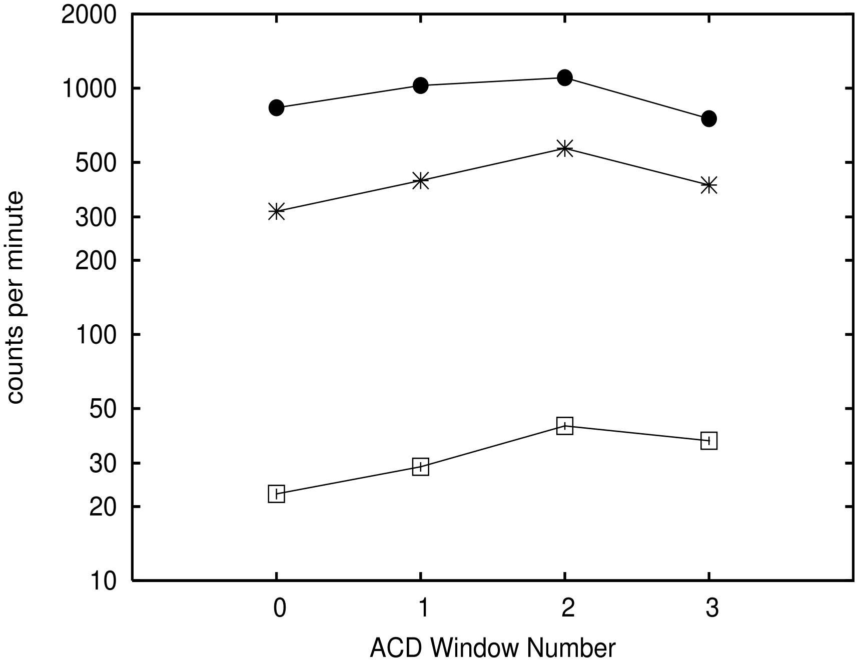

FIGURE 5.11: Simulated four-channel ACD spectrum due to the lunar albedos and the GCR protons; the closed circles correspond to the contribution due to the GCR protons, the asterisks indicate the contribution due to the LNA, while the open squares represent the contribution due to the LGRA. The y-axis is in logarithmic scale.

2. the background due to the variation of lunar albedos and the GCR protons change with solar activity
3. the background due to different lunar terrains

This revised background calculation, and the predicted veto efficiency of the ACD can be used to compute line sensitivities for the γ-rays that lie within energy range of interest of the HEX CZT detector according to eqn(1.12).

Simulating the ACD four-channel spectrum, one can study the energy deposits due to the different components that contribute to detector background in the lunar environment, and can be used to

1. predict the temporal variation of the four channel spectrum, say with respect to variation with solar activity
2. correlate the count rate in the four channel with occurrence of energetic events
3. to determine the component of background radiation that contributes most to the energy deposit; this helps in selection of the window with the most efficient veto action.

Bibliography

[1e] Banerjee, D. and Gasnault, O. *Hard X-rays and low-energy gamma-rays from the Moon: Dependence of the continuum on regolith composition and the solar activity*, Journal of Geophysical Research, Volume 113, E07004, 2008

[2e] Maurice, S. et al. *High Energy Neutrons from the Moon*, Journal of Geophysical Research, Volume 105, pp 20365-20375, 2000

[3e] Feldman, W.C et al. *Fluxes of Fast and epithermal neutrons from lunar prospector : evidence of water ice on lunar poles*, Science, Volume 281, Number 5382, pp 1496-1500, 1998

[4e] Feldman, W.C et al. *Major compositional units of the moon : lunar prospector thermal and fast neutrons*, Science, Volume 281, Number 5382, pp 1489-1493, 1998

[5e] Adams, J.H et al. *The ionizing radiation environment on the moon*, Advances in Space Research, Volume 40, Issue 3, pp 338-341, 2007

Chapter 6

Conclusions

The main goals of this thesis were to model the background measured by the CZT detector of the High Energy X-ray (HEX) experiment on Chandrayaan-I and to estimate the Compton suppression and background rejection efficiency of its anti-coincidence detector (ACD). The multi-particle simulation toolkit Geant4 was extensively used in order to accomplish these goals and was also used for other important issues that were part of the initial steps required for the final simulation.

There is renewed interest among the global space community to colonize the Moon within the next decade. It is therefore essential to map the abundances of minerals, elements and volatiles like water ice, Hydrogen, Oxygen, etc over the lunar surface in order to provide future colonists with means to build and maintain life support systems. It was speculated that volatiles would be trapped in permanently shadowed craters at the Moon's poles.

The HEX experiment was developed primarily to map the intensity of the 46.5 keV γ-ray line over the Moon's surface and to look for enhancements of the signal over the polar regions, which have craters that are permanently shadowed from sunlight. This γ-ray line is a by-product of the radioactive decay of volatile ^{222}Rn. If this line is detected with an enhanced intensity in these regions by HEX, it would provide direct evidence of transport and build up of volatile ^{222}Rn in these deep, dark craters. This can further indicate that other volatiles like water ice could also migrate to these cold traps.

Therefore, the detection of the 46.5 keV line would act as a tracer for other volatiles. HEX was also developed to measure the intensity of γ-rays emitted by other radioactive elements in the 30-270 keV energy range.

HEX is a spectroscopic instrument and was the first experiment designed to measure planetary radiation in the hard x-ray region. This energy region is extremely challenging because of the low signal strength and the intense detector and planetary background emission.

There were two types of detectors used in the HEX experiment: a CZT compound semiconductor for spectroscopy and a CsI scintillator used as an anti-coincidence detector (ACD). The CZT was chosen because it is a room temperature device, providing good energy resolution at high X-ray energies. The CsI detector was chosen because of its rugged and non-hygroscopic nature.

In order to confidently predict the CZT background and the ACD background rejection efficiency, it is necessary to validate the various input parameters used in the Geant4 simulation, like the source-detector geometry and the various physics processes used. An important part of the research approach was to model the detector response of ACD and CZT detectors to reproduce the experimental responses. This is essential as the final background simulation in terms of the integral count rate and the spectral shape depend on how well the detector response was modeled. The same applies for the ACD background rejection efficiency.

6.1 Pre-validation of Geant4

6.1.1 Validation of the source-detector geometry

All the sources described in this thesis were generated by the GSPM and therefore as part of the validation, it was essential to determine whether GSPM actually reproduces the assumed input spectrum. For the sake of simplicity, a simple particle counter filled with vacuum was placed at the centre of a generator sphere. An isotropic distribution of photons with an energy spectrum given by the Cosmic Diffuse X-rays represented by eqn(2.8), were made to impinge the surface of the counter. The aim of the exercise was to reproduce the spectrum input to GSPM as measured by the counter for various test cases. For each test case, the spectrum measured by the counter was well matched with the input spectrum. This indicated that for an isotropic source distribution, the energy spectrum of the incident particles is simulated by GSPM without specific θ or ϕ bias.

6.1.2 Validation of electromagnetic physics

Design optimization of the ACD depends upon the accurate simulation of Compton scattered photons from the CZT, since the main purpose of the ACD is to detect and suppress these photons. The Compton scattered spectrum was measured using a CdTe detector by illuminating a bare CZT crystal with γ-rays from the ^{133}Ba radioactive source. A Geant4 application was generated with the main purpose of reproducing this experimentally measured spectrum. The simulated spectrum recorded by the CdTe agreed very closely with the experimentally measured spectrum. This indicated that the physics used to implement the Geant4 application accurately modeled the Compton scattering in the CZT crystal, as well as the energy deposited in the CdTe detector.

6.1.3 Validation of hadronic physics

High energy radiation in ambient space interact with spacecraft and detector materials to produce a shower of secondary particles like photons, mesons, neutrons, etc which generate fluxes of additional photons and electrons. These deposit energy in the detector, contributing to the background. Since the HEX CZT is a hard x-ray/soft γ-ray detector, it is necessary to validate the γ-ray spectrum generated by the hadron physics selected for simulation. The γ-ray spectrum detected by the NaI detector aboard the Apollo 15 spacecraft was used for the validation. A simulation application was designed in which the Apollo 15 spacecraft and the NaI detector were modeled as shown in fig(2.9). The simulated and observed γ-ray spectra matched well, indicating that the hadronic physics list constructed for HEX background studies included all the necessary physical processes that produce photon-electron cascades.

6.1.4 Issues encountered and approximations

- **Compton scattering from CZT**: The Compton scattered spectrum from the CZT crystal was measured with the AMPTEK XR-100T CdTe detector. In order to meaningfully compare the simulated Compton scattered spectrum it was necessary to include the response of the CdTe detector in the simulation application. To obtain the spectral response of the CdTe detector, it was experimentally characterized using different γ-ray energies and the channel-energy and energy resolution-energy relationships were included. In addition to this, the charge collection efficiency, η of the CdTe detector was also required to complete the response. Due to certain technical constraints, it was not possible to experimentally extract the mobility-lifetime products $(\mu\tau)_{e,h}$ of the electrons and holes. Thus, standard values reported for CdTe detectors were used. For the operating bias of 500 V, these values were used to determine η for different interaction depths in order to reproduce the CdTe response at 122.1 keV. An artifact of this assumption is visible in fig(2.3) as excess counts in the low energy tail of the 122.1 keV photopeak in the simulated spectrum. This is accompanied by a corresponding reduction in photopeak counts when compared with the observed spectrum. This could be due an underestimation of the mobility-lifetime product of the holes, $(\mu\tau)_h$. This effect is also visible in fig(2.5) where the simulated Compton scattered spectrum from the CZT crystal measured by the CdTe detector is compared with the observed spectrum. The bottom panel of the figure shows the residuals obtained from the difference between the experimental and simulated spectra. The residuals are randomly distributed about the zero line throughout the energy range, except in the vicinity of the 276 keV line. The residual plot shows excess counts in the low energy tail of the modeled line spectrum along with the corresponding photopeak count deficit.

However, the discrepancy in this input parameter does not drastically affect the reproduction of the experimentally measured spectrum.

- **Reproduction of the locally produced γ-ray spectrum**: Approximations were made while designing the model of Apollo 15 spacecraft and the NaI detector. The spacecraft and detector were modeled as simple cylinders. The dimensions and material of the detector were according to that used for the experiment. The spacecraft and detector housing were lumped together as a single cylinder with material that was assumed to be Aluminum. Since it was mentioned in [9a] that locally produced γ-rays were generated in material of mass thickness of 50 g cm^{-2}, the dimensions and thickness of the cylinder representing the spacecraft and detector housing were computed accordingly. In addition to these approximations, the NaI detector response and the ^{203}Hg onboard calibration source were not included. Any contribution from SEPs were also neglected.

  Despite these simplifications and assumptions it can be seen from fig(2.10) that simulated spectrum agrees well with the measured one. The most significant result in this validation is the excellent match of the strengths of the 0.511 MeV annihilation line between the observation and simulation.

6.2 Design optimization of the CsI ACD

The main goal of the HEX ACD is to detect and suppress Compton scattered photons from the CZT detector. An ideal ACD system would have surrounded the CZT detector on all sides except that side from which the photons are incident. This set up is generally one of the heaviest subsystems on any space-based γ-ray experiment, and since HEX was imposed with weight constraints related to the spacecraft, it was detrimental to optimize the geometry of the HEX ACD.

The Compton suppression efficiency or CSE was defined as the parameter that would be used in optimization of the ACD geometry design. It is the ratio of the counts coincident between the CZT and ACD (the difference between the CZT counts without ACD and the CZT counts with ACD) to the CZT counts with ACD, expressed as a percentage.

During this exercise, the CSE was computed for three different ACD geometries: a five component ACD, which consisted of four ACDs placed on each lateral side of the CZT with one ACD placed below it, the single component ACD, which consisted of one ACD placed below the CZT and the four component ACD consisting of only the four side ACDs. For each case, the CZT was irradiated with an isotropically distributed photon spectrum with energies from 1 keV to 10 MeV, and the CSE computed. When the three CSEs were compared, it was seen that the CSE due to the four side ACDs was lower than the critical minimum limit of 10% CSE required for an ACD to be deemed efficient. When compared to the CSE for the ideal five component geometry, it was found that the bottom ACD contributed 76% to the CSE. Thus from these results it was decided to use the single component ACD design, foregoing the side ACDs as their combined contribution to the CSE was not worth their weight. This cut-down in design resulted in a 41.7% reduction in weight of the ACD system.

Further, an exercise was carried out to determine whether the weight of the ACD system could be reduced further without compromising on the CSE. A term CSE per unit mass, which is the ratio of the CSE computed for a particular ACD geometry to its mass was defined. For this exercise the CSE was computed for different thicknesses of ACD, starting from the initial 2.5 cm to 1 cm, in steps of 0.5 cm. For each case, the ACDs were placed below the CZT detector and the system was irradiated with an isotropically distributed photon spectrum with energies from 1 keV to 10 MeV. It was found that the CSE per unit mass of the 1 cm thick crystal was the highest at 12%kg^{-1}, compared to that of 7%kg^{-1} for the 2.5 cm thick crystal. Based on these results, the 1 cm thick crystal was chosen for the final design, leading to a further weight reduction of 60.2%.

These steps were important in the course of the research work, as the results of these simulations were used to select the ACD geometry for the final flight design of the HEX experiment.

6.3 Modeling the spectral response of the HEX ACD

The ACD has two side-mounted PMTs and preliminary tests had shown that the spectral parameters like peak channel and the line width σ were dependent on the position of the source on the crystal surface with respect to the PMTs. To take this positional dependence into account, the crystal was characterized with different energies as a function of position. A reference (x,y) co-ordinate frame was defined on the crystal surface, with the origin located at its centre. The different positions used for the characterization are indicated in fig(3.12), and correspond to a particular (x,y) co-ordinate. The channel-energy and σ-energy relationships at each position were then parameterized with respect to (x,y) location on the crystal surface. These parameterized equations were then included as part of the simulation logic. A two step validation procedure was adopted with respect to ACD response modeling.

The first step was modeling the response at the detector level. A simulation application was designed with the detector and its housing modeled with appropriate materials. The components of the geometry are shown in figures (3.18), (3.19), and (3.20). Spectra due to ^{133}Ba and ^{57}Co were simulated and compared with observations. Within experimental errors, the simulation reproduced the spectral response of the ACD.

The second step was modeling the response at the flight package level. In flight configuration, the output of the ACD was restricted to counts obtained in four window counters. For this the HEX package was modeled using Geant4, including the collimator, CZT detector, and the different trays comprising the experiment. This can be visualized from fig(3.23). The aim of this exercise was to reproduce the final window response and validate against experiment; this was successfully simulated and matched well with observations within experimental errors.

Therefore from this, one can be confident about the predictions of background rejection efficiency of the ACD in the lunar environment and proper tuning of window selection for event rejection can be carried out using Monte Carlo simulations.

6.3.1 Issues encountered and approximations made

- **Observed non-linear behavior of the ACD**: The designed energy range of operation of the ACD is from 30-250 keV and so it is assumed that the system is linear within this energy range. As can be seen from figures (3.16) and (3.17), there is a marked deviation of the channel-energy and σ-energy relationships from linearity for energies greater than 122.1 keV. One can see from these plots that there are no data between 122.1 keV and 356 keV. This was due to non-availability of calibration sources with energies in this range. So, we have a limited understanding of the ACD response in this energy range. The fact, the peak channel and σ of the 356 keV peak show lower than expected values, suggest that this could have risen from a a combination of non-linearity and saturation due to pile up. This argument seems to have some credibility because if one examines the

^{57}Co spectrum measured by the ACD in fig(3.22), a peak-like feature which is due to saturated pulses from high energy background radiation is observed between channel numbers 600 and 700. From fig(3.21) it can be seen that the peak that corresponds to 356 keV, falls in the regions where pulses saturate. Due to lack of high energy calibration sources and proper understanding of the reason behind the spectral shape of the 356 keV peak, the channel-energy and σ-energy relationships were fit with non-linear functions that best represented the trend of the data and this response was assumed to be closest to the "real" experimental response.
This uncertainty could have been remedied by feeding pulse generator signals into the systems and correctly determining the energy range up to which the system is linear. This had not been done during the course of the present work due to time constraints imposed upon by demands of the mission.

- **Approximations regarding the modeling of ACD geometry**: During the modeling of the ACD geometry at the detector level, the PMTs were not included during the modeling of the full HEX payload. All the electronics cards except for the CZT mother board were excluded from the simulation. This was based on the assumption that the impact is limited on the simulation results.

6.4 Modeling the spectral redistribution function

The final step in the approach leading towards predicting the background recorded by HEX is modeling the spectral redistribution function (SRF) of the CZT detector. In addition to measuring parameters like peak channel and the spectral width σ as functions of energy and temperature, it was essential to extract the mobility-lifetime products $(\mu\tau)_{e,h}$ of electrons and holes, which were used to determine the charge collection efficiency η of the detector.

The $(\mu\tau)_{e,h}$ values for all clean pixels were extracted for temperatures ranging from -20°C to +25°C. These values were averaged for these pixels in order to obtain $(\mu\tau)_{e_{avg}}$ and $(\mu\tau)_{h_{avg}}$ for the detector, for every temperature. It was found that with every 1°C rise in temperature, $(\mu\tau)_{e_{avg}}$ and $(\mu\tau)_{h_{avg}}$ increases by 0.7% and 2.3%, respectively.

Next, for each pixel, the energy-channel and σ-energy relationships were determined for every temperature. The gain and offset of the energy-channel equation were averaged over all pixels and parameterized as a function of temperature. This exercise was repeated for two cases: first during the laboratory calibration of the detector and second during the thermovacuum test of the HEX instrument. During the two calibration phases it was found that the spectral width parameter σ showed very little pixel to pixel variation, and energy and temperature dependence. Therefore, for the simulation application a constant value of σ was used as the spectral width parameter for all energies and temperatures.

The SRF corresponding to laboratory calibration of the CZT detector was simulated and validated against experimentally observed spectra for randomly selected pixels at different temperatures. The excellent match between simulation and experiment indicated confidence in the input parameters and the simulation procedure. Using the input parameters corresponding to the thermovacuum calibration, one can model the SRF for any energy within 30-270 keV. These SRFs can be used to populate table 4.3, which can then be used in the eqn(4.2) to compute the response matrix for the detector. The response matrix can be used to deconvolve the source spectrum.

6.4.1 Issues encountered and approximations made

- **Averaging parameters over the detector**: Due to minimal variation of parameters like the mobility-lifetime products $(\mu\tau)_{e,h}$ for electrons and holes, and of the gain and offset of the energy-channel relationship over the detector, these were averaged for all pixels and were then parameterized as functions of temperature.
- **The non-thermal noise component**: Detailed analysis of the behavior of the spectral width parameter σ showed that it was dominated by a noise component that smeared out any energy or temperature dependence that σ should have indicated. The source of this noise is not well understood but it is speculated that it could have originated from the ASIC. During the laboratory calibration, this noise source contributed 510 electrons to the spectral width, while during the thermovacuum calibration, the contribution was 819 electrons. This 60% increase could be due to differences between the two electronics setups. During the thermovacuum calibration phase, the tests were conducted using the HEX flight electronics, while the laboratory data were measured using the electronics provided by the manufacturers. Typically with the use of DC/DC converters in a flight payload, this increase in electronics noise can be expected.
  For the simulation, the averaged value of σ was used and despite this approximation, the validation of the simulated SRFs against experiment proved successful.

6.5 HEX background simulation

In the final phase of this thesis, the background expected in the HEX detector was studied. Chandrayaan-I was modeled using appropriate geometry and materials for the major components of the spacecraft. The ACD and CZT detector responses as defined in sections 6.3 and 6.4 were included in the simulation and the ACD logic was activated. Two kinds of CZT pulse height spectra were generated by the simulation: one with all the events (no event rejection) and one with background event rejection by the ACD. The simulation also generated the ACD energy deposit spectrum in the four broad band counters.

The input spectra used for the simulation were the GCR proton spectra for average solar activity, and LGRA and LNA. The simulation application was run for the three input spectra and the CZT detector background and ACD rejection efficiencies were obtained.

The results of the simulation showed that 61% of the CZT background was contributed by GCR protons, while only 8% was due to the LGRA photons. For the total background spectrum, the ACD rejection efficiency was 21%. From the simulation it was clear that the ACD was most efficient (37%) in rejection of events due to GCR protons. The ACD four window spectrum showed that Window 2, which corresponds to the energy band from 170-250 keV, registered the largest count rate with major contribution coming from GCR protons. The simulation clearly shows that Window 2 should be selected during flight for background veto.

6.5.1 Issues encountered and approximations made

- **Model of Chandrayaan-I**: Chandrayaan-I was not modeled in full detail; the solar panel and the other payloads were not included. Many of the electronics and wiring inside the spacecraft were not modeled. The contribution of these components to CZT background could be quite significant, and in order to make realistic background predictions, one may need more a detailed model of the spacecraft.
- **Input spectra**: The SEP spectrum and the contribution from solar flares were not part of the ambient lunar radiation environment for this simulation. The same hold for GCRs corresponding to heavy nuclei. These components would definitely have affected the predicted CZT background.
- **Source geometry approximations**: For the LGRA and LNA incident spectra, the dimensions of the region on the Moon from which these radiation would strike the spacecraft for an altitude of 100 km was computed. It would have been ideal to generate a square shaped plane source using GSPM with dimensions as computed placed 100 km from the Chandrayaan-I model. But due to time constraints, such a detailed simulation could not be done. The dimensions were, therefore, scaled down from kilometers to meters, maintaining the ratio between the spacecraft

altitude and the length of the square region. This approximated “lunar region” was then used as the particle generator to radiate the spacecraft with photons and neutrons.

GCRs are isotropic and in reality bombard the spacecraft from all directions. The GCRs were approximated as being generated isotropically from the inner surface of a sphere whose radius is larger than that of the Moon. Since the altitude of the spacecraft is insignificant relative to the lunar radius, it was assumed that the Moon shields the spacecraft from the effects of GCRs incident from the bottom half of the sphere. The GCR source geometry was therefore approximated as a hemisphere.

6.6 Summary of results and conclusions

1. Optimization of the HEX ACD geometry: Mass reduction and making the system compact
    - from initial design of the five component ACD to single component ACD, resulting in 41.7% weight reduction; from 3.79 to 2.21 kg
    - from initial detector thickness of 2.5 cm to 1 cm, resulting in a 60.2% weight reduction; from 2.21 kg to 0.88 kg
2. Characterization of ACD and response simulation: Position-dependent detector response is a necessary input for predicting the veto efficiency of the ACD and selecting the most efficient window for background suppression in the CZT spectrum.
3. Characterization of CZT detectors and response simulation: Experimental observations suggest that values of certain input parameters can be averaged over the detector, thus simplifying the SRF modeling for the HEX CZT detectors
    - $(\mu\tau)_{e,h}$ do not have strong variation from pixel to pixel for the detector that was studied in this thesis
    - temperature dependence is also minimal for the above parameters
    - variation of the spectral width parameter σ shows no dependence on energy or temperature
4. Background simulation: The maximum contribution to the background was the secondary radiation produced due to interaction of GCR protons with the spacecraft and detector environment. The ACD was most efficient in rejecting this locally produced background. This exercise has the following consequences with respect to the HEX experiment

- can be used to predict the lunar γ-ray line sensitivities
- helps in the study of the four window ACD spectrum with time; this can be considered as a coarse radiation environment study

With respect to the HEX CZT background, it was seen that the measured background was $\sim$3 times larger than that estimated in the present work. It can be therefore be construed that if one runs the simulation with a detailed spacecraft model, including other adjacent payloads and spacecraft electronics packages as well other radiation sources mentioned in section 6.5.1, the measured background counts may be better reproduced in the simulation results.

The spectral data measured by HEX while in orbit was not analyzed or presented in this thesis. The major work presented here was completed before the launch of Chandrayaan-I. Due to technical reasons, data good enough for spectral analysis and deconvolution were not available, and hence is absent in this thesis. Similar reasons hold for the ACD four window data from HEX while in orbit. Unforeseen temperature variations while in lunar orbit deemed it unsuitable for HEX to remain switched on for sufficient time to gather meaningful data.

6.7 Relevance of this work for space science studies

Monte Carlo simulations were used extensively in this thesis and it has proved an excellent tool for space science studies.

Ideally for a spectroscopy experiment one should calibrate the instrument over all energies across the defined energy range. In reality it is usually not possible to possess calibration sources for all energies, or it may be time consuming to set up an extensive calibration facility. However, one can perform a coarse system calibration using available sources that cover the specific region of energy. After system characterization, the spectral parameters can be used as input to a simulation application designed to model the response of the detector in question. As demonstrated in this thesis, if one can reproduce the measured SRF at discrete energies, this application can be used to simulate the SRF for all energies in the range of interest. Thus, virtual system calibration can be performed. One can do this for different experimental settings like for different photon incident angles, calibration using collimator system, etc. This can be used to synthesize the full detector response matrix, as well as to update the matrix, taking into account issues such as changes in gain of the instrument, etc while in orbit. This method can also be used to fine tune experimental parameters that have large uncertainties, by fitting the simulated response with experimental data, and iterating with modified parameters, till the best fit criterion is satisfied.

As demonstrated in this thesis, Monte Carlo methods can be used to make a first order model of the detector background. Such models help in understanding the different contributors to the detector background and also in the transport of radiation through complicated geometries, an essential input when optimization of the detector system is undertaken. The radiation dose for different onboard components can be computed for a particular orbit or epoch of the solar cycle, and this could help in determining optimum positions on a spacecraft for an instrument which would minimize the energy deposited due to hard radiation.

6.8 Future directions

Detailed modeling of geometries and physics relevant for space applications are not feasible using analytical methods, in which the accuracy of the modeling is affected. Monte Carlo methods on the other hand combine tracking of particles through complex geometries and the physics involved and can be used in a variety of applications concerning total system design. Payload design can be optimized according to mission specifics with regards to maintaining or enhancing performance. Detector response can be modeled by including the instrument calibration parameters, which helps in simulating the "real" behavior of the detector as functions of energy and photon incidence angle. Instrumental background can be estimated for the detector due to different sources of space radiation, taking into account their variation with time. This background can be used in analysis of data measured by the payload. In this way, Monte Carlo simulations are very useful in total system design.

The next direction the work, done in this thesis, can take is experimentation with different materials and designs for future experiments. Monte Carlo methods can be used to model detector housing and shields of different materials and one can simulate the background produced in a detector for different materials. This can help selecting material for building new age detector systems. One can also simulate the background produced by shields of different masses. As the thickness of a shield increases, its stopping power increases till an optimum value where the number of particles transmitted through to the detector becomes a minimum. When the shield mass is increased further, it would start to produce secondary particles on its own, contributing to the background in the detector. Therefore using Monte Carlo methods, one can simulate "background curves" of background count rate as a function of shield mass to determine the optimum shield geometry for a specific application. This is of particular importance when we undertake design of living capsules for astronauts in space stations or rocket ships that would transport them to the Moon, Mars or into deep space. One can design the shielding and compute the dose that an astronaut would receive for different space radiation, during quiet solar conditions and during maximum solar activity. This exercise can be taken a step further by designing habitats for lunar and Martian colonizers against geomagnetic storms and general radiation. Keeping this in mind, an important step forward with respect to the work presented in this thesis is to integrate total system design into the simulation, for instance complete payload design, spacecraft design, crew modules etc. From conception to realization, system design usually undergoes changes that need to be considered and incorporated at every step of the simulation. In order to facilitate this, it would be useful to be able to read in CAD drawings of the payload and spacecraft designs in the standardized STEP format. Geometrical dimensions and material properties are embedded in this format.

The work presented in this thesis is the first effort where a Monte Carlo simulation tool was used by ISRO in the area of payload design. This is a useful beginning as far as future experiments are concerned, as we have developed a working system for payload design, response modeling and background estimation which can be refined further as outlined in the previous sections. This also applies to future high-sensitivity instruments which are prone to even low-level background. With respect to manned space flight, it is imperative to conduct validation exercises at each step of the simulation so as to compute accurate doses as far as the living capsules of crew are concerned.

In the future we aim to improve the simulation set up keeping in mind the experience gained from this work and to move towards complete understanding of all the components that contribute to energy deposition in various subsystems of a spacecraft for different space environments.

List of Publications

1. Goswami, J.N and the HEX collaboration, *High Energy x-gamma ray spectrometer on the CHANDRAYAAN-I mission to the Moon*, Journal of Earth System Science, Volume 114, Issue 6, pp 733-738, 2005
2. Shyama Narendranath, K.C , Ramadevi, M.C, Sudhakar, M., Bhattacharya, D., Sreekumar, P., Seetha, S., *SLX 1746-311 in Outburst*, Advances in Space Research, Volume 38, Issue 12, pp 2788-2790, 2006
3. Lechner, A., Pia, M.G, Sudhakar M., *Validation of Geant4 Low Energy Electromagnetic Processes Against Precision Measurements of Electron Energy Deposition*, IEEE Transactions on Nuclear Science, Volume 56, Issue 2, pp 398-416, 2009
4. Vadawale, S.V, Purohit, S., Shanmugham, S., Acharya, Y.B, Goswami, J.N, Sudhakar, M., Sreekumar, P., *Characterization and selection of CZT detector modules for HEX experiment onboard Chandrayaan-1*, Nuclear Instruments and Methods A, Volume 598, Issue 2, pp 485-495, 2009
5. Augelli, M., Pia, M.G, Saracco, P., Sudhakar, M., Weidenspointner, G., Zoglauer, A., *PIXE simulation in Geant4*, IEEE Transactions on Nuclear Science, Volume 56, Number 6, pp 3614-3649, 2009
6. Pia, M.G, Saracco, P., Sudhakar, M., *Validation of K and L Shell Radiative Transition Probability Calculations*, IEEE Transactions on Nuclear Science, Volume 56, Number 6, pp 3650-3661, 2009
7. Sreekumar, P., Acharya, Y.B, Umapathy, C.N, Sharma, M.R.S, Shanmugham, M., Tyagi, A., Kumar, Vadawale, S., Sudhakar, M., Abraham, L., Kulkarni, R., Purohit, S., Premlatha, R.L, Banerjee, D., Bug, M., Goswami, J.N, *High Energy X-ray Spectrometer on Chandrayaan-1*, Current Science, Volume 96, Number 4, pp 520-525, 2009
8. Sudhakar, M., Sreekumar, P., *Detailed Modeling of Radiation Environment within Spacecraft Systems*, Submitted to Nuclear Instruments and Methods A
9. Sudhakar M., Sreekumar, P., *Detector response modeling of the HEX payload on Chandrayaan-1*, Under processing Nuclear Instruments and Methods A

Acknowledgements

One of the times I enjoyed the most during my education was while doing this thesis. I am extremely grateful to my thesis adviser, Dr. P. Sreekumar for his encouragement during this period. He had the faith in me to start working with something new (that is the simulation part of the thesis) and he always gave me freedom to think. I thank him for all the ideas, suggestions and guidance. I am grateful to Dr. B.R.S Babu, my co-guide at the University of Calicut, for all his help to get this thesis done. Dr. Babu has always been very prompt with regards to any queries and doubts. I want to thank Dr. S. Seetha for her encouragement, help and all the interesting discussions we had... related to work and other wide and varied topics. From PRL Ahmedabad, I wish to thank Dr. Santosh Vadawale for his help and Dr. Acharya, Mr. Shanmugham and Mr. Shishir Purohit. I thank Dr. Maria Grazia Pia of INFN, Genova for her collaboration and help in clearing my doubts in Geant4, as well as the Geant4 working group for the same. I want to thank Mr. M. Ramakrishna Sharma for everything he taught me about instrumentation, clearing all my doubts with so much patience. I want to thank Mrs. Lalitha Abraham for her encouragement and the discussions we've had together. I thank Mrs. Padmavathy for all her help regarding administrative duties.

All the scientists and engineers in our department, Dr. Ashoka, Mr. Chandrababu, Mr. Kumar, Mrs. Meena, Mr. Kulkarni, Mr. Umapathy, Dr. Sankarasubramanium, Dr. Radhakrishna; I want to thank them for their support, kind words and help. I want to thank my lab mates... the bits of fun we could snatch during the day were such stress busters!! Premalatha, Deepti, Mahalaksmi, Manjunath, Monoj, Ravishankar, Vaishali, Shyama, Sreejith, Ramadevi, Lalitha, Athreya, Rakhee, Radhika, Uma, Girish, thanks! My dear, dear friends Rajani, Bindu, Syamanthaka, Pooja and Mrs. Parineetha...I am so grateful for their solid support during the worst times and the best!!

My family...my strongest cheer-leading squad... they've been behind me since the day I began dreaming about being a scientist. My Dad, Mom, my two kid sisters Meera and Maya ...seriously ...they've had to put up with my weirdness and eccentricities during this whole time ...Dad and Mom especially. They both have been so patient with everything and the two of them have been so interested in everything I did! They're both two of the biggest contributors to this work!! Meera and Maya ...guys!! What can I say?? The best kid sisters anyone could ever ask for!! I am really, really grateful to my family for all their love, which got me through this thesis.

And to God... the other biggest contributor to this work. Thanks a million... for everything.